

AN INVESTIGATION OF X-RAY FLUORESCENCE YIELDS AND OF THE
COSTER-KRONIG TRANSITION PROBABILITIES FOR THE L_2 AND L_3
SUBSHELLS IN THE HIGH-Z REGION

A THESIS

Presented to

The Faculty of the Division of Graduate
Studies and Research

By

Dale Wendel Nix

In Partial Fulfillment

of the Requirements for the Degree

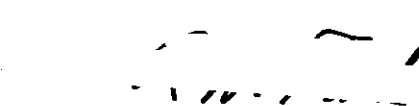
Doctor of Philosophy in the School of Chemistry

Georgia Institute of Technology

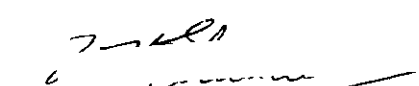
August, 1974

AN INVESTIGATION OF X-RAY FLUORESCENCE YIELDS AND OF THE
COSTER-KRONIG TRANSITION PROBABILITIES FOR THE L_2 AND L_3
SUBSHELLS IN THE HIGH-Z REGION

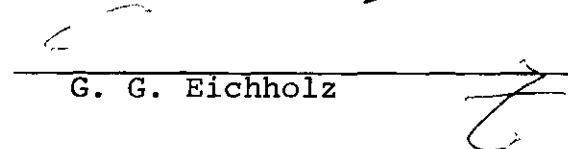
Approved:



R. W. Fink, Chairman



W. H. Eberhardt



G. G. Eichholz

Date Approved by Chairman Aug. 14, 1974

ACKNOWLEDGEMENTS

It gives me great pleasure to recognize those individuals and organizations whose support made this research possible.

I wish to express my sincere appreciation to my thesis advisor, Professor R. W. Fink, who suggested this research project and provided continual help and encouragement. I would like to thank Professors G. G. Eichholz and W. H. Eberhardt for valuable suggestions in their review of this manuscript and for serving as members of my reading committee. My appreciation is also extended to Professors H. M. Neumann and R. F. Borkman for serving on my examination committee.

I sincerely appreciate the advice and assistance given me by the postdoctoral fellows, Drs. J. C. McGeorge, K. R. Baker, W. D. Schmidt-Ott, and J. S. Hansen. Special thanks is extended to Dr. J. C. McGeorge who assisted me in the early stages of my work.

I wish to thank Dr. F. Tolea and Mr. J. H. Landrum for providing radiochemical separations.

My colleagues Drs. W. M. Chew, F. Tolea and S. Mohan, and Messrs. G. M. Gowdy, W. S. Lewis, and J. W. Uecke will always be remembered for their friendship, the kind that is formed through shared defeats and triumphs.

Professors S. T. Manson, H. M. Neumann, R. F. Borkman, and P. V. Rao shared their knowledge in several discussions which helped me obtain a more complete understanding of my work. Their time and concern is greatly appreciated.

I wish to express my sincere appreciation to my parents whose love and guidance will always be cherished.

I am greatly indebted to my wife, Susan, for her sacrificial and untiring support and encouragement during the course of this work. Words alone are so inadequate to express my thanks. In addition, I would like to thank her for typing this thesis.

I am also grateful to the School of Chemistry, Georgia Institute of Technology, which awarded me a teaching assistantship for several quarters; and the AEC which awarded me a research assistantship.

This research project was supported by AEC contract AT (40-1)-3346 as part of a larger program in nuclear spectroscopy-nuclear chemistry.

TABLE OF CONTENTS

	Page
ACKNOWLEDGMENTS	ii
LIST OF TABLES	vii
LIST OF ILLUSTRATIONS	viii
SUMMARY	ix
Chapter	
I. INTRODUCTION	1
1.1 Historical Background	1
1.1.1 Development of the Theory of L-Shell Yields	2
1.1.2 Historical Background on Experimental L-Shell Yields	4
1.2 Applications of this Work	5
1.3 Motivation and Objectives	7
1.4 Terminology	8
II. THEORETICAL BACKGROUND	15
2.1 Radiative Transition Probabilities	16
2.1.1 Nonrelativistic Radiative Transition Probabilities	17
2.1.2 Relativistic Radiative Tran- sition Probabilities	18
2.2 Nonradiative Transition Probabilities	19
2.3 Wave Functions.	22
2.3.1 Screened Nonrelativistic Hydrogenic Wave Functions	22
2.3.2 Numerical Wave Functions	25
2.4 Coupling	30
2.5 Energetics	31
2.6 Concluding Remark on the Theoretical Background	34
III. VACANCY CREATION PROCESSES AND CHOICE OF EXPERIMENTAL METHODS	36
3.1 Summary of Vacancy Creation Processes	36
3.1.1 Fluorescent Excitation	37
3.1.2 Charged Particle Excitation	38
3.1.3 Radioactive Decay	38
3.1.4 Indirect Vacancy Creation	40
3.1.5 Vacancy Creation as Presently Used	41

TABLE OF CONTENTS (Continued)

Chapter	Page	
3.2	Summary of Experimental Methods of Measuring L-Subshell Yields	41
3.2.1	Singles Methods	42
3.2.2	Coincidence Techniques	44
3.3	Outline of the Present Experimental Method.	53
3.3.1	Spurious Events in the Gate Counting Rate	57
3.3.2	Spurious Events in the Coincidence Spectrum	58
3.3.3	Angular Correlation Corrections	60
IV.	SOURCES AND APPARATUS	62
4.1	Choice and Description of Radioactive Sources	62
4.2	Detectors and Their Efficiencies	68
4.3	Electronic Equipment	71
4.3.1	Single-Parameter Coincidence System	71
4.3.2	Dual-Parameter Coincidence System	74
V.	DATA EVALUATION AND RESULTS	77
5.1	Mean L-Shell Fluorescence Yields	77
5.2	L ₂ - and L ₃ -Subshell Yields at Z = 86, 88, 92, and 94.	78
5.2.1	Radon L-Subshell Yields from Ra ²²³ Decay	81
5.2.2	Radium L-Subshell Yields from Th ²²⁷ Decay	81
5.2.3	Uranium L-Subshell Yields from Np ²³⁵ Decay	82
5.2.4	Measurement of f ₂₃ for Uranium from Pa ²³³ Decay	83
5.2.5	Plutonium L-Subshell Yields from Np ²³⁹ Decay	84
5.3	The Measurements of f ₂₃ at Z = 80, 81, and 82 with the Dual-Parameter System	85
VI.	DISCUSSION AND CONCLUSIONS	87

TABLE OF CONTENTS (Concluded)

Chapter	Page
6.1 Discussion and Conclusions of Mean L-Shell Fluorescence Yields	87
6.2 Comparison of Present Values of ω_2 and ω_3 with Theory and with Previous Experiments	91
6.3 Comparison of f_{23} with Theory	96
VII. SUGGESTIONS FOR FURTHER WORK	113
APPENDICES	
I. Correction for Gate Compositions in the Determination of the Net True Coincidence Counting Rates Used in Measurements of f_{23} and Example of Experimental Evaluation of L-Subshell Yields	115
II. Values of f_{23} Omitted from "Most Reliable" Values	126
III. Evaluation of Highly Oriented Graphite Curved Crystals for X-Ray Spectroscopy with Radioactive Sources	130
BIBLIOGRAPHY	133
VITA	143

LIST OF TABLES

Table	Page
1. Identification of Major K and L Shell Characteristic X Rays Used in this Work	9
2. Nominal Detector Specifications	69
3. Present Experimental Values of ν_2 , ω_2 , ω_3 , and f_{23} for $Z = 80, 81, 82, 86, 88, 92,$ and 94.	80
4. Comparison of the $\bar{\omega}_L$ Results with Theory and Previous Experiment	89
5. Summary of Experimental Values and Theo- retical Predictions of ω_2 and ω_3	93
6. Measured $L_2 - L_3$ Coster-Kronig Yields	98
7. Selected "Most Reliable" Experimental $L_2 - L_3$ Coster-Kronig Yields.	100
8. Typical Composition of the K_α X-Ray Gates	116
9. Typical Composition of the L_α Peak in the Coincidence Spectra	117
10. Evaluation of ω_3 from Coincidence Data	123
11. Evaluation of ω_2 from Coincidence Data	124
12. Values of f_{23} Omitted from Selected "Most Reliable" Values	127
13. Resolution vs Energy of Highly Oriented Graphite Curved Crystal	132

LIST OF ILLUSTRATIONS

Figure	Page
1. Siegbahn Notation for the Major K and L Shell Radiative Transitions	10
2. The Photon Spectrum of the Equilibrium $\text{Am}^{243}\text{-Np}^{239}$ Source Showing the Pu K X Rays . . .	55
3. Pu L X Rays in Coincidence with K_{α_1} and K_{α_2} X-Ray Gate Pulses from the Equilibrium $\text{Am}^{243}\text{-Np}^{239}$ Source	56
4. The Photon Spectrum in the K X-Ray Region of the Th^{227} Source	66
5. The Photon Spectrum in the K X-Ray Region of the Ac^{227} Source	67
6. Experimental Detection Efficiency vs Energy for Detector S1	70
7. Fast-Slow Single Parameter Coincidence System	72
8. Fast-Slow Dual Parameter Coincidence System	75
9. Plot of ω_2 vs Z	95
10. Plot of ω_3 vs Z	97
11. Plot of f_{23} vs Z in the Region $60 \leq Z \leq 90$. . .	103
12. Plot of f_{23} vs Z Above Z = 85.	105

SUMMARY

This research involves an experimental study of the L_2 - and L_3 -subshell fluorescence yields (ω_2 and ω_3) and the L_2 - L_3 Coster-Kronig transition probability (f_{23}) in the high- Z region and an experimental study of mean L-shell fluorescence yields ($\bar{\omega}_L$) at $Z = 47, 60, \text{ and } 63$. The following experimental results are obtained:

$$\begin{array}{ll}
 f_{23}(Z=80) = 0.123 \pm 0.012, & f_{23}(Z=81) = 0.109 \pm 0.011, \\
 f_{23}(Z=82) = 0.105 \pm 0.011, & f_{23}(Z=86) = 0.105 \pm 0.011, \\
 f_{23}(Z=88) = 0.053 \pm 0.052, & f_{23}(Z=92) = 0.147 \pm 0.010, \\
 f_{23}(Z=94) = 0.226 \pm 0.016, & \\
 \omega_2(Z=86) = 0.459 \pm 0.025, & \omega_2(Z=88) = 0.493 \pm 0.030, \\
 \omega_2(Z=92) = 0.560 \pm 0.033, & \omega_2(Z=94) = 0.513 \pm 0.022, \\
 \omega_3(Z=86) = 0.384 \pm 0.020, & \omega_3(Z=88) = 0.408 \pm 0.027, \\
 \omega_3(Z=92) = 0.481 \pm 0.029, & \omega_3(Z=94) = 0.509 \pm 0.029, \\
 \bar{\omega}_L(Z=47) = 0.0425 \pm 0.0064, & \bar{\omega}_L(Z=60) = 0.131 \pm 0.017, \\
 \bar{\omega}_L(Z=63) = 0.142 \pm 0.023. &
 \end{array}$$

A comparison of the "most reliable" experimental values of the L_2 - L_3 Coster-Kronig transition probability f_{23} , selected on the basis of rigid criteria from the present results and from published results, with current theoretical predictions allows the following conclusions to be drawn:

- 1) The experimental values of f_{23} are in general agreement with theoretical results in the region $63 \leq Z \leq 88$.

2) The theoretical prediction of McGuire agrees with the experimental result at $Z = 96$, where both $L_2-L_3M_{4,5}$ transitions are well above threshold and contribute fully.

3) The experimental results at $Z = 92$ seem to indicate that the $L_2-L_3M_4$ transition is very near threshold and contributes only part of its full intensity to the value of f_{23} .

4) The disagreement of approximately 25 percent at $Z = 94$ between the theoretical prediction of Chen and Crasemann [using the independent particle model (IPM) with a Green-Sellin-Zachor (GSZ) potential] and the experimental results is attributed to the inaccuracy of the theoretical prediction caused by the inaccuracy of the adjustable parameters used in the Green-Sellin-Zachor potential.

5) More experimental determinations of f_{23} are desirable, especially at $Z = 91$ and 93 , in order to completely understand the effect of M_5 and M_4 electron ejection on f_{23} .

6) Further calculations of f_{23} above $Z = 92$ are necessary, in order adequately to compare theory with experiment.

Comparison of mean L-shell and of L_2^- and L_3^- -subshell fluorescence yields with theoretical predictions leads to the following conclusions:

1) At $Z = 47$, the theoretical mean L-shell fluorescence yield predictions of Chen and Crasemann agree better with experiment than do those of McGuire.

2) Although there is overall good agreement between experiment and McGuire's theory for ω_2 , the available experimental accuracy (limited mainly by uncertainties in detector efficiency) is not sufficient to distinguish between the theoretical predictions due to McGuire and those due to Chen, Crasemann, and Kostroun, however it appears to rule out the IPM calculation with the GSZ potential by Chen and Crasemann.

The discrepancy between the experimental results using the L_α gating coincidence technique and the $K_{\alpha_{1,2}}$ gating coincidence techniques is studied. It is found that these techniques are equivalent and that any discrepancy between them is due to improperly applied corrections to the experimentally determined quantities used to calculate f_{23} .

The possible use of highly oriented graphite (HOG) mosaic curved crystals for determination of x-ray fluorescence and Coster-Kronig yields was evaluated. It was found that the problems arising from low efficiency makes coincidence studies impossible within a reasonable time. In addition, the problems arising from low efficiency, source attenuation, and assumptions of quantities from other measurements in the singles use of HOG crystals makes it difficult to use them for precise measurements of fluorescence and Coster-Kronig yields.

CHAPTER I

INTRODUCTION

1.1 Historical Background

Ever since the discovery of the radiative atomic deexcitation process [the discovery of x rays by Röntgen in 1895 (1)] and the discoveries of the nonradiative atomic deexcitation processes [the discoveries of the Auger effect in 1925 (2) and the Coster-Kronig transition in 1935 (3)], the understanding of the radiative and nonradiative processes and their interrelation has been the object of much experimental and theoretical work. A brief account of the experimental and theoretical work on these processes as they apply to L-shell fluorescence yields and Coster-Kronig transition probabilities is given in the following sections.

A brief set of definitions is given here in order to be able to discuss the development of the theory and the historical background of L-shell yields. The i th subshell fluorescence yield ω_i is the probability that a transition occurs in which an L_i subshell vacancy is replaced by an X vacancy (X stands for M, N, O, ...) with the concomitant emission of an (L_i-X) x ray*. The i th subshell Coster-Kronig

*This is frequently expressed in a shorter way, i.e., ω_i is the probability that a vacancy in the L_i subshell is filled through a radiative transition $[(L_i-X) \text{ x ray}]$.

yields (or transition probabilities, $f_{i,j}$) are the probability that a vacancy is transferred from the i th subshell to the j th subshell ($i < j$). The probability that an L-shell x ray is emitted due to a primary i th subshell vacancy is called the mean subshell fluorescence yield (v_i) and the probability that an L-shell x ray is emitted due to an L-shell vacancy is termed the mean L-shell fluorescence yield ($\bar{\omega}_L$). For a more complete and detailed set of definitions see Sect. 1.4.

1.1.1 Development of the Theory of L-Shell Yields

A few years after the discovery of x rays, a systematic study of x-ray frequencies as a function of atomic number (Z) was undertaken by Moseley (4). This study enabled him to interpret characteristic x-ray emission on the basis of the Bohr theory of the atom (5). The old Quantum Theory on which this interpretation was based was not sufficiently complete to explain transition probabilities, level widths, or other features of x rays.

After a consistent theoretical framework of quantum mechanics was developed (6, 7, 8), Massey and Burhop (9) calculated radiative transition rates for the L subshells. These relativistic calculations employed screened hydrogenic wave functions. Subsequent to this work many other calculations were performed*.

* A review of all radiative calculations is given by Scofield (10).

After the Auger and Coster-Kronig transitions were discovered, a complete description of the atomic deexcitation process became available. Shortly thereafter, crude calculations of the nonradiative (Auger and Coster-Kronig) transition probabilities were undertaken by Pincherle (11) in 1935 and independently by Burhop (12) also in 1935. A review of all the Auger and Coster-Kronig rates is given by Burhop (13), Burhop and Asaad (14), and Bambynek et al. (15).

Owing to the apparent lack of accurate wave functions and the lack of reliable experimental data, few attempts were made to calculate a comprehensive set of L-shell fluorescence and Coster-Kronig yields until very recently. Pincherle (11) in 1935 attempted calculations employing nonrelativistic hydrogenlike wave functions with Slater screening. Later in 1960, crude semitheoretical values of subshell fluorescence and Coster-Kronig yields were computed by Listengarten (16). The three current comprehensive theoretical sets of calculations are due to McGuire (17, 18); Chen, Crasemann, and Kostroun (20), and Crasemann, Chen, and Kostroun (21) published in 1971; and Chen and Crasemann (22), published in 1973. These 1971 to 1973 theoretical calculations were stimulated by the appearance of accurate experimental results on the K, L, and M shells due mainly to work carried out by the nuclear chemistry group at Georgia Institute of Technology and the physics group at Emory University.

1.1.2 Historical Background on Experimental L-Shell Yields

The first L-shell fluorescence yield was measured by Auger (2) in 1925. He measured $\bar{\omega}_L$ by photographing Auger electron tracks in a cloud chamber. A later systematic study of $\bar{\omega}_L$ was undertaken by Lay (23) using a fluorescent excitation technique with detection of the emitted radiation with photographic plates.

Küstner and Arends (24) and Stephenson (25) measured the L_3 -subshell fluorescence yield (ω_3) using a secondary radiator to obtain x rays of energy greater than the binding energy of the L_2 subshell in certain elements (selective excitation of L_3 subshell). The ratio of fluorescent radiation to the primary beam intensity was used to calculate the fluorescence yield.

Salgueiro et al. (26) used a method combining high resolution measurements of L x rays and α -particle-L x-ray coincidence measurements to determine the L_2 -subshell fluorescence yield (ω_2) and Coster-Kronig yield (f_{23}). This method has serious limitations, as discussed in Sect. 3.2.3.

Lazar and Lyon (27) first used the K_α x-ray-L x-ray coincidence method to obtain a mean fluorescence yield (ω_{KL}).

Jopson et al. (28, 29) used fluorescent excitation to create vacancies which they studied by the K_α x-ray-L x-ray coincidence technique. In a later paper Jopson et al. (30) used a secondary radiator to measure the L_2 - and L_3 -mean subshell fluorescence yields (ν_2 and ν_3).

Hohmuth, Müller, and Schintlmeister (31) and Hohmuth and Winter (32), using radioactive sources, measured a group of mean L-shell fluorescence yields, in the range $37 \leq Z \leq 80$. They used the K_{α} x-ray-L x-ray coincidence technique and the γ -ray-L x-ray coincidence technique (see Sect. 3.2).

Rao and Crasemann (33) used critical absorbers with the K_{α} x-ray-L x-ray coincidence technique to measure the L_2 and L_3 subshell fluorescence and Coster-Kronig transition probabilities (ω_2 , ω_3 , and f_{23}). Later work by Price, Mark, and Swift (34) exploited the development of semiconductor detectors to isolate the L_2 and L_3 vacancies by resolving K_{α_1} and K_{α_2} x rays. The L x rays were detected with a low resolution device [NaI(Tl) scintillator], thus only the L_2 - and L_3 -mean subshell fluorescence yields (ν_2 and ν_3) were measured. Rao, Wood, and Palms (35) and Rao et al. (37) used a combination of lithium drifted germanium [Ge(Li)] and lithium drifted silicon [Si(Li)] detectors to resolve both $K_{\alpha_{1,2}}$ x rays and L x rays to measure ω_2 , ω_3 , and f_{23} .

1.2 Applications of This Work

The study of fluorescence yields is of great interest, since it presents an opportunity to investigate quantities which are of fundamental physical interest as well as an opportunity to study quantities which are of practical value. The applications of these quantities in chemical analysis are a good example of their practical use. The technique of

x-ray fluorescence analysis has been applied to samples from geological and oceanographic exploration, samples of heavy elements in biologically important molecules, atmospheric samples of air and water pollutants, rock samples from lunar explorations, samples for elemental analysis in nuclear medicine, and samples for control of industrial processes.

A knowledge of fluorescence and fluorescence yields is necessary for the standardization of certain radioisotopes used for detector efficiency calibrations. Low-energy γ rays are highly converted; therefore, x rays are the only monoenergetic photons available for standardization of radiation detectors at energies below about 30 keV. The calculation of the number of x rays emitted per disintegration requires an accurate knowledge of fluorescence and Coster-Kronig yields.

Applications of fluorescence and Coster-Kronig yields in fundamental research include their use in the interpretation of measurements in nuclear and atomic physics. Since the only detectable emissions from orbital electron capture are x rays and Auger electrons, a study of these emissions frequently leads to information about the decay energy (Q_{EC}). The multipolarity of internally converted γ rays can be deduced from x-ray intensity measurements and a knowledge of fluorescence yields, giving information on nuclear structure.

1.3 Motivation and Objectives

Past efforts to study fluorescence and Coster-Kronig yields at high atomic numbers (Z) have produced experimental results which exhibited rather serious disagreements among each other and exhibited large uncertainties (see Sects. 3.2 and 6.3) (39-40). The high- Z region is of special interest since the Coster-Kronig transitions $L_2-L_3M_5$ and $L_2-L_3M_4$ are believed to be energetically possible for $Z \geq 90^*$. These added transitions produce a large increase in f_{23} in this region (see Sect. 6.3).

Recent work using the L_α gating technique (41) (described in Sect. 3.2) to measure f_{23} has produced results which are in better agreement with theory for $Z \leq 88$ than older results using the K_α gating technique (see Sect. 6.3). The apparent systematic disagreement between these two techniques seemed worthy of investigating and in the present work the two methods will be shown to give identical results when proper corrections are made (see Sect. 6.3).

The availability of still higher resolution in the detectors, more advanced electronics, and multiparameter analyzer systems should enable one to remove the discrepancy

* Any allowed nonradiative transition that is energetically possible (i.e., $E > 0$ where E is the energy of the ejected electron) will take place. For the $L_2-L_3M_5$ transition one approximation for E is given by: $E = BE(L_2) - [BE(L_3) + BE(M_5)]$ where $BE(L_2)$, $BE(L_3)$, and $BE(M_5)$ are the binding energies of the L_2 , L_3 and M_5 subshells, respectively (2).

between the two methods and to determine values of f_{23} with much improved accuracy.

The objectives of this work were to study high-Z L-subshell fluorescence yields and Coster-Kronig transition probabilities and to resolve the discrepancies in f_{23} values, in order to obtain a consistent set of results with which to test theory. In the course of this work, some accurate determinations of high-Z L-subshell fluorescence yields will have been made and compared with theoretical results.

1.4 Terminology

The complex electronic rearrangement process for ionized atoms gives rise to an involved scheme of definitions and notation. The construction of this scheme is based upon two rearrangement processes consisting of radiative and non-radiative transitions. The deexcitation process in an ionized atom requires the movement of an electron to a lower level. The excess energy can be emitted in the form of a photon (i.e., a radiative transition) or the excess energy can be transferred to an electron (from a higher shell or subshell) which is emitted (i.e., a nonradiative transition). Table 1 gives a list of the major radiative transitions and their classical Siegbahn notation for the K and L shell (see Fig. 1). The nonradiative transitions are classified according to whether a vacancy is left in the original shell (the Coster-Kronig process, $X_i-X_jZ_k$) or both final vacancies are

Table 1. Identification of Major K and L Shell Characteristic X Rays Used in This Work

X Ray or X-Ray Group	Transition
K_{α_1}	$K - L_3^*$
K_{α_2}	$K - L_2$
K_{β_1}'	$K - M$
K_{β_2}'	$K - N, O$
L_{λ}	$L_3 - M_1$
L_{α}	$L_3 - M_4, M_5$
L_{η}	$L_2 - M_1$
L_{β}	$L_2 - M_4$ $L_3 - N, O$ $L_1 - M$
L_{γ}	$L_1 - N_2, N_3$ $L_1 - O_2, O_3$ $L_2 - N, O$

*The notation $K, L_1, L_2, L_3, M_1, M_2, \dots$ is an abbreviation for $1s_{1/2}, 2s_{1/2}, 2p_{1/2}, 2p_{3/2}, 3s_{1/2}, 3p_{1/2}, \dots$ levels, respectively. This notation is valid in the jj -coupling approximation and is used in most of the x-ray literature on fluorescence yields and Coster-Kronig transition probabilities. The notation $K - L_3$ implies that an original vacancy in the K shell is transferred to the L_3 subshell with the emission of a quantum of electromagnetic radiation (K_{α_1} x ray).

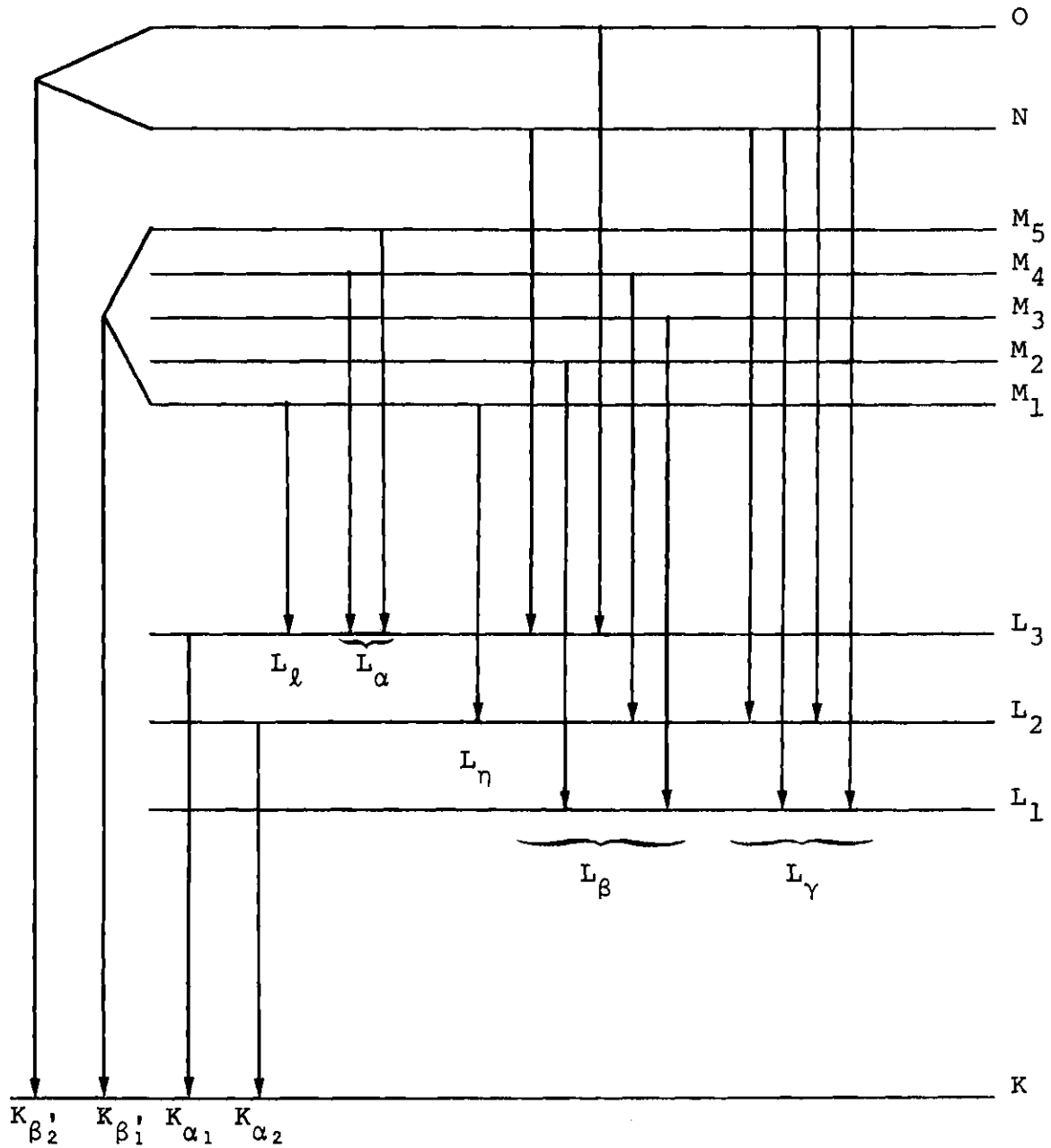


Figure 1. Siegbahn Notation for the Major K and L Shell Radiative Transitions

in a higher shell (the Auger Process, $X_i - Y_j Z_k$)*.

Owing to the multiple deexcitation processes present, it is necessary to define several different transition probabilities. Associated with a single K-shell vacancy there are two such yields, the K-shell fluorescence yield (ω_K) and the K-shell Auger yield (a_K); ($\omega_K + a_K = 1$). The K-shell fluorescence yield is defined as the probability that a vacancy in the K shell of a singly-ionized atom is filled by a radiative transition (K x ray). The Auger yield is defined as the probability that a vacancy in the K shell of the atom is filled by a nonradiative transition (K-Auger transition). Thus,

$$\omega_K = I_K/n_K = 1 - a_K \quad (1)$$

where I_K/n_K is the relative number of K x rays emitted per K-shell vacancy, I_K is the absolute number of K x rays emitted, and n_K is the absolute number of K shell vacancies.

The L-subshell yields are denoted for the L_1 subshell

*The notation $X_i - Y_j Z_k$ (or $X_i - X_j Z_k$) signifies that the original vacancy in the X_i subshell is transferred to the Y_j (or X_j) subshell with the energy difference transferred to an ejected Z_k subshell electron which is ejected leaving a vacancy in the Z_k subshell. The exchange process whereby the original X_i vacancy is transferred to the Z_k subshell with the energy difference transferred to an ejected Y_j (or X_j) subshell electron is indistinguishable from the above process (called the direct process).

by ω_1 , a_1 , f_{12} , and f_{13} ; for the L_2 subshell by ω_2 , a_2 , and f_{23} ; and for the L_3 subshell by ω_3 and a_3 . The i th subshell fluorescence yield (ω_i) is the probability that a vacancy in the i th subshell is filled by a radiative transition (L_i x ray). The Auger yield (a_i) is the probability that a L_i subshell vacancy is filled by a nonradiative transition from a higher (M, N, etc.) major shell (Auger transition) and the Coster-Kronig transition probability (f_{ij}) is the probability for shifting a vacancy from the L_i subshell to the L_j subshell ($i > j$)*. These quantities are interrelated for an atom with a single L-shell vacancy as follows:

$$\omega_1 + a_1 + f_{12} + f_{13} = 1 \quad (2)$$

$$\omega_2 + a_2 + f_{23} = 1 \quad (3)$$

$$\omega_3 + a_3 = 1 \quad (4)$$

In addition to these fundamental relations, several quantities have been defined for singly-ionized atoms that

*The Coster-Kronig transition probability (f_{ij}) has a small radiative component [$f_{ij}(R)$]. Thus,

$$f_{ij} = f_{ij}(NR) + f_{ij}(R) \quad (5)$$

The radiative component of f_{23} has been demonstrated to be negligible both experimentally and theoretically (42).

are useful from an experimental standpoint. These are the mean L-subshell fluorescence yield (v_i), the mean L-shell fluorescence yield ($\bar{\omega}_L$), and the average L-shell fluorescence yield following K x-ray emission (ω_{KL}).

The mean L-subshell fluorescence yield (v_i) is the total number of all L x rays emitted per L_i vacancy*. The mean L-shell fluorescence Yield ($\bar{\omega}_L$) is the probability that an L x ray is emitted due to any primary L-shell vacancy. The following equations relate the above quantities to the fundamental quantities:

$$v_1 = \omega_1 + f_{12}\omega_2 + (f_{13} + f_{12} + f_{23})\omega_3 \quad (6)$$

$$v_2 = \omega_2 + f_{23}\omega_3 \quad (7)$$

$$v_3 = \omega_3 \quad (8)$$

$$\bar{\omega}_L = N_1v_1 + N_2v_2 + N_3v_3 \quad (9)$$

$$\omega_{KL} = N_2v_2 + N_3v_3 \quad (10)$$

where N_i is the normalized primary vacancy distribution**

*The difference between v_i and ω_i for the i th subshell is: ω_i only includes x rays that go to the L_i subshell, while v_i includes all x rays that result from an initial i th subshell vacancy (these include L_k x rays that are a result of the L_i-L_k X or L_i-L_j X and L_j-L_k X Coster-Kronig processes).

**The primary vacancy distribution for the L shell is the vacancy distribution after reorganization of the K shells but before reorganization within the L shell.

$(N_1 + N_2 + N_3 = 1)$. In the specialized case of ω_{KL} ,
 $N_1 = 0$, $N_2 = I_{K_{\alpha_2}} / I_{K_{\alpha}}$, and $N_3 = I_{K_{\alpha_1}} / I_{K_{\alpha}}$ where $I_{K_{\alpha_1}}$, $I_{K_{\alpha_2}}$,
 and $I_{K_{\alpha}}$ are the intensities of the K_{α_1} transition, K_{α_2}
 transition, and the total K_{α} transition ($I_{K_{\alpha_1}} + I_{K_{\alpha_2}} = I_{K_{\alpha}}$),
 respectively.

CHAPTER II

THEORETICAL BACKGROUND

Theoretical calculations of the radiative and non-radiative (Coster-Kronig and Auger) partial level widths* (Γ_R , Γ_{CK} , and Γ_A , respectively) are generally treated separately, since they originate from basically different interactions. The quantities ω_i , f_{ij} , and a_i are defined in terms of the partial level widths:

$$\omega_i = \Gamma_R(i)/\Gamma_t(i) \quad (11)$$

$$f_{ij} = \Gamma_{CK}(ij)/\Gamma_t(i) \quad (12)$$

and

$$a_i = \Gamma_A(i)/\Gamma_t(i) \quad (13)$$

where \underline{i} is the particular subshell ($i = 1, 2, 3$)** and the total level width $\Gamma_t = \Gamma_R + \Gamma_{CK} + \Gamma_A$, [$\Gamma_{CK} = \sum_{i>j}^3 \Gamma_{CK}(ij)$].

* The partial level widths (actually full widths at half maximum) are all related to the decay probability (per unit time) by a definition based on the Heisenberg uncertainty principle [i.e., $\Gamma_R = \hbar/\tau_R$, etc. where $1/\tau_R$ is the radiative decay probability (per unit time), τ_R is the mean radiative life, and \hbar is Planck's constant divided by 2π].

**

For $i = 3$, f_{ij} is meaningless.

The transition probability per unit time from state i to state f (w_{fi}) can be derived from elementary time-dependent perturbation theory (43) and is given by Fermi's "Golden Rule No. 2":

$$w_{fi} = (2\pi/\hbar) | H_{fi} |^2 \rho_f \quad (14)$$

where H_{fi} is the matrix element of the interaction Hamiltonian H' for the transition $i \rightarrow f$ ($H_{fi} = \int \psi_f^* H' \psi_i d\tau \equiv \langle \psi_f | H' | \psi_i \rangle$, where ψ_f and ψ_i are the wave functions for the final and initial states, respectively) and ρ_f is the density of final states with energy appropriate for the conservation of energy. The appropriate matrix elements for radiative and nonradiative transitions together with the density of final states can be substituted into eq. (14) multiplied by \hbar and summed over all allowed final states to obtain the partial level widths (e.g., $\Gamma_R(i) = \hbar \sum_f w_{fi}$). A discussion of the recent theoretical approaches to calculate the L-subshell yields is given in the following sections preceded by a discussion of the transition probabilities, wave functions, and energetics as they apply to recent L-subshell yield calculations.

2.1 Radiative Transition Probabilities

Theoretical L-subshell yield calculations have been performed recently using both relativistic (20-22) and non-relativistic (17, 18) theories to calculate the radiative

transition probabilities. In the high-Z region relativistic calculations should be superior to nonrelativistic calculations, but the magnitude of the relativistic effects may be sufficiently small enough not to produce an appreciable effect on the calculated L-subshell yields. A review of both relativistic and nonrelativistic theories is given below.

2.1.1 Nonrelativistic Radiative Transition Probabilities

The nonrelativistic expression for the radiative transition probability is normally given in terms of a multipole expansion. Terms corresponding to magnetic dipole (M1), electric quadrupole (E2), magnetic quadrupole (M2), and higher order terms (E3, M3, etc.) contribute less than 0.1 percent to the expansion^{*}; therefore, the radiative transition probability for the transition (W_{fi}) is given to high accuracy by the electric dipole (E1) term:

$$W_{fi} = \frac{32}{3} \frac{\pi^3 \nu^3}{\hbar c^3} \left| \langle \Psi_f \left| e \vec{r} \right| \Psi_i \rangle \right|^2 \quad (15)$$

where ν is the frequency of the radiation ($\Delta E = h\nu$), c is the speed of light, \hbar is Planck's constant divided by 2π , e is the electronic charge, \vec{r} is the position vector of the electron involved in the transition, and Ψ_i and Ψ_f are the initial and final state wave functions, respectively. The

^{*}The absence of terms corresponding to M1, M2, and E2 transitions is due to the fact that the wavelength of the emitted radiation is much greater than characteristic atomic dimensions.

selection rule for the E1 transition is $\Delta\ell = \pm 1$ where ℓ is the orbital angular momentum quantum number*.

2.1.2 Relativistic Radiative Transition Probabilities**

Expansion of the appropriate relativistic expressions in terms of multipoles gives the following expressions for the spontaneous radiative transition probability (10):

$$\omega_{fi} = 4\pi\alpha\omega_0 \sum_{L=1}^{\infty} \sum_{M=-L}^L \left\{ \left| \langle \psi_f^* | \vec{\alpha} \cdot \vec{A}_{LM}(m) | \psi_i \rangle \right|^2 + \left| \langle \psi_f^* | \vec{\alpha} \cdot \vec{A}_{LM}(e) | \psi_i \rangle \right|^2 \right\} \quad (16)$$

where $\vec{A}_{LM}(m)$ and $\vec{A}_{LM}(e)$ are the vector potential of the emitted wave for magnetic and electric multipoles (10, 48):

$$\vec{A}_{LM}(m) = i(2/\pi)^{1/2} j_L(kr) [L(L+1)]^{-1/2} \vec{L} Y_{LM}(\hat{r}) \quad (17)$$

and

$$\vec{A}_{LM}(e) = (2/\pi)^{1/2} \omega_0^{-1} [L(L+1)]^{-1/2} \vec{\nabla} \times \vec{L} j_L(kr) Y_{LM}(\hat{r}) \quad (18)$$

and where α is the fine structure constant, ω_0 is the circular frequency of the photon, $\vec{\alpha}$ is the Dirac matrix for the electron undergoing the transition ($\psi_i \rightarrow \psi_f$), $\vec{L} = -i\vec{r} \times \vec{\nabla}$, $Y_{LM}(\hat{r})$ is a spherical harmonic, and $J_L(kr)$ is a spherical Bessel function of the first kind.

* Discussions of radiative transitions in terms of multipole fields can be found in Refs. (44-47).

** In this section atomic units are used ($\hbar = c = m_0 = 1$).

Considering only single-particle electron states in a spherically symmetric potential and averaging over the magnetic quantum numbers of the final state, one obtains the following expression:

$$W_{fi} = 2\alpha\omega_0^2 \int_L [\omega_0^{-1} B(-\kappa_i, \kappa_f, L) R_L^2(m) + \omega_0^{-1} B(\kappa_i, \kappa_f, L) R_L^2(e)] \quad (19)$$

where B is a function of the Clebsch-Gordon coefficients and Racah Coefficients, κ_i and κ_f are quantum numbers which characterize the initial and final angular-momentum states ($\kappa \equiv -(\ell + 1)$ for $S = + 1/2$; $\kappa \equiv + \ell$ for $S = - 1/2$ or $\ell = \kappa$ if $\kappa > 0$ or $\ell = -\kappa - 1$ if $\kappa < 0$), and the R's are the Dirac radial matrix elements. Expressions for the Dirac radial matrix elements can be found in Refs. (10, 15).

2.2 Nonradiative Transition Probabilities

An outline of the theory of the nonrelativistic radiationless transition probability, first formulated by Wentzel (49), is given below, since all of the current L-subshell yield calculations are based on nonrelativistic theory. Clear discussions of relativistic nonradiative transition probabilities, first formulated by Møller (50), are given in Bambynek et al. (15), Burhop and Asaad (14), and Rose (48).

Wentzel (49) showed that the Auger and Coster-Kronig transitions arise from the electrostatic interaction between

two electrons ($H' = \sum_{i>j}^{N-1} e^2/r_{ij}$ where $r_{ij} = |\vec{r}_i - \vec{r}_j|$) in an atom in an initial state of single ionization* to give a doubly ionized final state of equal energy.

Substituting the interaction potential into eq. (14), one gets an expression for the probability of the radiationless transition from state \underline{i} to state \underline{f} :

$$\omega_{fi} = 2\pi \hbar^{-1} |\langle \Psi_f^* | \sum_{i>j}^{Z-1} e^2/r_{ij} | \Psi_i \rangle|^2 \rho_f \quad (20)$$

where Ψ_i are the $Z-1$ electron wave functions, given by the Slater determinant of the initial atomic state and Ψ_f are the $Z-1$ electron wave functions of the final state, an atom with two vacancies and the ejected Auger electron. The orthogonality and normalization properties of initial and final single-particle wave functions of which Ψ_i and Ψ_f are composed enable one to reduce eq. (20) to an equation containing a matrix element of two-electron configurations:

$$\omega_{fi} = 2\pi \hbar^{-1} |\langle \Psi_f(1,2) | e^2/r_{12} | \Psi_i(1,2) \rangle|^2 \rho_f \quad (21)$$

where

$$\Psi_f(1,2) = 1/\sqrt{2} [\psi_a(1)\psi_b(2) - \psi_a(2)\psi_b(1)] \quad (22)$$

*The condition of being initially singly ionized is not a general condition imposed by the definition of the Auger transition, Coster-Kronig transition, or the interaction, but is required by the present definition of L-subshell yields.

$$\Psi_i(1,2) = 1/\sqrt{2} [\psi_c(1)\psi_d(2) - \psi_c(2)\psi_d(1)] \quad (23)$$

ψ_b is the continuum wave function and ψ_a , ψ_c , and ψ_d are the bound-state wave functions. Introduction of the anti-symmetric wave functions into eq. (21) gives an equation of the form:

$$w_{fi} = 2\pi \hbar^{-1} |D - E|^2 \rho_f \quad (24)$$

where

$$D = \langle \psi_a^*(1)\psi_b^*(2) | e^2/r_{12} | \psi_c(1)\psi_d(2) \rangle \quad (25)$$

is the direct matrix element corresponding to the transition $\psi_c \rightarrow \psi_a$ and $\psi_d \rightarrow \psi_b$ and where

$$E = \langle \psi_a^*(2)\psi_b^*(1) | e^2/r_{12} | \psi_c(1)\psi_d(2) \rangle \quad (26)$$

is the exchange matrix element corresponding to the transition $\psi_d \rightarrow \psi_a$ and $\psi_c \rightarrow \psi_b$. Normalization of the bound-state wave functions to unity and normalization of the continuum wave function to yield one electron per unit time (51, 52) yields an expression for the density of the final states ($\rho_f = \hbar^{-1}$). Substituting \hbar^{-1} for ρ_f into eq. (24) yields an equation for the transition probability:

$$w_{fi}^{NR} = \hbar^{-2} |D - E|^2 \quad (27)$$

which is used in the current calculations.

The total transition rate for the nonradiative process ($\tau_{NR}^{-1} = \Gamma_{NR}/\hbar$) is a properly weighted sum of w_{fi}^{NR} for all the allowed radiationless transitions. In the nonrelativistic limit, transitions are allowed that have identical initial and final state symmetries, L, S, J, and parity π . These results can be stated in the form of the following selection rules

$$\Delta L = \Delta S = \Delta J = 0, \pi_i = \pi_f \text{ (yes)} \quad (28)$$

2.3 Wave Functions

The present discussion is intended to give merely an outline of the wave functions used in the various recent approaches (17, 18, 20-22) to calculating L-subshell yields.

2.3.1 Screened Nonrelativistic Hydrogenic Wave Functions

The screened nonrelativistic hydrogenic bound-state wave functions are found by solving the familiar Schrödinger equation for an electron in the field of a nucleus of charge Z^*e and of infinite mass:

$$\nabla^2 \psi + 2m_0/\hbar^2 (E + Z^*e^2/r) \psi = 0 \quad (29)$$

or in atomic units:

$$\nabla^2 \psi + 2(E + Z^*/r) \psi = 0 \quad (30)$$

After eq. (30) has been transformed into spherical polar coordinates, a separation of variables is possible. The solution is given by:

$$\psi_{n\ell m}(r, \theta, \phi) = R_{n\ell}(r) Y_{\ell m}(\theta, \phi) \quad (31)$$

where \underline{n} , ℓ , and \underline{m} are the principal, orbital angular momentum, and magnetic quantum numbers, respectively, $R_{n\ell}(r)$ is the radial eigenfunction, and $Y_{\ell m}(\theta, \phi)$ is a Legendre spherical harmonic.

The radial eigenfunctions and spherical harmonics are tabulated in standard texts on quantum mechanics. A thorough treatment of hydrogenic wave functions has been given by Bethe and Salpeter (53).

The results obtained using screened hydrogenic wave functions are critically dependent upon the choice of the screening constant σ ($Z^* = Z - \sigma$). The Hartree recipe is generally used. In this approach σ is derived from the ratio of the mean hydrogenic radius \bar{r}_H to the mean radius \bar{r}_{SCF} computed from self-consistent field (SCF) wave functions:

$$\sigma = Z - \bar{r}_H / \bar{r}_{SCF} \quad (32)$$

Since the screening constant σ depends on the quantum numbers \underline{n} and ℓ , the screened hydrogenic wave functions are not necessarily orthogonal. The single-electron wave function always has this inherent difficulty. The use of a single effective charge[†] Z' has given better results (54,15).

[†]The quantity Z' is a geometric mean of charges appropriate to contribution of various electron shells that enter into the problem.

The Gordon wave function (55, 52) is generally used as the continuum wave function along with the screened hydrogenic wave functions in calculations of nonradiative transition probabilities (56, 57, 20, 21). This wave function is a solution of the Schrödinger equation in a Coulomb potential of an effective point charge Z^*e with proper normalization (one electron per unit time). A selection of the appropriate effective charge is difficult and critical (see Kostroun, Chen, and Crasemann (57) for a discussion of this point).

Crasemann and coworkers (20, 21, 22) used the non-relativistic screened hydrogenic bound state wave functions and Gordon (Coulomb continuum function with an effective Z) continuum wave functions to calculate the Coster-Kronig and Auger partial level widths. These nonradiative widths were combined with the radiative level width calculations of Scofield (10, 58) (see Sects. 2.1.2 and 2.3.2) to derive the L-subshell yields. The nonradiative matrix elements were computed using jj-coupling (see Sect. 2.4 for more details). The energy of the ejected electron $E(V_i - X_j - Y_k)$ was approximated by the formula:

$$E(V_i - X_j - Y_k) = BE(V_i, Z) - BE(X_j, Z) - BE(Y_k, Z + 1) \quad (33)$$

where Z is the atomic number of the atom undergoing re-organization, $BE(V_i, Z)$ and $BE(X_j, Z)$ are the binding energies of the V_i and X_j subshells of element Z , and $BE(Y_k, Z + 1)$ is

the binding energy of the Y_k subshell of element $Z+1$. The binding energies were taken from the tabulation of Bearden and Burr (59). Further discussion of ejected-electron energies is given in Sect. 2.5.

2.3.2 Numerical Wave Functions

The calculations of McGuire (17,18), Chen and Crasemann (22), and Scofield (10, 58) are based on the Hartree-Fock-Slater (HFS) approach using the central field approximation. The radial HFS one-electron wave function for orbitals of principal quantum number n and orbital angular momentum quantum number ℓ are written in the form (atomic units are used):

$$[d^2/dr^2 - \ell(\ell+1)/r^2 - V(r) + E_{n\ell}]P_{n\ell}(r) = 0 \quad (34)$$

where $P_{n\ell}(r) = r R_{n\ell}(r)$, $R_{n\ell}(r)$ is the radial wave function, r is the magnitude of the radial vector, $E_{n\ell}$ is the energy eigenvalue, and $V(r)$ is the central atomic potential.

The above works differ in their selection of the central atomic potential. Chen and Crasemann (22) used an analytical independent-particle model potential given by Green, Sellin, and Zachor (GSZ) (60). McGuire (17, 18) used a nonrelativistic Herman-Skillman (HS) potential (61), and Scofield (10, 58) chose a relativistic HS potential.

The GSZ potential is given by:

$$V(r) = 2r^{-1}(NT - Z) \quad (35)$$

where

$$T = 1 - [(e^{r/d} - 1)^H + 1]^{-1} \quad (36)$$

where Z is the atomic number, $N = Z - 1$ is the number of core electrons, and \underline{d} and $H = d\alpha_0 N^{0.4}$ are adjustable parameters. Values of \underline{d} and α_0 are found by a least-squares fit of GSZ potential eigenvalues to the Hartree-Fock (HF) eigenvalues. The quantity \underline{d} is adjusted for each element and is tabulated by Green, Sellin, and Zachor (60). A value of $\alpha_0 = 1.00$ is found for HF models.

In the approach used by Chen and Crasemann, the continuum wave functions were determined by numerically solving the HFS radial wave equation using the GSZ potential. The energy of the ejected electron was estimated by the $\Delta Z = 1$ approximation (i.e., eq. 33) using binding energies from electron spectroscopy for chemical analysis (ESCA) tables (62). The calculations were carried out in jj -coupling (see Sect. 2.4). The values of the nonradiative level widths calculated for the L_2 subshell were combined with the L_2 -subshell radiative level widths calculated by Scofield (10, 58) to derive the L_2 -subshell yields ω_2 and f_{23} .

The nonrelativistic HS potential is given by:

$$\begin{aligned} V(r) &= V_0(r) \quad \text{for } r < r_0 \\ V(r) &= -2(Z-N+1)/r \quad \text{for } r \geq r_0 \end{aligned} \quad (37)$$

where Z is the atomic number, N is the number of electrons, r is the magnitude of the radial vector, and r_0 is defined by the relation $V_0(r_0) = -2(Z - N + 1)/r_0$. The quantity $V_0(r)$ is given by:

$$V_0(r) = -2Z/r - (2/r) \int_0^r \sigma(t) dt - 2 \int_r^\infty \sigma(t) dt/t - 6[-3/(8\pi) \rho(r)]^{1/3} \quad (38)$$

where t is the summation parameter, and $\rho(r) = (4\pi r^2)^{-1} \sigma(r)$ is the spherically averaged total electronic charge density. The quantity $\sigma(r)$ is given by:

$$\sigma(r) = - \sum_{n\ell} \omega_{n\ell} [P_{n\ell}(r)]^2 \quad (39)$$

where $\omega_{n\ell}$ is the occupation number for the orbital $n\ell$ [given by $2(2\ell + 1)$ for closed shells], and $P_{n\ell}(r)$ are the normalized radial wave functions.

The four terms in the expression for $V_0(r)$ (eq. 38) are due to the nuclear Coulomb potential (first term); the total electronic Coulomb potential, inner shielding (second term), outer shielding (third term); and the exchange potential (fourth term).

The form of eq. (37) is due to Latter (63). In the initial form of this equation, $V(r)$ was set equal to $V_0(r)$ for all r . This approximation is known as the free-electron approximation, but it breaks down at large distances from

the nucleus due to the cancellation of the nuclear Coulomb potential by the total electronic Coulomb potential. Then the potential reduces to the free-electron exchange potential which approaches zero at large \underline{r} . Instead of a zero potential at large \underline{r} , the electron moves effectively in the field of a singly-charged positive ion; thus the potential must approach $-2/r$ at large values of \underline{r} .

McGuire (17, 18) has calculated both radiative and nonradiative partial level widths using seven straight lines (64, 17) to approximate the quantity $-rV(r)$ for the HS potential. Auger partial level widths were calculated using LS-coupling. The ejected electron energies for the Auger transitions were taken from the energy eigenvalues obtained from the approximated HS potential. For the Coster-Kronig transition $V_i-X_iY_j$ the energy of the ejected electron $E(V_i-X_iY_j)$ is given by:

$$E(V_i-X_iY_j) = BE(V_i, Z) - 1/2 [BE(X_i, Z) + BE(X_i, Z+1) + BE(Y_j, Z) + BE(Y_j, Z+1)] \quad (40)$$

where the terms are previously defined.

Herman and Skillman (61) used perturbation methods to obtain relativistic and spin-orbit coupling corrections* to order α^2 . The Schrödinger radial wave equation is given by:

*The quantity α^2 is the perturbation parameter; $\alpha = 1/137$ is fine structure constant.

$$[H_0(r) + H_m(r) + H_d(r) + H_{SO}(r)]R(r) = ER(r) \quad (41)$$

where $R(r)$ and E are two-component radial wave functions and energy values, respectively, and $H_0(r)$ is the nonrelativistic Hamiltonian operator given by:

$$H_0(r) = -1/r^2 (d/dr) (r^2 d/dr) + V(r) + \ell(\ell+1)/r^2 \quad (42)$$

The quantities $H_m(r)$, the relativistic variation of mass with velocity; $H_d(r)$, the relativistic Darwin (65) correction and $H_{SO}(r)$, the spin-orbit energy are given by:

$$H_m(r) = -(\alpha^2/4) [E^\circ - V(r)]^2 \quad (43)$$

$$H_d(r) = -(\alpha^2/4) [dV(r)/dr] (d/dr) \quad (44)$$

$$H_{SO}(r) = -(\alpha^2/4) [f(\ell)] (1/4) [dV(r)/dr] \quad (45)$$

where E° is the zero order (nonrelativistic) energy eigenvalue, $f(\ell) = [0 \text{ for } \ell = 0; -\ell \text{ for } j = \ell + 1/2 \text{ and } \ell > 0; \ell + 1 \text{ for } j = \ell - 1/2 \text{ and } \ell > 0]$. The Darwin correction is positive for orbitals with $\ell = 0$ and zero for all orbitals with $\ell > 0$ when $V(r) = -Z/r$ (Coulomb potential).

The relativistic version of the HS potential was used by Scofield (10,58) to calculate the radiative partial level widths. This same model with the inclusion of the effects of finite nuclear size was used by Rosner and Bhalla (66) to calculate K-shell radiative partial level widths.

These agreed with Scofield's work to approximately 0.1 percent for all Z.

2.4 Coupling

The nonrelativistic Hamiltonian for an atom is given by:

$$H = H_0 + H_C + H_{SO} \quad (46)$$

where H_0 corresponds to the hydrogenic Hamiltonian, H_C is the Coulomb interaction of electron pairs, and H_{SO} is the spin orbit interaction. The coupling scheme depends on the relative magnitudes of H_C and H_{SO} ($H_C \gg H_{SO}$:LS-Coupling; $H_C \gg H_{SO}$:jj-coupling; and $H_C \approx H_{SO}$:intermediate coupling).

The quantum numbers \underline{n} and \underline{l} characterise a vacancy in the LS-coupling scheme (e.g. $2p$ or $L_{2,3}$). In LS-coupling the electrostatic interaction splits the final two hole configurations into terms of different energies characterized by L and S. These terms are given by the notation ^{2S+1}L (e.g. 1P). The quantum numbers \underline{n} , \underline{l} , and \underline{j} characterize a vacancy in jj-coupling. Terms for jj-coupling are given by $n\underline{l}_j$ (e.g. $2p_{1/2}$ or L_2). In intermediate coupling a double-vacancy state is characterized by L, S, and J. The notation is given by $K-L_1L_{2,3}(^1P_1)$ if the coupling is approached from pure LS-coupling, or the notation is given by $K-L_1L_2(^1P_1)$ if it is approached from pure jj-coupling.

Much experimental and theoretical work has been done to investigate the various coupling schemes. Most of this

work has been confined to the K-series Auger lines at low- and intermediate-Z values. Little work has been done on the L series at medium to high atomic numbers ($Z > 60$). The experimental and theoretical work on L-Augur spectra has been summarized by Haynes (67). He found that the theoretical work of McGuire (68) using jj-coupling was in reasonable agreement with experiment at high-Z values, but a tendency toward intermediate coupling was found at medium-Z values.

All of the present work on Coster-Kronig yields has used the jj-coupling approximation.

It should be noted that the fluorescence yields are independent of the coupling scheme used, since the total nonradiative transition rates in the various schemes are related by unitary matrix transformations (69).

2.5 Energetics

Calculations of the Auger and Coster-Kronig rates are fairly insensitive to the ejected-electron energy (70, 71)* except very near thresholds**. Near threshold it is

* Callan (72) concluded that Coster-Kronig transition rates are sensitive to the ejected-electron energy but he did not give any information to prove this. The work of Yin et al. at $Z = 30$ (71) showed that the $L_2-L_3M_{4,5}$ Coster-Kronig transitions are insensitive to ejected-electron energy except very near thresholds.

** Here, the term "threshold" means the energy region (determined by Z) in which a transition becomes energetically allowed (i.e., the transition $L_2-L_3M_5$ becomes energetically allowed near $Z = 91$).

possible to estimate that a transition is energetically forbidden (i.e., the estimate of the ejected electron energy is less than or equal to zero) when it is actually allowed. Such a mistake can cause a large error in theoretical calculations of f_{23} , since the theoretical calculations of f_{23} do not include all of the allowed transition probabilities. McGuire (18) predicted that the $L_2-L_3M_4$ transition is not allowed at $Z = 94$ while experiments indicate that this transition is, in fact, allowed (73).

The ejected-electron energy is given by different expressions in different coupling schemes. Much work has been done on the energetics of the K-LL transitions using the LS-, intermediate-, and jj-coupling schemes (14, 74). Most of the work on the L-series nonradiative transitions has used the jj-coupling approximation. Since the energy formulas are only critically important near threshold, and since the present work is primarily concerned with the $L_2-L_3M_4$ and $L_2-L_3M_5$ thresholds at high Z , use of the jj-coupling approximation in this work is valid.

In the jj-coupling approximation the energy of the ejected Auger or Coster-Kronig electron $E(V_i-X_jY_k)$ is given by:

$$E(V_i-X_jY_k) = BE(V_i, Z) - BE(X_j, Z) - BE(Y_k, Z) - \Delta BE(X_jY_k, Z) \quad (47)$$

where $BE(V_i, Z)$, $BE(X_j, Z)$, and $BE(Y_k, Z)$ are the binding energies of the V_i , X_j , and Y_k subshells of atomic number Z , respectively; Z is the atomic number of the atom in which the transition takes place; and $\Delta BE(X_j, Y_k, Z)$ can be considered as a measure of the increase in the X_j and/or Y_k binding energies caused by the doubly ionized final state.

A crude estimate of the ejected-electron energy is given by:

$$E(V_i - X_j, Y_k) = BE(V_i, Z) - BE(X_j, Z) - BE(Y_k, Z+1) \quad (48)$$

where $BE(Y_k, Z+1)$ is the Y_k subshell binding energy of atomic number $Z+1$ and all other terms are as defined previously.

Other estimates of the ejected-electron energy have been given:

$$E(V_i - X_j, Y_k) = BE(V_i, Z) - BE(X_j, Z) - (1 - \Delta Z) BE(Y_k, Z) - \Delta Z BE(Y_k, Z+1) \quad (49)$$

or

$$E(V_i - X_j, Y_k) = BE(V_i, Z) - BE(X_j, Z+1) - BE(Y_k, Z) \quad (50)$$

where ΔZ is a fitted constant which can be derived from measured values of ejected-electron energies. This constant (ΔZ) is associated with the change in the charge state of the atom due to the ejection of the electron. Eq. (49) is due to Bergström and Hill (75) while eq. (50) is due to

McGuire (76, 18).

It is evident that eqs. (48-50) are unrealistic, since the direct $V_i-X_jY_k$ and exchange $V_i-Y_kX_j$ processes are equivalent, and these equations give different values of ejected-electron energies for the equivalent processes. Albridge and Hollander (77) rectified this mistake by using the formula:

$$E(V_i-X_jY_k) = BE(V_i, Z) - (1-\Delta Z') [BE(X_j, Z) + BE(Y_k, Z)] - \Delta Z' [BE(X_j, Z+1) + BE(Y_k, Z+1)] \quad (51)$$

where $\Delta Z'$ is an adjustable parameter determined from measured ejected-electron energies. McGuire (17, 18) used eq. (51) with $Z' = 1/2$, while Crasemann and coworkers (20, 21, 22) used eq. (48).

A discussion of these equations as they apply to this experimental work will be given in Sect. 6.3.

2.6 Concluding Remark on the Theoretical Background

Owing to the diversity of the previous sections a summary of the principal theoretical L-subshell yield calculations would be useful.

McGuire (17, 18) calculated L-subshell yields for the L_1 , L_2 , and L_3 subshells; used an approximate non-relativistic Herman-Skillman potential with jj-coupling to obtain numerical wave functions; and used eq. (51) with

$\Delta Z' = 0.5$ to predict the Coster-Kronig ejected-electron energies.

Crasemann and coworkers (20, 21) calculated L-subshell yields for the L_1 , L_2 , and L_3 subshells; used non-relativistic screened hydrogenic wave functions with jj-coupling to calculate the Auger and Coster-Kronig transition probabilities; used the radiative transition probabilities calculated by Scofield; and used eq. (48) to predict the Coster-Kronig ejected-electron energies.

Scofield (10, 58) calculated radiative transition probabilities using a relativistic Herman-Skillman potential.

Chen and Crasemann (22) calculated L-subshell yields using the IPM with a GSZ potential and jj-coupling to obtain numerical wave functions to calculate Auger and Coster-Kronig transition probabilities, used the radiative transition probabilities calculated by Scofield, and used eq. (48) to predict the Coster-Kronig ejected-electron energies.

How well these various theoretical approaches agree with each other is discussed in Sects. 6.2 and 6.3 below, together with comparisons with experiment.

CHAPTER III

VACANCY CREATION PROCESSES AND CHOICE OF EXPERIMENTAL
METHODS

In order to discuss L-subshell yields, it is necessary to understand the various methods of measurement and processes by which electron vacancies are created, and to select the most appropriate process.

3.1 Summary of Vacancy Creation Processes

Since the choice of a particular vacancy creation process greatly influences the accuracy and selectivity of an experiment, the various processes of vacancy creation should be carefully considered. Subsequent to initial vacancy creation by one of the three ionization processes, i.e., fluorescent excitation, charged particle bombardment, or radioactive decay, the initial vacancies are shifted by radiative x-ray transitions and, in addition, are multiplied by the nonradiative processes (Auger and Coster-Kronig transitions). Since this vacancy reorganization is a function of Z for a given initial single vacancy, the only control over the final vacancy distribution lies in the choice of the initial vacancy creation process. These processes and their relationship to the L shell are considered in detail below.

3.1.1 Fluorescent Excitation

The direct fluorescent excitation (photoionization) method is of great interest historically, since the first fluorescence yield measurement (2) and the first systematic $\bar{\omega}_L$ measurements (23) were performed using this method. In photoionization, only single vacancies are created by exposing a thin target to x rays or γ rays. The primary L-subshell vacancy distribution (n_1, n_2, n_3) can be determined by observing the ejected L-shell photoelectrons, or by observing $K_{\alpha_{1,2}}$ x rays in a K_{α} x-ray-L x-ray coincidence experiment [e.g. Jopson et al. (28, 29)]. In principle the vacancy distribution can be calculated from the relative photoionization cross sections, which requires an accurate knowledge of the subshell photoelectric cross sections, which are not currently available. All published data on photoelectric cross sections consist either of total cross sections (78-80) or major-shell (81) cross sections, rather than subshell cross sections.

Uncertainties in the measured L-subshell yields are introduced in methods using fluorescent excitation due to the compromise in choice of target thickness. The target must be of sufficient thickness to produce an appreciable number of observable events, but such a thickness will seriously attenuate the L x-ray intensity, corrections for which introduce a large uncertainty in the result. Additional uncertainties are introduced by self-excitation

of the foil and by scattering of the incident and emitted radiation.

In the photoelectric process, vacancies can be formed predominantly in the L_3 subshell without ionizing the L_1 or L_2 subshells by a proper selection of the excitation energy.

3.1.2 Charged Particle Excitation

Inner-shell vacancies can be created by electron, proton, or heavy-ion beams. The use of energetic electrons is severely limited by bremsstrahlung which obscures the emitted L x rays. The use of protons or heavy ions to create vacancies is complicated by the creation of multiply ionized species (82). In addition, reliable calculations of the primary vacancy distribution are limited by inaccuracies in the knowledge of ionization cross sections for heavy ions. For this reason, this process is rarely employed for the present type of experiment.

3.1.3 Radioactive Decay

Atomic vacancies are produced in radioactive decay processes, such as electron capture and internal conversion. In the electron capture process, the initial vacancy distribution is dictated by the decay energy (Q_{EC}) and the transition selection rules. When Q_{EC} is sufficiently greater than the K shell binding energy (B_K), most (approximately 90 percent) of the vacancies are produced in the K shell. These primary K-shell single vacancies subsequently shift to the three L-subshells (see Sect. 3.1.4). In the case of pure L

capture, when $B_L < Q_{EC} < B_K$, primary vacancies are created predominantly in the L_1 subshell*. Accurate values of the electron capture probabilities for the various shells and subshells (P_K , P_{L_1} , P_{L_2} , and P_{Total}) can be calculated using the tables given by Behrens and Bühring (83), Zyryanova and Suslov (84), or Martin and Bilchert-Toft (85).

Vacancies produced by internal conversion can be calculated using experimental internal conversion coefficients** (86) or theoretical internal conversion coefficients (87, 88). These coefficients are a function of atomic number, transition energy, and multipolarity of the transition.

Low energy ($E \approx 50$ keV) E2 γ -ray transitions fed by even-even alpha-emitting heavy nuclei are of interest, since they provide a source of primary L_2 - and L_3 -subshell vacancies. The normalized primary vacancy distribution ($N_1:N_2:N_3$) is approximately 0.02:0.52:0.46. These transitions have been studied to find values of ω_2 and f_{23} or ω_2 and ω_3 (26, 38, 89-94).

*The ratio P_{L_2}/P_{L_1} is less than 0.15 if Q_{EC} is sufficiently greater than the L_3 binding energy, while the ratio P_{L_3}/P_{L_1} is negligible, thus pure L capture can be a source of L_1 subshell vacancies.

**The internal conversion coefficient (α_{X_i}) is defined as the number of γ rays emitted in a nuclear transition divided by the number of X_i subshell conversion electrons emitted.

3.1.4 Indirect Vacancy Creation

In addition to the three methods of direct vacancy production above, one or more vacancies can be created in the L shell due to shifts of an initial vacancy from the K shell. These shifts occur either by x-ray or Auger transitions.

The radiative shift occurs predominantly by the K_{α_2} ($K-L_2$) or K_{α_1} ($K-L_3$) transitions, since the ($K-L_1$) radiative transition is forbidden by the electric dipole selection rule, $\Delta l = \pm 1^*$. The nonradiative shifts occur by means of the Auger transitions $K-L_iL_j$ and $K-L_iX$, where X refers to an outer shell electron (M, N, ...), and result in a doubly-ionized atom.

The very useful quantity, n_{KL_1} , the number of L_1 subshell vacancies produced in the filling of a K-shell vacancy, is given by the following relations:

$$n_{KL_1} = (1-\omega_K) \left\{ \frac{2I(K-L_1L_1) + I(K-L_1L_2) + I(K-L_1L_3) + I(K-L_1X)}{I(K-L_1L_1) + I(K-L_1L_2) + I(K-L_1L_3) + I(K-L_1X)} \right\} \quad (52)$$

$$n_{KL_2} = \frac{\omega_K I(K_{\alpha_2})}{I(K)} +$$

$$(1-\omega_K) \left\{ \frac{2I(K-L_2L_2) + I(K-L_1L_2) + I(K-L_2L_3) + I(K-L_2X)}{I(K-L_1L_1) + I(K-L_1L_2) + I(K-L_1L_3) + I(K-L_1X)} \right\} \quad (53)$$

* The radiative $K-L_1$ transition intensity is finite due to magnetic dipole admixture but is of negligible intensity(10).

$$n_{KL_3} = \frac{\omega_K I(K_{\alpha_1})}{I(K)} + (1-\omega_K) \left[\frac{2I(K-L_3L_3) + I(K-L_1L_3) + I(K-L_2L_3) + I(K-L_3X)}{I(K-LL) + I(K-LX) + I(K-XY)} \right] \quad (54)$$

where $I(\dots)$ represents the intensity of the x-ray or Auger transition shown in parenthesis; X and Y refer to shells higher than the L shell (M, N, ...) and $I(K)$ refers to the total intensity of all of the K x rays ($K_{\alpha} + K_{\beta}$). Calculations of n_{KL_i} can be found in Rao et al. (95) and Bambynek et al. (15).

3.1.5 Vacancy Creation as Presently Used

Creation of atomic vacancies by radioactive decay processes is chosen for the present work. The L-subshell vacancies are produced indirectly from radiative vacancy shifts, i.e., the K_{α_2} and K_{α_1} radiative transitions. This method provides an adequate number of vacancies without the problems of scattering and self-absorption which are inherent in the fluorescent excitation method. In addition, the fate of individual subshell vacancies can be studied. The K_{α_1} and K_{α_2} x rays effectively "tag" L_3 - and L_2 -subshell vacancies, respectively.

3.2 Summary of Experimental Methods of Measuring

L-Subshell Yields

The methods used for measuring L-shell yields fall

into two basic techniques: Singles-spectrum methods and coincidence methods. In addition to this distinction, the methods can be classified into high or low resolution techniques*.

3.2.1 Singles Methods

The singles method relies on the ability to measure the intensity of a designated x-ray emission. With low resolution, mean L-shell fluorescence yields ($\bar{\omega}_L$) are measured by relating the total number of L x rays (I_{LX}) or the total number of L-Auger electrons (I_{LA}) to some other event that can be normalized to a known primary vacancy distribution. Such normalizing events are frequently K x rays (31, 96-100), although other possibilities exist (e.g.

* High resolution in the present context means that for K x rays the K_{α_1} and K_{α_2} lines are resolved, and that for L x rays the principal x-ray transitions feeding vacancies in the L_1 , L_2 , and L_3 subshells are resolved, i.e., the L_{α} , L_{β} , and L_{γ} x rays. Common high resolution x-ray detectors include modern Ge(Li), Ge(HP) (i.e., high purity germanium), Si(Li), and crystal diffraction spectrometers. Low resolution in the present context means for K x rays that only K_{α} and K_{β} are resolved while the major L x-ray transitions are not resolved (i.e., L_{α} , L_{β} , and L_{γ} x rays are an unresolved multiplet). Common low resolution x-ray detectors include NaI(Tl) (i.e., thallium activated sodium iodide) scintillators and older Ge(Li) and Si(Li) semiconductor detectors.

L-shell conversion electrons or γ rays)*.

It is also possible to count both the L-Auger electrons and the L x rays to obtain the total number of L-shell vacancies (101-103), $\bar{\omega}_L = I_{LX}/(I_{LX}+I_{LA})$.

With high resolution it is possible to determine L-shell fluorescence yields and/or Coster-Kronig transition probabilities. In each measurement it is frequently necessary to assume critical parameters which are not measured with the same apparatus (26, 38, 39, 89-92, 104). For details and equations, see Bambynek et al. (15). Singles methods have been applied to the low-energy E2 transition fed by even-even alpha-emitting heavy nuclei (38, 93, 94). Since this technique is a modification of the general α -particle-L x-ray coincidence technique, it is treated in Sect. 3.2.2.3.

In addition to the above singles methods, Auger-electron and photoelectron spectroscopy have been used to obtain qualitative information concerning the L_2 - L_3 Coster-

*When the K x rays are used as the normalizing events, $\bar{\omega}_L$ is given by:

$$\bar{\omega}_L = \omega_K (I_{LX}/I_{KX}) [N_K(T)/N_L(T)] \quad (55)$$

where $N_K(T)$ and $N_L(T)$ are the total number of K and L shell vacancies, I_{KX} is the intensity of the K x rays, and all other quantities are as previously defined. The quantities $N_K(T)$ and $N_L(T)$ can be calculated using equations given by Nix, McGeorge, and Fink (99).

Kronig transition probability (f_{23}) at low atomic numbers ($Z \approx 30$) (71, 105). Since those techniques are only qualitative and the results are not directly applicable to this study, they will not be discussed in detail.

3.2.2 Coincidence Techniques

A K_{α_1} x-ray signals the direct transfer of an initial K-shell vacancy to the L_3 subshell. When the L x-rays resulting from the radiative filling of this secondary L_3 -subshell vacancy are detected in coincidence with the K_{α_1} x ray, it is possible to examine the K- L_3 transition separately from other transitions leading to L x-ray emission. Similarly, a K_{α_2} x-ray-L x-ray coincidence separates events relating to the L_2 subshell, since the K_{α_2} x ray represents the K- L_2 vacancy transfer. Because the electromagnetic radiative transition probability is essentially zero for K- L_1 (1s \rightarrow 2s) transitions, there is no K x ray emitted which can serve as a signal for creation of an L_1 subshell vacancy. In this case, one may, in the radioactive gamma decay of certain nuclides, use the L_1 -conversion electron to signal creation of L_1 -subshell vacancies, and examine in coincidence the resulting L x rays. Thus, by appropriate coincidence gating (involving K_{α_1} or K_{α_2} x rays on $Ce_{L_1}^-$ electrons), it is possible with present detector resolution to separate from the total emission of L x rays those arising from each of the three L subshells and to investigate them individually.

The coincidence technique was first used to isolate

L-shell vacancies by Lazar and Lyon in 1958 (27). Since that time many advances in technique and equipment (30, 33, 37, 106) have permitted the study of individual subshell vacancies and thus to measure directly L-subshell quantities. In the following sections each coincidence technique is discussed in detail.

3.2.2.1 K_{α} X-Ray-L X-Ray Coincidences. The information on the L shells that can be obtained depends on the resolution of the detectors used. If low-resolution detectors are used to observe both K and L x rays, only a mean yield (i.e., ω_{KL}) can be determined:

$$I_{L(K_{\alpha})} = C'_{K_{\alpha}} \omega_{KL} \quad (56)$$

where $I_{L(K_{\alpha})}$ is the intensity of L x rays in coincidence with K_{α} x rays per unit time and $C'_{K_{\alpha}}$ is the counting rate of K_{α} x-ray gating events.

When K_{α_1} and K_{α_2} are resolved*, but L x rays are not resolved, ω_3 and ν_2 can be measured:

$$I_{L(K_{\alpha_1})} = C'_{K_{\alpha_1}} \omega_3 \quad (57)$$

$$I_{L(K_{\alpha_2})} = C'_{K_{\alpha_2}} \nu_2 = C'_{K_{\alpha_2}} (\omega_2 + f_{23} \omega_3) \quad (58)$$

*The K_{α} x-ray-L x-ray coincidence technique in which K_{α_1} and K_{α_2} are resolved will be denoted as the $K_{\alpha_{1,2}}$ x-ray-L x-ray coincidence technique.

Experiments which resolve K_{α_1} , K_{α_2} , and the L x rays into groups which correspond to transitions to the L_1 , L_2 , and L_3 subshells are capable of determining ω_2 , ω_3 , and f_{23} . The appropriate equations are:

$$I_{L_2-X(K_{\alpha_2})} = C'_{K_{\alpha_2}} \omega_2 \quad (59)$$

$$I_{L_3-X(K_{\alpha_1})} = C'_{K_{\alpha_1}} \omega_3 \quad (60)$$

and

$$I_{L_3-X(K_{\alpha_2})} / I_{L_3-X(K_{\alpha_1})} = (C'_{K_{\alpha_2}} / C'_{K_{\alpha_1}}) f_{23} \quad (61)$$

or

$$I_{K_{\alpha_2}(L_3-X)} / I_{K_{\alpha_1}(L_3-X)} = (C_{K_{\alpha_2}} / C_{K_{\alpha_1}}) f_{23} \quad (62)$$

where $C_{K_{\alpha_1}}$, $C_{K_{\alpha_2}}$, etc., are the singles counting rates; other symbols are as previously defined.

3.2.2.2 Conversion-Electron-L X-Ray Coincidence.

The detection of conversion electrons (Ce^-) can be used to signal vacancies in the L shell or L_i subshell if the resolution of the instrument is sufficient. The L_i -subshell conversion electron energy ($E_{Ce_{L_i}^-}$)* is characteristic of the L_i subshell.

* $E_{Ce_{L_i}^-} = E_{\gamma} - B_{L_i}$ where E_{γ} is the nuclear transition energy (i.e., γ -ray energy) and B_{L_i} is the L_i -subshell binding energy.

This technique was used by Boyer and Barat (107) to obtain a mean L-shell fluorescence yield for $Z = 91^*$. The results were given by the relation:

$$I_{L(\text{Ce}_L^-)} = C_{\text{Ce}_L^-}' \bar{\omega}_L \quad (63)$$

Wood et al. (108) and Rao et al. (37) performed additional measurements using a cooled Si(Li) x-ray spectrometer to detect the L-shell conversion electrons. Results for the L subshell were obtained using L_2^- and L_3^- -subshell information derived from $K_{\alpha_{1,2}}$ x-ray-L x-ray coincidences.

Recently, Campbell et al. (106) used this method to obtain L_2^- and L_3^- subshell results for $Z = 88$ and 94 . A $\pi\sqrt{2}$ β spectrometer was used to select the individual L_2^- and L_3^- subshell conversion electrons from low-energy E2 transitions (the parents were high-Z even-even α emitters). Eqs. (59-61) apply in this case except that the K_{α_1} and K_{α_2} gates are replaced by $\text{Ce}_{L_3}^-$ and $\text{Ce}_{L_2}^-$ gates, respectively. This method has wide applicability in the high-Z region and is potentially very precise. It is a vastly superior alternate to the α -particle-L x-ray coincidence technique (39) (see Sect. 3.2.2.3).

* No reliable subshell yields were obtained since the L-conversion electron spectrum was not resolved by their electrostatic spectrometer. (The quantities ω_2 and ω_3 were calculated using the erroneous assumption that $f_{23} = 0$ and assuming a ratio of $\alpha_{L_2}/\alpha_{L_3}$).

3.2.2.3 α -Particle-L X-Ray Coincidences. Much work has been done using L x-ray spectra gated by an α particle which feeds a converted E2 gamma transition in the daughter atom (26, 89-92), or the singles adaptation of this technique (38, 93, 94), at high atomic numbers. This technique is based on the fact that many even-even α -emitting nuclei with $Z \geq 86$ decay predominantly to the first excited state (2+) of the daughter. This state is approximately 50 keV above the ground state and cannot convert in the K shell, since K-shell binding energy is approximately 100 keV. Such nuclear transitions are classified as electric quadrupole (2+ \rightarrow 0+) transitions (E2) and have a ratio of conversion coefficients ($\alpha_{L_1}:\alpha_{L_2}:\alpha_{L_3}$) of approximately 3:104:96, and thus these transitions provide a source of essentially pure L_2 and L_3 vacancies. Owing to the high atomic numbers of the radioactive nuclides ($Z \geq 86$) used, semiconductor detectors can resolve the L x-ray groups filling the L_2 or L_3 subshells.

The subshell yields f_{23} and ω_2 are given by the following equations (assuming that L_1 vacancies are negligible):

$$f_{23} = (\omega_2/\omega_3) F'_3 - C'_3 \quad (64)$$

$$\omega_2 = F(1+C'_3)/\{[\alpha_L/(1+\alpha_T)][1+F'_3]\} \quad (65)$$

where:

$$C'_3 = N_3/N_2 = \alpha_3/\alpha_2 \quad (66)$$

$$F = I_{L(\alpha)}/C'_\alpha = \omega_2 N_2 + \omega_3 (N_3 + f_{23} N_2) \quad (67)$$

$$F'_3 = I_{L_3}/I_{L_2} = \omega_3 (N_3 + f_{23} N_2) / (\omega_2 N_2) \quad (68)$$

The above notation is that given by Ross et al. (109) as modified by Salguero et al. (26).

This technique has the severe limitation that a value for ω_3 must be assumed in order to calculate f_{23} and ω_2 . The attainable accuracy in f_{23} is limited, since f_{23} is the small difference of two large terms [i.e., $(\omega_2/\omega_3)F'_3 \approx 1.05$; $C'_3 \approx 0.90$].

A modification of this technique can be used to derive ω_1 , ω_2 , and ω_3 if values for f_{ij} are assumed (93, 94). In this technique, the singles intensities of the L x rays and the E2 γ rays are measured at high resolution, and absolute L-subshell conversion coefficients (α_{L_1} , α_{L_2} , and α_{L_3}) as well as f_{ij} values are taken from the literature in order to derive ω_1 , ω_2 , and ω_3 . The equations which relate these quantities are:

$$\omega_1 = I_{L_1}/n_1 \quad (69)$$

$$\omega_2 = I_{L_2}/n_2 \quad (70)$$

and

$$\omega_3 = I_{L_3}/n_3 \quad (71)$$

where

$$n_1 = I_{\gamma} \alpha_{L_1} \quad (72)$$

$$n_2 = I_{\gamma} (\alpha_{L_2} + f_{12} \alpha_{L_1}) \quad (73)$$

and

$$n_3 = I_{\gamma} [\alpha_{L_3} + f_{23} \alpha_{L_2} + (f_{13} + f_{12} f_{23}) \alpha_{L_1}] \quad (74)$$

The limitation of this method lies in its dependence on absolute L-subshell conversion coefficients and, to a lesser degree, on its dependence on the Coster-Kronig yields, since the results are not strongly dependent on the latter.

3.2.2.4 γ -Ray-L X-Ray Coincidence. A γ -ray gated L x-ray spectrum can yield atomic information (ω_i 's and f_{ij} 's) when the gating γ ray is preceded or followed by a nuclear transition creating K- or L-shell vacancies. It should be noted that the primary L-shell vacancy distribution will be the weighted sum of the primary L-shell vacancy distributions of all the prompt nuclear events preceding and following the γ transition (nuclear cascading). Thus useful L-subshell information is usually derived from γ rays which are preceded only by a single, prompt nuclear event (frequently electron capture) (110-111), or followed only by a single, prompt nuclear event (frequently, a γ ray) (108). The coincidence

intensity per unit time $I_{L(\gamma)}$ is related to the mean L-shell fluorescence yield ($\bar{\omega}_L$) as follows:

$$I_{L(\gamma)} = C'_\gamma \bar{\omega}_L p_L \quad (75)$$

where C'_γ is the counting rate in the γ -ray gate and $p_L = P_L + n_{KL} P_K$, (P_L and P_K are the L and K capture probabilities, respectively) for the case of electron capture and $p_L = \alpha_L / (1 + \alpha_T) + n_{KL} \alpha_K / (1 + \alpha_T)$ for γ transitions. Useful L-subshell information can be derived when the vacancies are predominantly confined to a single subshell. This condition is fulfilled for certain classes of pure L capture and certain classes of pure L-shell conversion.

3.2.2.5 M X-Ray-L X-Ray Coincidence. In this technique the ratio of M x rays in coincidence with the L_2 - M_4 transition to the M x rays in coincidence with the L_3 - $M_{4,5}$ transitions are observed. From that ratio, f_{23} is calculated using the following relation*:

$$\frac{I_{M(L_2-N_{4,5})}}{I_{M(L_2-M_4)}} = \left[\frac{C'_{L_2-N_{4,5}}}{C'_{L_2-M_4}} \right] \left[\frac{n_2 f_{23} (1-R_2)}{n_2 f_{23} + n_3} \right] \left[\frac{\bar{\nu}_{4,5}^M}{\nu_4^M} \right] \quad (76)$$

where

* It should be noted that eq. (76) is the only one which contains M-shell quantities (i.e., $\bar{\nu}_{4,5}^M$ and ν_4^M); all other quantities are L-shell quantities.

$$n_2 = \alpha_{L_2} / (1 + \alpha_T) \quad (77)$$

$$n_3 = \alpha_{L_3} / (1 + \alpha_T) \quad (78)$$

$$R_2 = I_{L_2-L_3X} / (I_{L_2-L_3X} + I_{L_2-L_3M}) \quad (79)$$

and v_4^M and $\bar{v}_{4,5}^M$ are the mean M_4 subshell fluorescence yield and a weighted average of mean M_4 and mean M_5 subshell fluorescence yields, respectively. For further definitions of M-shell quantities, see Bambynek et al. (15).

From eq. (76) one can see that it is necessary to assume a value of R_2 from theory, since the energy of the $L_2-L_3^M$ Coster-Kronig transition is very low, and it has not been observed at high Z . This assumption introduces a large uncertainty into the value of f_{23} using this method. In addition, this method is not applicable when the $L_2-L_3^M$ transitions are energetically forbidden, since the term $(1-R_2)$ is then zero. It should be noted that the primary purpose of this type of experiment is not to determine the value of $f_{23}(112)$, but to investigate the "jump in f_{23} " at $Z \geq 90^*$.

3.2.2.6 K-Auger Electron-L X-Ray Coincidences. L x-ray spectra gated by K-Auger electrons gives information

* This increase in f_{23} ("jump in f_{23} ") is due to the onset of $L_2-L_3^{M_{4,5}}$ Coster-Kronig transitions which are forbidden for $30 \leq Z \leq 91$ (it should be noted that the limits are not exact).

about fluorescence yields of doubly ionized atomic states. Results of this type of work indicate that L-subshell fluorescence yields are not much influenced by a single vacancy in the M shell or higher shells, whereas double vacancies within the L shell increase the fluorescence yield appreciably (41, 113, 114).

3.3 Outline of the Present Experimental Method

Of the previously considered experimental techniques the $K_{\alpha_{1,2}}$ x-ray-L x-ray coincidence technique and the Ce_L^- -L x-ray coincidence technique are capable of the highest accuracy in determining L_2^- and L_3^- subshell yields. Application of the Ce_L^- -L x-ray coincidence technique is limited by the number of appropriate radioactive sources and by the availability of the electron spectrometer to detect the conversion electrons. The $K_{\alpha_{1,2}}$ x-ray-L x-ray coincidence technique was chosen to take advantage of the availability of appropriate radioactive sources and of high resolution Si(Li) and Ge(HP) detectors (see Sect. 4.2).

In the presently used $K_{\alpha_{1,2}}$ x-ray-L x-ray coincidence technique, the K x rays are detected using a Ge(HP) x-ray detector while the L x rays are detected in a Si(Li) x-ray detector (see Sect. 4.2). The Ge(HP) detector is used to detect K x rays since these detectors have a high efficiency and good resolution in the K x-ray region pertinent to this work (i.e., 60 - 100 keV). A Si(Li) detector was chosen as the L x-ray detector since such detectors have a fairly

slowly varying efficiency energy response in the L x-ray region studied in this work (i.e., 9 - 22 keV).

All events which are detected in the Ge(HP) detector and correspond to the energy of a K_{α_1} x ray or a K_{α_2} x ray are individually recorded. Such events are termed gate counts or gate events (see Fig. 2). The gate counts yield the quantities $C'_{K_{\alpha_2}}$ and $C'_{K_{\alpha_1}}$ [see eqs. (57-62)], after corrections for spurious events (see Sects. 3.2.2.1, 3.3.1, and 3.3.3). The L x-ray events which are detected in the Si(Li) detector in coincidence with a K_{α_1} or K_{α_2} event are recorded. Events following a K_{α_1} pulse are recorded separately from events following a K_{α_2} pulse. The L x-ray events are recorded as a spectrum. The L x-ray spectrum thus recorded is termed the coincidence spectrum (see Fig. 3). These spectra are analyzed to obtain the intensity of the L x rays which fill a particular L subshell (i.e., the quantities $I_{L_2-X(K_{\alpha_2})}$ and $I_{L_3-X(K_{\alpha_1})}$; see Sect. 3.2.2.1). corrections for spurious events in the coincidence spectrum must be made before the quantities $I_{L_2-X(K_{\alpha_2})}$ and $I_{L_3-X(K_{\alpha_1})}$ are determined (see Sect. 3.3.2). In summary, eqs. (59 - 62) have been used to calculate the results after corrections have been made for spurious events in the gate and in the coincidence spectrum; for angular correlation effects; and for efficiency. The principles of these corrections are given in Sects. 3.3.1 and 3.3.2.

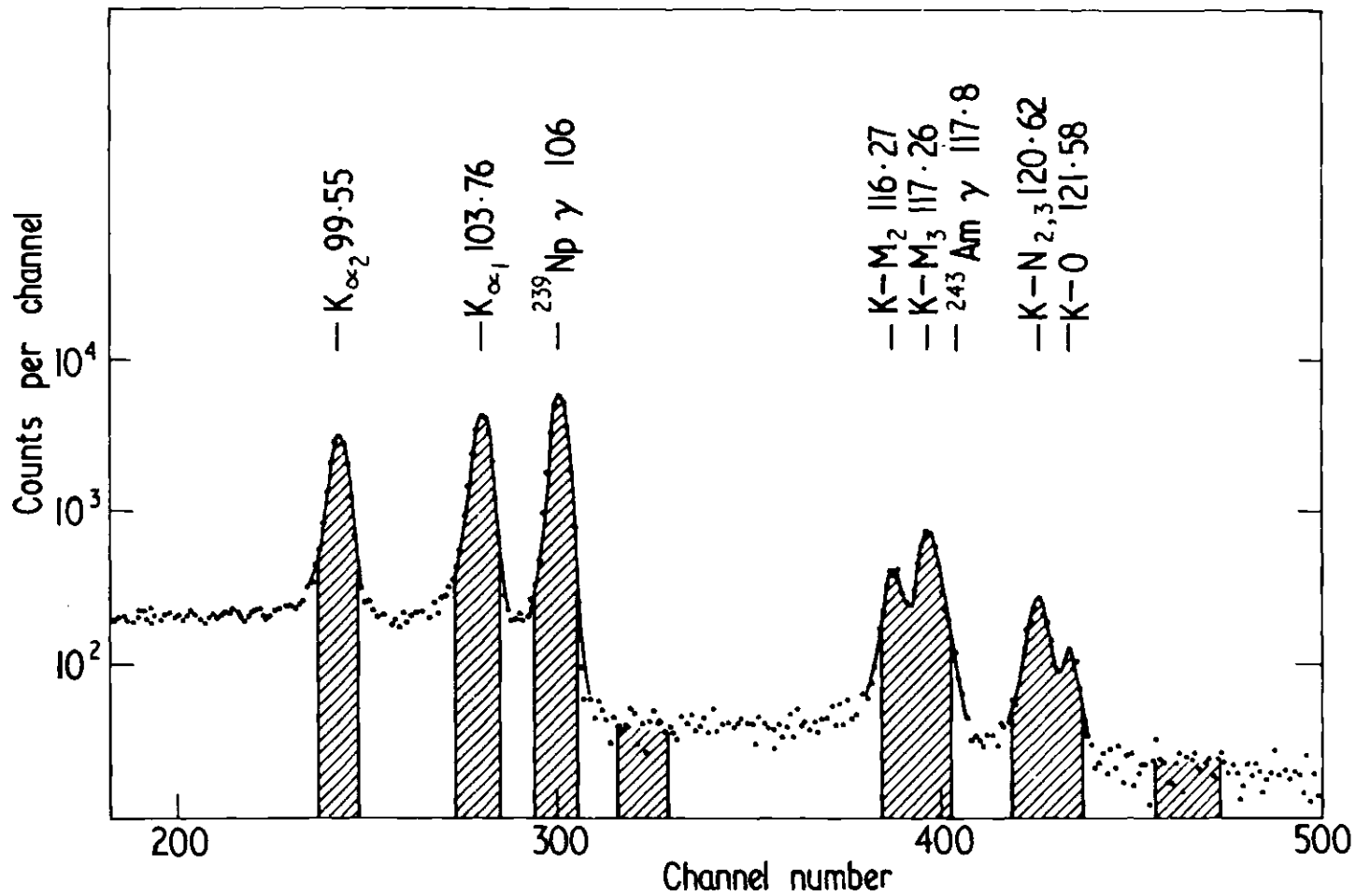


Figure 2. The Photon Spectrum of the Equilibrium $\text{Am}^{243}\text{-Np}^{239}$ Source Showing the Pu K X Rays. [Note the absence of K x-ray lines at 97.06, 101.05, and 113.8 keV characteristic of neptunium. The shaded areas indicate the gate settings and energies are given in keV. This figure is from Ref. (73) based on the present work.]

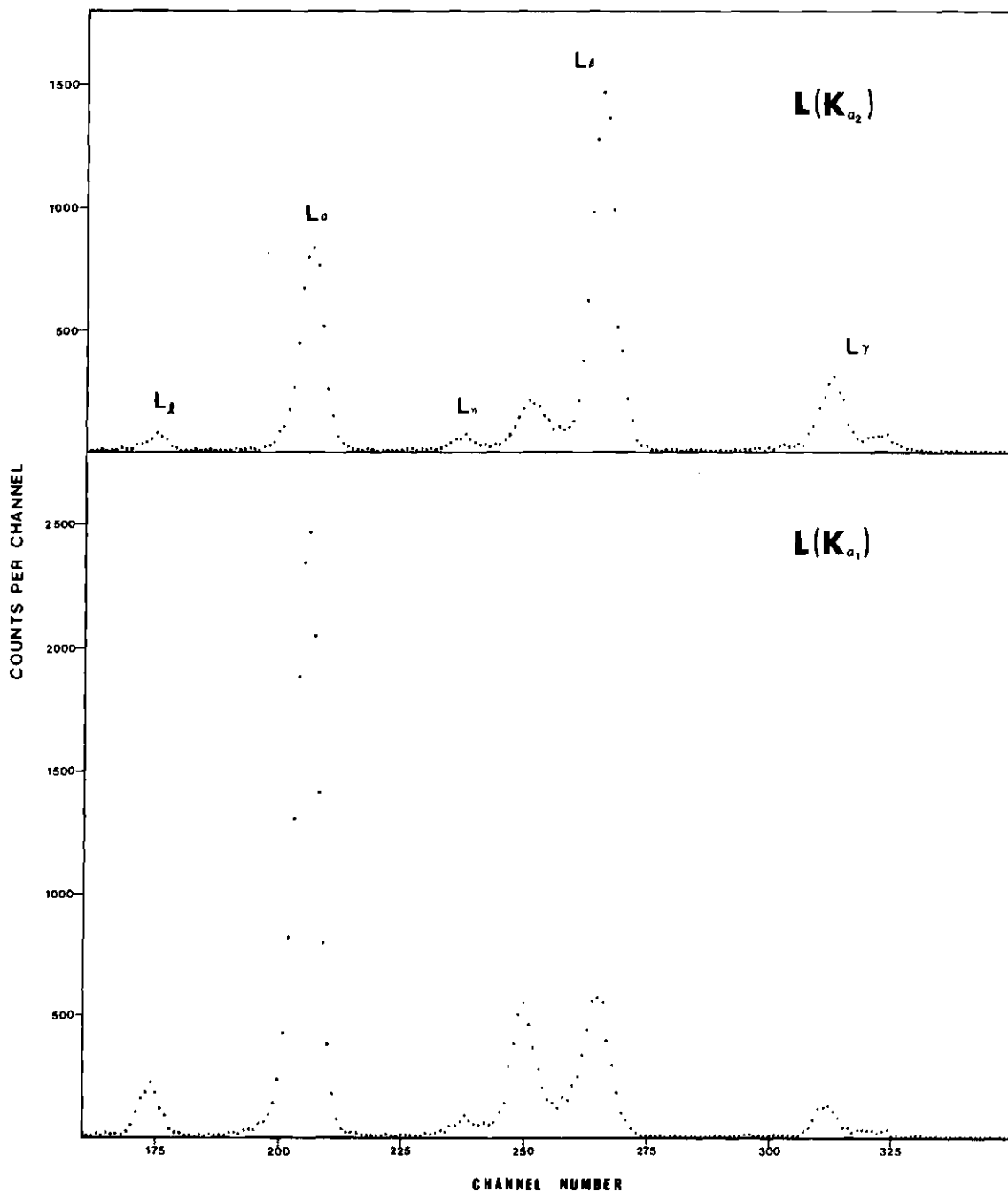


Figure 3. Pu L X Rays in Coincidence with K_{α_1} and K_{α_2} X-Ray Gate Pulses from the Equilibrium $\text{Am}^{243}\text{-Np}^{239}$ Source. [The L x-ray coincidence spectra gated by pulses from the K_{α_1} and K_{α_2} gates are designated by $L(K_{\alpha_1})$ and $L(K_{\alpha_2})$, respectively.]

3.3.1 Spurious Events in the Gate Counting Rate

The experimental gate counting rate $C'_g(E)$ is due to "true" events C'_g and spurious events $C'_g(I)$, [$C'_g(E) = C'_g + C'_g(I)$]. The latter are due to escape peaks, Compton scattering, degraded pulses from higher energy events ("tailing"), and unresolved lines. Such spurious events may be corrected for by fitting a single line of similar photon energy to each line which interferes with the gate and estimating its contribution to the gate. In the present experiments, the tailing of K_{α_1} into K_{α_2} , of L_β into L_α , the incomplete resolution of L_η and L_α , of L_α and L_β , and of K_{α_1} and K_{α_2} , and the escape of silicon K_α and K_β x rays* (this is a negligible effect) (115) are the major sources of impurities in the gates.

The correction for incomplete resolution of L_α and L_η x-ray groups is not generally made by line fitting techniques, but when L_α is used for the gate the correction is made by using the following equation:

$$\frac{C_{K_{\alpha_2}}(L_\alpha + kL_\eta)}{C_{K_{\alpha_1}}(L_\alpha + kL_\eta)} = C_{K_{\alpha_2}} / C_{K_{\alpha_1}} [f_{23} + k(\omega_2/\omega_3)(S_\eta/S_\alpha)] \quad (80)$$

where S_η is the radiative branching ratio of the L_2-M_1 x-ray

* If in the interaction of a L_γ x ray (at $Z \approx 60$) a silicon K_α or K_β x ray escapes, the event will be observed along with the L_α x rays.

transition ($S_{\eta} = I_{L_{\eta}}/I_{L_3-X}$); S_{α} is the radiative branching ratio of the $L_3-M_{4,5}$ x-ray transition ($S_{\alpha} = I_{L_{\alpha}}/I_{L_3-X}$); $C_{K_{\alpha_2}(L_{\alpha}+kL_{\eta})}$ and $C_{K_{\alpha_1}(L_{\alpha}+kL_{\eta})}$ are the coincidence counting rates; $C_{K_{\alpha_2}}$ and $C_{K_{\alpha_1}}$ are the singles counting rates; and k is the fraction of L_{η} x-ray events which are included in the L_{α} gate. Values of S_{η} and S_{α} can be obtained from the work of Scofield (10, 58).

3.3.2 Spurious Events in the Coincidence Spectrum

The spurious events in the coincidence spectrum are a result of chance coincidences^{*}, of nuclear cascading^{**}, and of coincidences from spurious events in the gate. The spurious events in the gate fall into two classes: (i) those which are coincident with lines in the coincidence spectrum (spurious coincidences) and (ii) those which are not in coincidence with lines in the coincidence spectrum (these can be considered as a part of the chance coincidence rate). Correction for spurious coincidences requires a knowledge of the intensity of the L x rays in coincidence with the

* Coincidence events which are due to the decay of two separate atoms are termed chance events. The probability of such an event being recorded is proportional to the counting rates (N_1, N_2) and resolving time of the system (i.e., to $2\tau N_1 N_2$).

** Cascading is a term applied to the process in which the gate pulse due to one nuclear event (e.g. an L x ray from electron capture) and the coincident spectral pulse due to another nuclear event (e.g. an L x ray from internal conversion) are in coincidence (cascade).

spurious event. This may necessitate the setting of another gate. The spurious spectrum is subtracted from the observed total gate spectrum with a proper normalizing factor (C'_g/C'_1), where C'_g and C'_1 are the counting rates of the gating events in the gate of interest and of the gate set on the spurious event, respectively.

Corrections for chance and cascading events are made by using the K_β subtraction method (116). The K_β subtraction method is based on the fact that only cascade and chance events are in coincidence with K_β (K-MN...) x rays. With this method a gate is set on K_β (usually K'_{β_1}), and all events in coincidence with K_β are recorded. When the $K_{\alpha_1,2}$ coincidence technique is employed, the K_β coincidence spectrum is subtracted from the K_{α_1} and K_{α_2} coincidence spectra (i.e., $L(K_{\alpha_1})$ and $L(K_{\alpha_2})$, respectively) using normalizing factors of $C'_{K_{\alpha_1}}/C'_{K_\beta}$ and $C'_{K_{\alpha_2}}/C'_{K_\beta}$, respectively. When the L_α group is used as the gate, the chance and cascade intensities $I^C_{K_{\alpha_1}}(L_\alpha)$ and $I^C_{K_{\alpha_2}}(L_\alpha)$ are given by:

$$I^C_{K_{\alpha_1}}(L_\alpha) = C_{K_{\alpha_1}} I_{K_\beta}(L_\alpha) / C_{K_\beta} \quad (81)$$

and

$$I^C_{K_{\alpha_2}}(L_\alpha) = C_{K_{\alpha_2}} I_{K_\beta}(L_\alpha) / C_{K_\beta} \quad (82)$$

where $I_{K_\beta}(L_\alpha)$ is the intensity of K_β events in coincidence

with L_α x rays, and $C_{K_{\alpha_1}}$, $C_{K_{\alpha_2}}$, and C_{K_β} are the K_{α_1} , K_{α_2} , and K_β singles counting rates, respectively.

When K_{α_1} and K_{α_2} x rays are used as gates and L_α and L_η x-ray groups are incompletely resolved, the following equation applies, from which f_{23} is evaluated:

$$\frac{I_{L_\alpha + kL_\eta}(K_{\alpha_2})}{I_{L_\alpha + kL_\eta}(K_{\alpha_1})} = (C'_{K_{\alpha_2}} / C'_{K_{\alpha_1}}) [f_{23} + k(\omega_3/\omega_2)(S_\eta/S_\alpha)] \quad (83)$$

3.3.3 Angular Correlation Corrections

Moellering and Jensen (117) first suggested that x-ray cascades should be angularly correlated. The theory was outlined by Moellering and Jensen (117) and Bambuskin (118). This correlation was experimentally verified by Beste (119) and Konstantinov and Sazonova (120).

Since this correction is small (15), only those factors directly applicable to K x-ray-L x-ray coincidences are given here; for a complete discussion of x-ray angular correlations, see Bambynek et al. (15).

Vacancy cascades of the type $I_k \rightarrow I \rightarrow I_f$ are isotropic (where \underline{i} refers to initial and \underline{f} refers to final spin states, respectively) when $I = 1/2$; therefore, all $K_{\alpha_1}(1s_{1/2} \rightarrow 2p_{3/2} \rightarrow I_f)$ x-ray-L x-ray coincidences result in anisotropic directional correlations and require correction. When the detectors are oriented at 180° to each other, this correction is given by:

$$I_{L_i-X(K_{\alpha_1})} = I_{L_i-X(K_{\alpha_1})}^U / [1 + A_{22} f(\theta)] \quad (84)$$

where $I_{L_i-X(K_{\alpha_1})}$ and $I_{L_i-X(K_{\alpha_1})}^U$ are the corrected and uncorrected L_i -x rays in coincidence with K_{α_1} x rays, respectively; A_{22} is a function of the angular momenta and of the multipolarities of the emitted radiations; A_{22} is also a product of $A_{K(1)}$ that depends on the first transition of the cascade and of $A_{K(2)}$ that depends on the second transition; and $f(\theta)$ is the finite solid angle correction (15). Values of A_{22} can be taken from experiment (15) or from theoretical values (58).

CHAPTER IV

SOURCES AND APPARATUS

4.1 Choice and Description of Radioactive Sources

The $\bar{\omega}_L$ measurements were made in the $47 \leq Z \leq 63$ region, since the K_{α_1} and K_{α_2} lines and the L_{α} , L_{β} , and L_{γ} lines are difficult to resolve in this region. Therefore, any results (i.e., L-subshell yields) which require these lines to be resolved are subject to large uncertainties.

The f_{23} measurements were made at $Z = 80, 81, \text{ and } 82$, in order to investigate the apparent discrepancy between the results obtained by the $K_{\alpha_{1,2}}$ gating method and the L_{α} gating method (see Sect. 6.3). In this Z region problems associated with resolving the K and L x-ray lines are minimal.

Nuclides for the $86 \leq Z \leq 94$ region were chosen in order to investigate the "jump in f_{23} " and also to measure L_{2^-} and L_{3^-} -subshell yields in this region.

The individual nuclides chosen for the $\bar{\omega}_L$ or f_{23} and/or ω_2 and ω_3 measurements have half-lives in range of several days to several years. These nuclides decay by electron capture and/or γ transitions which are appreciably converted. The energy of either of these processes is sufficient to produce K-shell vacancies. The nuclides had to be available either by loan from some other laboratory,

by direct purchase from a vendor, or by production in the Georgia Tech Research Reactor. In addition, the nuclides used for the L-subshell measurements must have decay schemes which produce a minimal amount of cascading. In certain cases, especially in the high-Z region, this requirement is relaxed, since few suitable radioactive sources exist and are difficult to obtain. Descriptions of the individual radioactive sources and their preparation are given below.

Thin uniform sources of Pm^{145} , Gd^{153} , Hg^{203} , Au^{198} , and Bi^{207} were prepared by insulin spreading of radiochemically pure, high specific activity solutions*. The solutions were drop evaporated onto 0.025 mm thick Mylar films. A drop of 1:20 insulin water provided a low-surface-tension substrate of area approximately equal to 0.25 cm^2 . The radioactive solutions were deposited with a micropipet directly onto the dilute-insulin-covered area and allowed to dry under a heat lamp. Typical source strengths were in the range of 1-5 microcuries (μCi).

The Cd^{109} source (15 μCi) was prepared by electroplated onto a thin backing in a spot of 5 mm diameter. The thickness of this source was not negligible and a correction for self-absorption of the L x rays was determined from conversion electron spectroscopy (100) (see Sect. 5.1).

* Obtained from New England Nuclear Corporation, Boston, Massachusetts.

An Am²⁴³-Np²³⁹ solution* (1μCi) was electroplated onto a thin sheet of aluminized Mylar in a spot of 7 mm diameter. A singles photon spectrum of this source showed the absence of Np K x rays (Fig. 2). The absence of Np K x rays is due to the lack of K shell conversion in Am²⁴³ decay.

A 410 day Np²³⁵ source was prepared from material produced at the Lawrence Livermore Laboratory by J. H. Landrum by a high intensity deuteron irradiation of highly purified, isotopically enriched U²³⁵ (121). The neptunium fraction was isolated at the Livermore Laboratory from the uranium target and fission and spallation products removed by a series of co-precipitations with LaF₃ and La(OH)₃, followed by anion exchange in an HCl medium. The final purification step entailed a solvent extraction using mono-octyl phosphate in toluene, thenoyltrifluoroacetone (TTA) in benzene, and diethyl ether as the extracting agent (122). The Np²³⁵ source was prepared by evaporation of a 10 μCi solution on a thin Mylar film.

The 27 day Pa²³³ sources were prepared in the present work by irradiating 30 mg of Th²³²(NO₃)₄·4H₂O in the Georgia Tech Research Reactor for two hours at a flux of 1.3×10^{13} thermal neutrons·cm⁻²·sec⁻¹. The 22 minute Th²³³ was allowed to decay to Pa²³³ for approximately one hour. The sample

* Purchased from the Transuranium Research Laboratory, Oak Ridge National Laboratory, Oak Ridge, Tennessee.

was dissolved in 1.5 ml of 4 M HNO_3 solution, and Pa^{233} was isolated by solvent extraction with 1.5 ml of 0.5 M TTA in benzene (123, 124). A single spectrum showed the absence of the 29.3 keV γ ray emitted in the decay of Th^{233} (125, 126) as a test of complete separation from thorium. Sources of Pa^{233} approximately 30 μCi in strength, were prepared by drop evaporation of the Pa^{233} activity in the TTA-benzene solution onto thin mylar film.

Radioactive sources for the $Z = 88$ and 86 work, sources of 18 day Th^{227} and 11 day Ra^{223} , respectively, were isolated by Dr. F. Tolea in our laboratory by solvent extraction with tributyl phosphate (127) from a solution of 21 year Ac^{227} * which contained an equilibrium mixture of daughter products.

Owing to the growth of the Ra^{223} decay product during the course of each run (approximately 2 days), Rn K x rays and the γ rays emitted in the decay of Ra^{223} also were present in the Ge(HP) spectra (Fig. 4), but the resolution was good enough to prevent the appearance of any appreciable unwanted contribution to the Ra K x-ray gate pulses from this source.

The solution remaining after extraction of Th^{227} was used to make sources for study of the K and L x rays characteristic of Rn. Since the Ac^{227} was not removed from the solution, the Th^{227} grew in (Fig. 5) during the runs,

*Obtained from New England Nuclear Corporation.

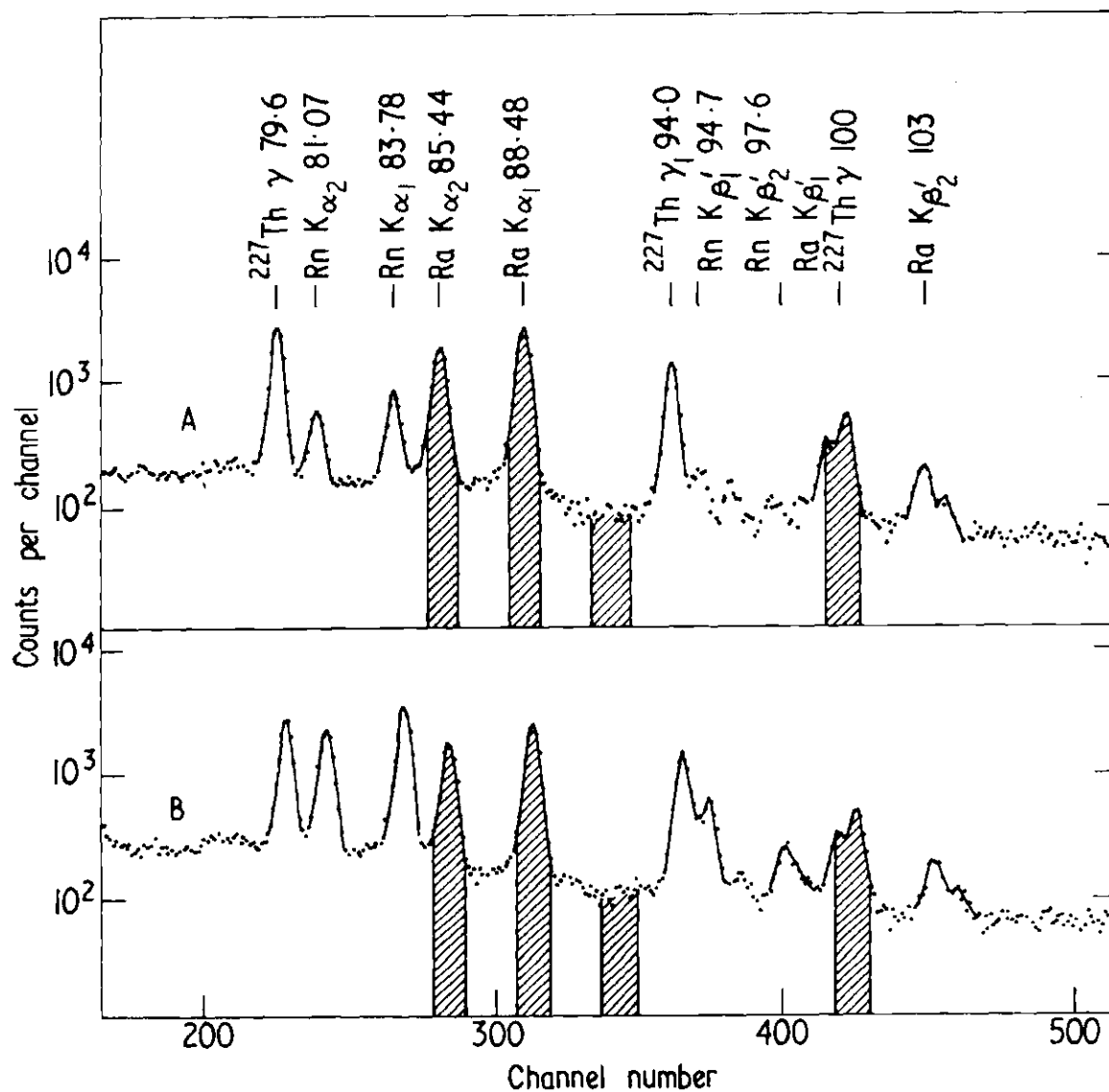


Figure 4. The Photon Spectrum in the K X-Ray Region of the Th^{227} Source. [Spectrum A was taken before a typical run and spectrum B, after the run, indicating growth (Rn K x rays) of the Ra^{223} daughter during the run. The shaded areas indicate the gates. This figure is from Ref. (73), based on the present work.]

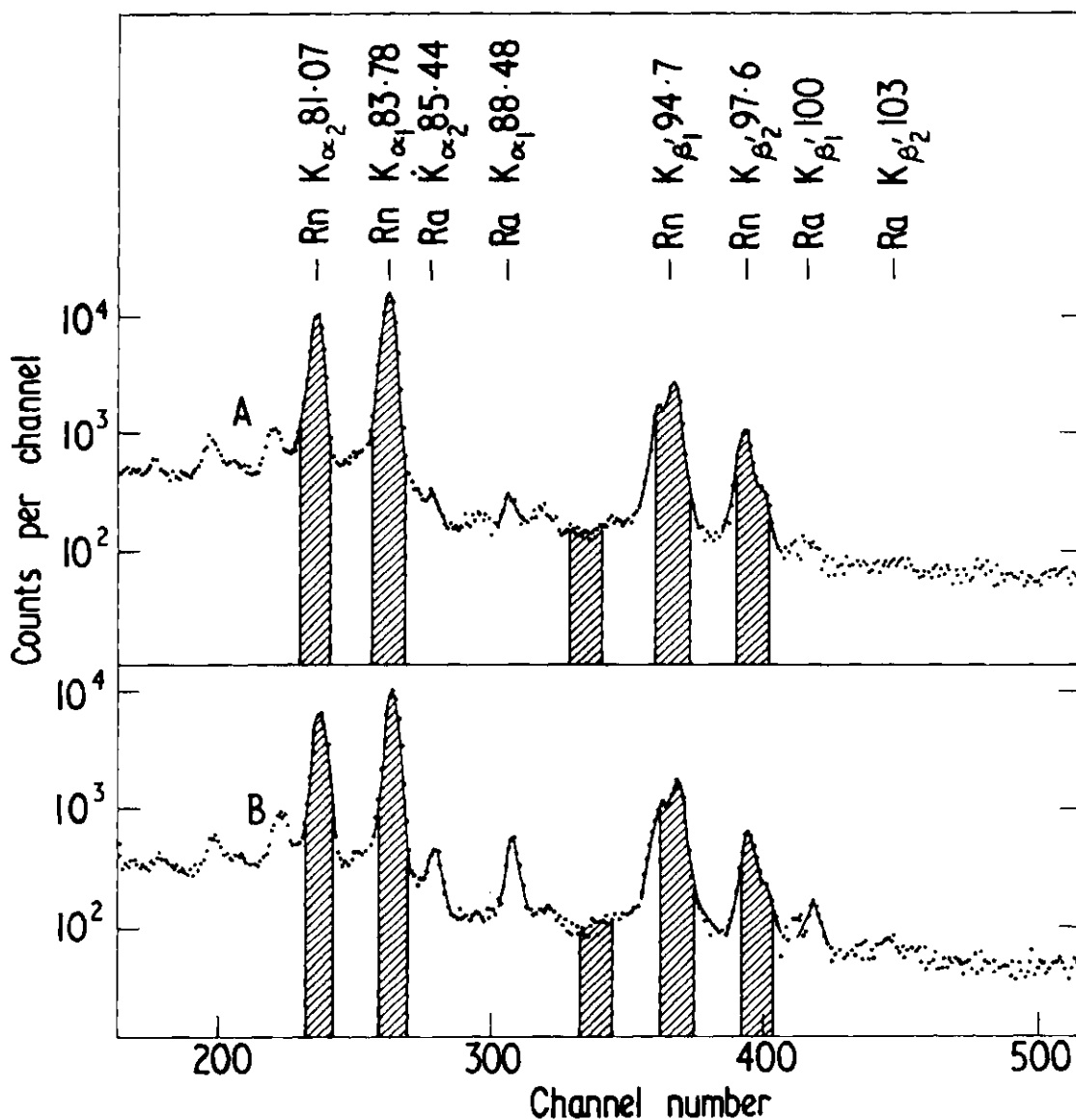


Figure 5. The Photon Spectrum in the K X-Ray Region of the Ac^{227} Source. [The Th^{227} daughter has been radiochemically extracted leaving Ra^{223} and its daughters in the source. Spectrum A is before and spectrum B is after a typical run for $Z = 86$ measurements. The shaded areas indicate the gates. This figure is from Ref. (73), based on the present work.]

but even after the run, the intensity of the Rn K x rays was greater than 15 times that of the Ra K x rays, and the presence of the latter did not disturb the measurement at $Z = 86$.

4.2 Detectors and Their Efficiencies

Three different detectors were used in the present work (Table 2). These detectors were selected for their high resolution and high detection efficiency.

Detector S1 was used in measurements of $\bar{\omega}_L$ and in measurements of f_{23} , ω_2 , and ω_3 at $Z = 86, 88, 92$ and 94 . Detectors S1 and S2 were used in f_{23} measurements at $Z = 80, 81, 82, \text{ and } 92$. Detector G1 was used in conjunction with detectors S1 and S2 in those experiments requiring coincidence measurements; i.e., in all of the L-subshell work.

Only the efficiency of detector S1 was determined especially for the present measurements (Fig. 6), since only the fluorescence yields are dependent on efficiency, whereas the determination of the Coster-Kronig transition probability f_{23} is independent of efficiency. The efficiency was determined using absolutely calibrated radioactive photon sources*, together with thin sources prepared in this laboratory. Further details of these measurements are given in Refs. (128, 129). It should be noted that the efficiency was determined before and after each fluorescence yield

* Provided by the International Atomic Energy Agency, Vienna (IAEA).

Table 2. Nominal Detector Specifications

Designation	Type	Preamplifier Type(Feedback)	Nominal Dimensions		Resolution(FWHM)		Manufacturer
			Depth (mm)	Diameter (mm)	5.9keV	122keV	
G1	Ge(HP)	Resistive	3.5	6	204ev	550ev	ORTEC
S1	Si(Li)	Pulsed-Optical	3.0	6	185ev	-	KEVEX
S2	Si(Li)	Pulsed-Optical	5.0	10	169ev	-	KEVEX

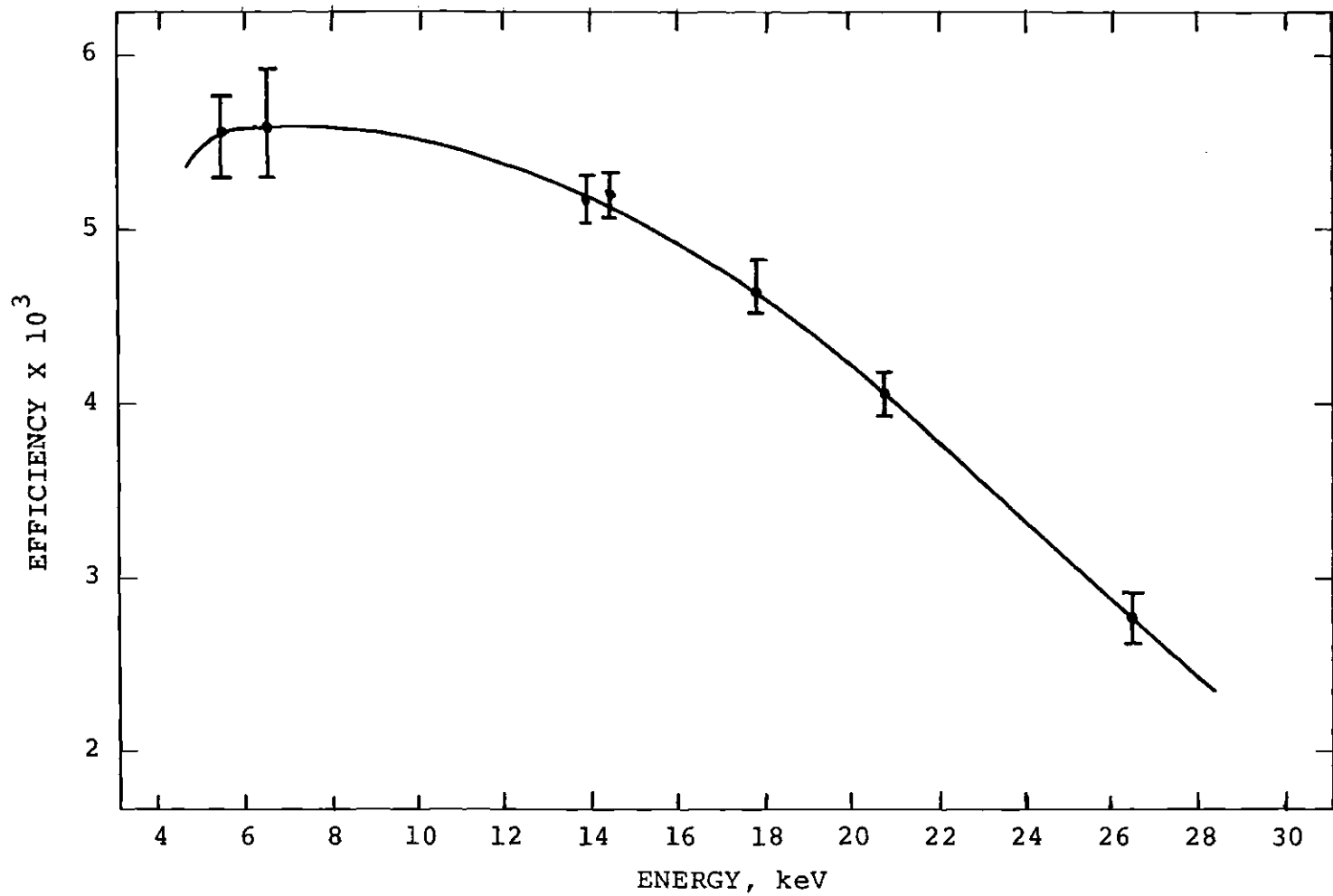


Figure 6. Experimental Detection Efficiency vs Energy for Detector S1.
 (The curve is established by the experimental points to an accuracy of ± 4 percent.)

measurement and Fig. 6 serves as a typical example of these determinations.

4.3 Electronic Equipment

The quantity $\bar{\omega}_L$ was measured in singles experiments with detector S1, and a Tennelec TC-202-BLR linear amplifier with baseline restoration, and a 2048-channel (Nuclear Data ND-2200) analyzer (MCA).

The coincidence experiments employed a standard fast-slow coincidence system with a time-to-amplitude converter (TAC) used as the coincidence unit. The fast branches of the coincidence systems are designed to measure accurately the time relationship of the pulses in the two detectors, while the slow branches of the coincidence systems are designed to optimize the energy resolution.

For the coincidence studies at $Z = 82, 86, 88, 92,$ and $94,$ a single-parameter system with fourfold routing into a Nuclear Data (ND-2200) 2048-channel analyzer was employed (see Fig. 7). Additional coincidence experiments at $Z = 80, 81, 82,$ and 92 were performed using a dual-parameter Nuclear Data (ND-4420) multiparameter analyzer (MPA) (see Fig. 8) which became available at a later date.

4.3.1 Single-Parameter Coincidence System

In the fast branch of the single-parameter coincidence system, the signals from the preamplifiers formed the input to the fast amplifiers (F-AMP) whose signals were fed to the start input of the TAC on the gate side and to the stop input

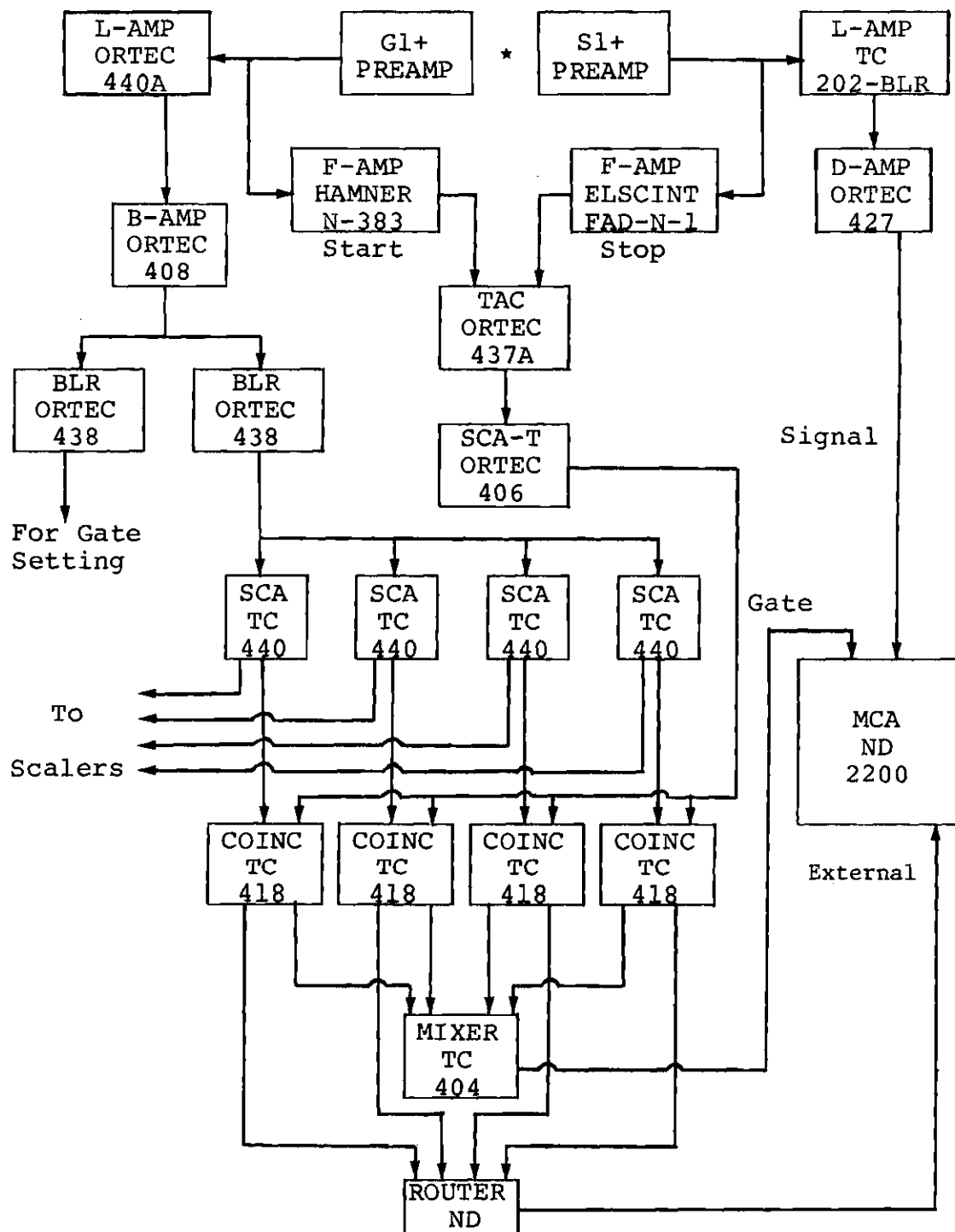


Figure 7. Fast-Slow Single Parameter Coincidence System
(see Sect. 4.3.1)

of the TAC from the "signal" side, as shown in Fig. 7. The fast amplifiers are designed to give an output suitable for fast timing (i.e., a negative spike). This output is always very accurately correlated in time to the input signal. By connecting the outputs of these fast amplifiers to a TAC an output from the TAC is obtained which is proportional to the time between the pulses arriving at the start input and the pulse arriving at the stop input. By selecting the range of pulses which correspond to $K_{\alpha_{1,2}}$ x-ray-L x-ray cascade events (prompt events), many random coincidence events can be excluded. The prompt events are selected using a single channel analyzer (SCA)*. The output from the SCA-T was connected to the four coincidence units (COINC).

In the slow branch, pulses from the gate detector were processed through a linear amplifier (L-AMP), biased amplifier (B-AMP), and baseline restorer (BLR). The linear amplifier served to shape the pulse, while the B-AMP biased off the region below the K x rays and amplified the K x-ray region. The BLR served as an impedance matching unit. The BLR was connected to the four SCA units which have windows set to accept the respective energy regions. Typical gate settings are designated by the shaded areas in Figs. 2, 4, and 5. Pulses from the SCA units along with pulses from the SCA-T were introduced into the mixer (operating as a

*This particular SCA will be designated as SCA-T since it is used in the timing branch of the system.

multiplexer). A signal from the mixer and router, along with a properly delayed signal from the L x-ray detector, entered the MCA and the latter signal was recorded in the appropriate channel and quadrant of the MCA. The spectrum recorded in each quadrant of the MCA corresponds to the L x-ray spectrum in coincidence with its corresponding gate set by the SCA.

4.3.2 Dual-Parameter Coincidence System

In the fast branch of the coincidence system (see Fig. 8), the signal from the preamplifier of the Ge(HP) detector (G1) formed the input to a fast amplifier and discriminator (FAD) which was connected to the start input of the TAC. Owing to the complex nature of the pulsed-optical preamplifier output, the preamplifier output of detector S2 was connected to a fast amplifier circuit in the L-AMP. The output of this fast amplifier was connected to an integral discriminator (ID) which was connected to the stop input of the TAC. The prompt peak from the output of the TAC was selected by a SCA whose output was connected to a gate and delay generator (GDG). The delay of the GDG unit was adjusted so that coincident signals from the two L-AMP amplifiers would be processed.

The two fast branches of the dual-parameter system were identical. The output from the preamplifiers was connected to the ADC units through an L-AMP.

In this system the output of the ADC units was stored

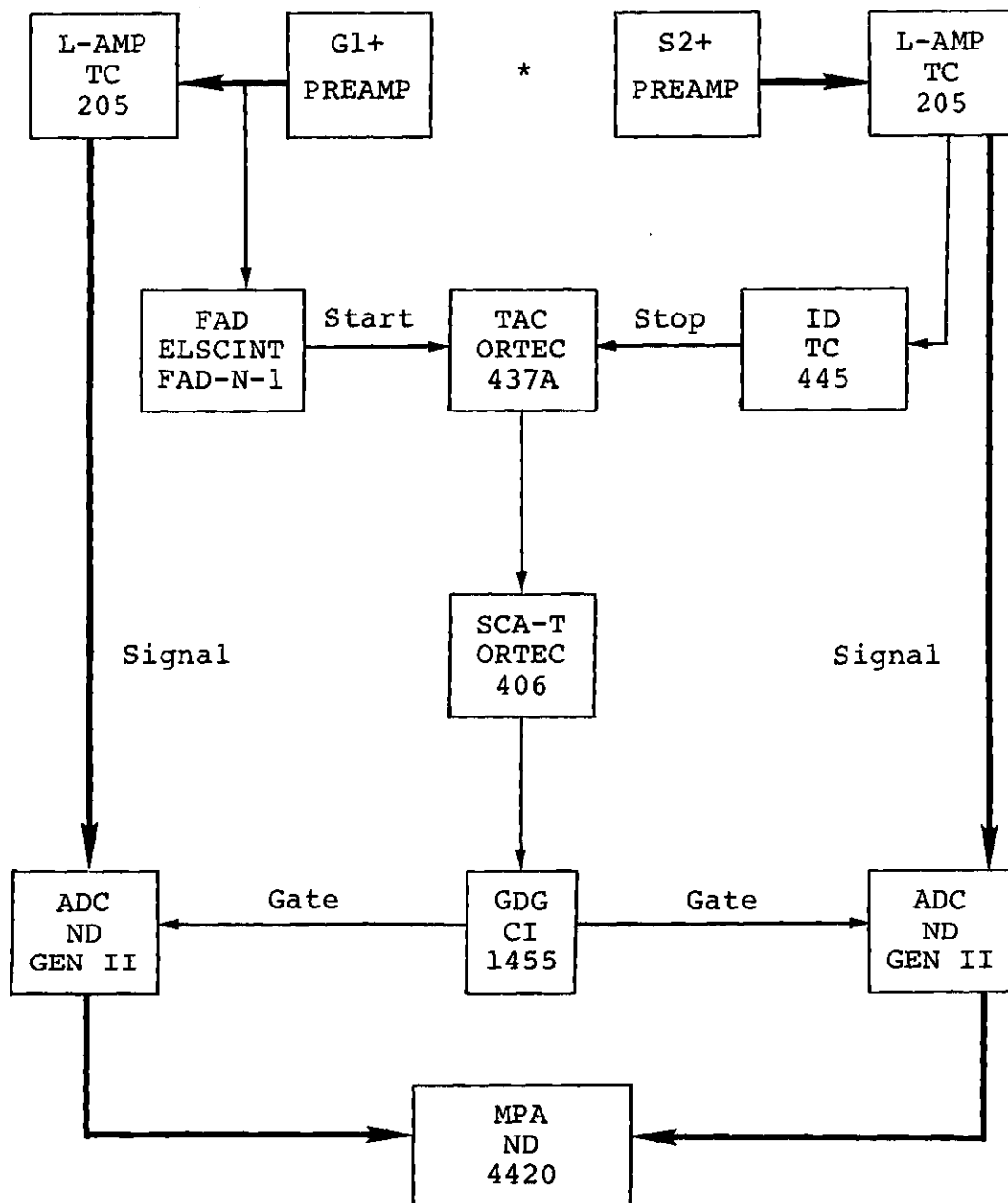


Figure 8. Fast-Slow Dual Parameter Coincidence System
(see Sect. 4.3.2)

in "list" mode in the memory of the ND-4420 MPA and later stored on magnetic tape. In the "list" mode the addresses ("channel numbers") corresponding to the events were stored sequentially in the buffer memory. At a later time the "list" data were sorted into separate spectra corresponding to the applied gates. Such sorting of data was accomplished with a standard program provided by Nuclear Data.

CHAPTER V

DATA EVALUATION AND RESULTS

5.1 Mean L-Shell Fluorescence Yields

Mean L-shell fluorescence yields ($\bar{\omega}_L$) were measured by observing K and L x-ray singles spectra from the decay of Cd^{109} , Pm^{145} , and Gd^{153} using detector S1. The basis of this method is given in Sect. 3.2.1. Eq. (55) was then used to relate the measured ratio I_L/I_K to $\bar{\omega}_L$.

Singles spectra were taken for Cd^{109} , Pm^{145} , and Gd^{153} to determine the x-ray intensity ratio I_L/I_K . Counting rates for the components in the K and L x-ray lines were computed and corrected by their respective detection efficiencies after subtracting the continuum beneath the peaks. The continuum was subtracted in an identical manner as in the determination of the efficiency, in order to minimize systematic errors in the estimation of the true counting rates.

Owing to the large coefficient for absorption of the 3 keV L x rays in the case of Cd^{109} , the source thickness was evaluated by observing degradation of the conversion electron energy. For this purpose the electron spectrum was observed by a windowless Si(Li) detector (130) which was calibrated by γ rays and K x rays of well known energies. After corrections for the energy shift of the electron peaks

due to the gold contact and dead silicon layers and the 1 keV negative bias on the front face of the detector, the remaining shift of 1.44 keV was attributed to a mean source thickness of approximately $320 \mu\text{g}/\text{cm}^2$. Assuming this to be mostly due to Cd^* and using x-ray cross sections from Storm and Israel (131), a correction factor for self-absorption of the L x rays of 1.16 was derived for the ratio I_L/I_K .

Corrections for absorption of L x rays in the other sources were negligible, since high specific activity solutions were used.

The present results for $Z = 47, 60, \text{ and } 63$ are as follows: $\omega_L = 0.0425 \pm 0.0064, 0.131 \pm 0.017, \text{ and } 0.142 \pm 0.023$, respectively.

5.2 L_2^- and L_3^- -Subshell Yields at $Z = 86, 88, 92, \text{ and } 94$

Sect. 3.2.2.1 and 3.3 give a description of the general method used to reduce the data. The following sections are devoted to a brief description of the individual circumstances associated with evaluating the data for each of the atomic numbers $Z = 86, 88, 92, \text{ and } 94$.

Low counting rates (e.g. less than 2000 counts/sec) were used, so that corrections due to deadtime, pulse pile-up, and summing effects were negligible. In addition, the electronic timing and the counting rates were adjusted to

*The Cd^{109} activity was produced by the reaction $\text{Cd}^{108} (n, \gamma) \text{Cd}^{109}$. This activity was electroplated onto a thin backing.

give a coincidence efficiency of unity as checked by means of self-gated coincidence experiments using one detector and its timing and counting outputs in coincidence. Corrections for spurious events in the gate and in the coincidence spectrum, and for angular correlation effects were discussed in Sect. 3.3. Efficiency corrections were discussed in Sect. 4.2.

Tables of typical composition of the K_{α_1} and K_{α_2} x-ray gates* and of typical composition of the L_{α} peak in the K_{α_1} and K_{α_2} x-ray coincidence spectra are given in Appendix I, together with evaluation of results for a typical run.

Final values of f_{23} , v_2 , ω_2 , and ω_3 are given in Table 3. The error limits assigned to v_2 , ω_2 , and ω_3 are 2σ statistical uncertainty (95 percent confidence limit) plus linear addition of the uncertainty in the detection efficiency (4 percent). The error limits assigned to f_{23} are 2σ statistical uncertainty plus linear addition of the uncertainty in the corrections for the presence of the K_{α_1} pulses in the K_{α_2} gate. The 2σ statistical uncertainty (i.e., that uncertainty due to counting statistics) contributed an uncertainty of less than 3 percent (of the magnitude of the results).

*By "gate composition" is meant the analysis of all events falling into the gate window arising from true events, chance coincidences, nuclear cascade coincidences, and spurious counts arising from tailing of higher energy events into the gate window.

Table 3. Present Experimental Values of ν_2 , ω_2 , ω_3 , and f_{23} for $Z = 80, 81, 82, 86, 88, 92$, and 94

ATOMIC NUMBER	Quantity*			
	f_{23}	ν_2	ω_2	ω_3
80	0.123 ± 0.012			
81	0.109 ± 0.011			
82	0.105 ± 0.011			
86	0.105 ± 0.011	0.498 ± 0.028	0.459 ± 0.025	0.384 ± 0.020
88	0.053 ± 0.052	0.516 ± 0.036	0.493 ± 0.030	0.408 ± 0.027
92	$0.147 \pm 0.010^{**}$ $0.146 \pm 0.018^{***}$	$0.630 \pm 0.036^{**}$	$0.560 \pm 0.033^{**}$	0.481 ± 0.029
94	0.226 ± 0.016	0.627 ± 0.036	0.513 ± 0.022	0.509 ± 0.029

* Error limits are 2σ (95 percent confidence level) plus linear addition of uncertainty in detection efficiency.

** Values obtained from the decay of Np^{235} .

*** This value obtained from the decay of Pa^{233} .

5.2.1 Radon L-Subshell Yields From Ra²²³ Decay

The subshell yield measurements for Rn were straight forward. Corrections for the presence of the K_{α_1} x-ray pulses in the K_{α_2} x-ray gate (4.3 percent) were derived by using the 82 keV γ ray of Ba¹³³ and the 74.6 keV γ ray of Am²⁴³ as models for the shape of the K_{α_1} x-ray peak.* Typical gate settings for this measurement have been presented in Fig. 5. Four separate coincidence runs of approximately two days duration were made.

5.2.2 Radium L-Subshell Yields From Th²²⁷ Decay

Due to the complexity of the decay scheme of Th²²⁷ (132), an unusually large correction for nuclear cascading must be applied to the L_{α} peak in coincidence with the K_{α_2} x rays. This correction (approximately 87 percent, see Appendix I) gives rise to large error limits on the measured f_{23} value. Corrections associated with the determination of ω_2 and ω_3 are relatively smaller; therefore, the error limits for these two quantities are correspondingly smaller.

Corrections for the presence of the K_{α_1} x-ray pulses in the K_{α_2} x-ray gate (4 percent) were derived by using γ rays from the decay of Ba¹³³ and of Am²⁴³ (see Sect. 5.2.1) as models for the shape of the K_{α_1} x-ray peak.

* The magnitude of the K_{α_1} tail which falls into the K_{α_2} gate was determined by normalizing a monoenergetic γ -ray line shape of similar energy to the K_{α_1} peak and subtracting that portion of its tail that is encompassed by the K_{α_2} gate.

Analysis of the K_{β_1}' x-ray gate count rate is complicated by a contribution of approximately 5 percent from the 100 keV γ ray emitted following the α decay of Th^{227} (132). On the basis of theoretical conversion coefficients (88) for the 29.9 keV transition that follows the 100 keV transition in the Th^{227} decay scheme (132), it was deduced that the number of L x-ray coincidences per 100 keV γ -ray gate pulse is almost the same as the number observed per K_{β_1}' -gate pulse, and no correction was therefore necessary.

Four separate coincidence runs of two to four days duration were made.

5.2.3 Uranium L-Subshell Yields From Np^{235} Decay

Nuclear cascading is absent in Np^{235} decay*, but a gate set on K_{β_1}' x rays enabled the correction for chance coincidences to be determined at the same time as the true coincidences between the K_{α_1} and K_{α_2} x-ray gate pulses and the L x ray pulses. The large L/K capture ratio ($P_L/P_K = 32.2$, Ref. 133) in Np^{235} decay (134, 135) leads to a large number of L x rays that are not preceded by a K x ray. These L x rays cannot contribute to the true coincidences, but only increase the chance/true ratio. The coincidence resolving time (2τ) was therefore chosen carefully, in order to minimize the chance coincidence counting rate and at the same time maintain a coincidence efficiency close to unity.

* This was confirmed with the help of a separate chance coincidence run.

Examination of the time distribution between K x-ray events in the Ge(HP) detector and the L x-ray events in the Si(Li) detector revealed a prompt coincidence peak approximately 130 nsec wide (full width at tenth maximum), and in the coincidence experiment a time window of 160 nsec was set to completely envelope the peak. Two further runs were taken with $2\tau = 300$ nsec, in order to check the coincidence efficiency. After correction for chance coincidences [approximately 14 percent correction to the L_{α} peak in coincidence with K_{α_2} x rays for $2\tau = 300$ nsec (worst case)], the coincidence counting rates for all three runs (of approximately three day duration) were in good agreement.

The contribution of K_{α_1} pulses to the K_{α_2} window was found to be 3.3 percent (of the K_{α_2} gate) by using the low-energy tail of the K_{α_2} peak as a guide to shape of the K_{α_1} tail. This result agreed well with a value obtained by taking the shape of the 122 keV γ ray in Co^{57} decay as a model for the shape of the K x-ray peak.

5.2.4 Measurement of f_{23} for Uranium From Pa^{233} Decay

A sizable correction for nuclear cascading (approximately 68 percent, see Appendix I) was applied to the $K_{\alpha_{1,2}}$ x-ray- L_{α} x-ray coincidence data due to the complex decay scheme (126, 136). Since the cascade correction is applied for each run by the K_{β} subtraction method (116) simultaneously with the $K_{\alpha_{1,2}}$ x-ray- L_{α} x-ray coincidence measurements (see Sect. 3.3.2), and since the source was strong and allowed

collection of good statistics, f_{23} could be measured to approximately 12 percent accuracy. In addition, six coincidence runs of one to two day duration were made.

The K_{α_1} x-ray pulses which "tail" into the K_{α_2} x-ray gate were found to be 2.6 percent of the K_{α_2} x-ray gate. This was determined by using the low-energy tail of the 88 keV γ ray of Cd^{109} and of the 122 keV γ ray of Co^{57} as models for the shape of the K_{α_1} x-ray peak.

5.2.5 Plutonium L-Subshell Yields From Np^{239} Decay

Analysis of the K_{α_1} and K_{α_2} x-ray gates was complicated by the presence of "tailing" from the 106 keV γ rays emitted following Np^{239} decay (see Fig. 2). In order to correct for this, two extra runs (in addition to five standard coincidence runs of two to four day duration) were made with a separate gate set on the 106 keV γ ray. The contribution of 106 keV γ -ray pulses to the K_{α_2} (4.1 percent) and K_{α_1} (6.1 percent) x-ray gates was determined by using the 122 keV γ ray from Co^{57} to give a model for the shape of a single line. Similarly, the K_{α_1} contribution to the K_{α_2} x-ray gate was determined to be 3.6 percent. While the contribution from the weak 98.5 keV γ ray (from Am^{243} decay) to the K_{α_2} x-ray gate was negligible, the K_{β_1}' x-ray gate contained a contribution of approximately 4 percent from the 117.8 keV γ ray. According to the Am^{243} decay scheme (137, 138) however, there can be only a negligible number of Np L x rays in coincidence with the 117.8 keV γ ray, and this

contribution to the K_{β_1}' x-ray gate is taken into account on the basis of chance coincidences only. Two additional runs were made with this gate set on the K_{β_2}' x-ray group, and the results obtained were consistent with those from the main runs.

5.3 The Measurements of f_{23} at $Z = 80, 81, \text{ and } 82$

With the-Dual Parameter System

The radioactive nuclides Au^{198} , Hg^{203} , and Bi^{207} were used to study the Coster-Kronig transition probability f_{23} at $Z = 80, 81, \text{ and } 82$, respectively. In order to reduce deadtime due to β^- -ray-x-ray coincidences, a thin aluminum beta absorber was inserted between the Ge(HP) detector and the source and a thin beryllium beta absorber was inserted between the source and the Si(Li) detector for the measurements of the β^- emitters, Au^{198} and Hg^{203} .

The contribution of K_{α_1} pulses to the K_{α_2} gate was determined by using the 59.5 keV γ ray from the decay of Am^{241} and the 88 keV γ ray from the decay of Cd^{109} as models for the shape of the K_{α_1} x-ray peak. The contributions of the K_{α_1} events to the K_{α_2} peak were found to be 3.8, 4.7, and 4.9 percent of the K_{α_1} peak at $Z = 80, 81, \text{ and } 82$, respectively.

The data were collected with the ND-4420 dual parameter system and could be analyzed by using the L_{α} -gating or the $K_{\alpha_{1,2}}$ -gating technique (see Sects. 3.2.2.1 and 3.3).

The Bi²⁰⁷ data were analyzed using both techniques. The results and corrections of both techniques are equivalent. The Au¹⁹⁸ and Hg²⁰³ data were analyzed by the K_{α_{1,2}}-gating technique. Three, two, and six separate coincidence runs (of two to three days duration) were made for Au¹⁹⁸, Hg²⁰³, and Bi²⁰⁷, respectively.

Tables of typical gate composition and typical composition of the L_α coincidence peak are given in Appendix I. These tables are given in terms of L_{α_{1,2}} gating.

Values of $f_{23} = 0.123 \pm 0.012$, 0.109 ± 0.011 , and 0.105 ± 0.11 at $Z = 80, 81, \text{ and } 82$ were determined from K_{α_{1,2}}-L x-ray coincidences, observed using Au¹⁹⁸, Hg²⁰³, and Bi²⁰⁷ activities, respectively. The assigned error limits correspond to 95 percent confidence (2σ error limits). These results are listed in Table 3.

CHAPTER VI

DISCUSSION AND CONCLUSIONS

6.1 Discussion and Conclusions of Mean L-ShellFluorescence Yields

The mean L-shell fluorescence yield ($\bar{\omega}_L$) is given by the relation (eq. 9, Sect. 1.4):

$$\bar{\omega}_L = N_1 v_1 + N_2 v_2 + N_3 v_3$$

where $N_1 + N_2 + N_3 = 1$ and $N_1:N_2:N_3$ is the distribution of primary L-subshell vacancies before Coster-Kronig transitions alter them. By combining values of v_1 , v_2 , and v_3^* from the theoretical calculations of Crasemann and coworkers (20, 21) or of McGuire (17) with the $N_1:N_2:N_3$ vacancy distribution evaluated for example from experimental or theoretical conversion coefficients and/or orbital electron capture rates [see Ref. (100) for details], it is possible to obtain a theoretically-based prediction of $\bar{\omega}_L$ which then may be compared with the experimental value for a given Z as a test of the consistency of the predicted value of $\bar{\omega}_L$. The

* The quantity v_i represents the probability of emission of an L x-ray per L_i -subshell vacancy (see Sect. 1.4).

predicted values* of $\bar{\omega}_L$ for $Z = 47, 60,$ and 63 are given in Table 4, together with present and previous experimental values and $N_1:N_2:N_3$ ratios.

Since the primary L-vacancy distribution $N_1:N_2:N_3$ is known to better than 10 percent for these cases, the predicted value of $\bar{\omega}_L$ should be good to better than 10 percent, and a comparison with experiment then serves as a test of the theoretical calculations of the mean L-subshell fluorescence yields $v_1, v_2,$ and v_3 .

The calculated values based on the theory of Crasemann and coworkers (20, 21) agree with present results at $Z = 47, 60,$ and $63,$ while calculations based on the theory of McGuire (17) agree at $Z = 60$ and $63,$ but give a value considerably higher at $Z = 47.$

The theory of Crasemann and coworkers (20, 21) predicts that the values of v_i in the region of $40 \leq Z \leq 70$ are equal within plus or minus 15 percent. Even for the radically different vacancy distributions obtained in K_α x-ray-L x-ray coincidence experiments, differences in the v_i values as large as 30 percent would not give rise to significantly different values of $\bar{\omega}_L$. With this consideration, it becomes meaningful to compare present results with previous experiments (Table 4). Disagreement between

* In Table 4, the theoretical values of $\bar{\omega}_L$ are uncorrected for the effect of double vacancies, but this correction is in any case less than 4 percent [see Ref.(100)].

Table 4. Comparison of the $\bar{\omega}_L$ Results with Theory and Previous Experiment

Z	Experimental $\bar{\omega}_L$	Theoretical $\bar{\omega}_L$		Primary L-Shell Vacancy Distribution $N_1 : N_2 : N_3$	Reference
		Crasemann (20,21)	McGuire (17)		
47	0.0425±0.0064	0.0461	0.0615	0.160:0.335:0.505	Present Work, 100
	0.049 ^a			0.160:0.335:0.505	31
	0.029 ±0.003 ^b			0.160:0.335:0.505	139
	0.100			0.17 :0.33 :0.50	23
	0.047 ±0.002			0.17 :0.33 :0.50	140
	0.044 ±0.003			0.00 :0.35 :0.65	32
	0.054 ±0.007			0.00 :0.35 :0.65	29
	0.0659±0.0037			0.00 :0.35 :0.65	141
60	0.131 ±0.017	0.125	0.143	0.274:0.269:0.457	Present Work, 100
	0.170			0.17 :0.33 :0.50	23
	0.16 ±0.02			0.00 :0.35 :0.65	28
63	0.142 ±0.023	0.150	0.169	0.262:0.272:0.466	Present Work, 100
	0.145 ±0.013			0.30 :0.26 :0.44	108
	0.17 ^c				142
	0.18 ±0.02			0.00 :0.36 :0.64	28

(Continued)

Table 4. (Continued)

- a) Reevaluated using more recent values for ω_K , $P_{K'}$, $P_{L'}$, α_K , α_L , α_T , and n_{KL} (see Ref. 100).
- b) Calculated from Ref. 21 and equations given previously (Ref. 99).
- c) Due to the complexity of the 104 keV γ ray gate set on a NaI(Tl) detector (Ref. 142) values of N_1 : N_2 : N_3 are very difficult to calculate. For this reason there may be large uncertainties associated with this value of $\bar{\omega}_L$.

the older results of Bertolini et al. (139) and Lay (23) with the present results may be due to uncertainties in detector efficiencies or source self-absorption in their work. The disagreement between the results of Jopson et al. (28, 29) and Bailey and Swedlund (141) with the present results is possibly due to uncertainties in the self-absorption of L x rays in their targets. Other experimental results (31, 32, 108, 140) agree with the present results within the stated error limits.

The following conclusions can be drawn concerning mean L-shell fluorescence yields, i.e., both $\bar{\omega}_L$ and ω_{KL} . Certain older results should be discarded due to uncertainties inherent in their experimental method. Ref. (100) gives a table of the latest $\bar{\omega}_L$ measurements including those in the present work. At $Z = 47$, the present experiment shows that the theoretical predictions of Crasemann and coworkers (20, 21) were correct, while those of McGuire (17) were high. At $Z = 60$ and 63 , the present experimental uncertainty (plus or minus 13 and 16 percent, respectively) is too large to permit distinction between the theoretical predictions.

6.2 Comparison of Present Values of ω_2 and ω_3 with

Theory and with Previous Experiments

Determination of the quantities ω_2 and ω_3 is dependent upon detector efficiency. Accurate determination of

detection efficiencies has been difficult in the past, due to lack of x-ray standards, insufficient knowledge of photon emission rates, and limited information on detector parameters such as deadlayers. Recent studies of detection efficiencies (128, 129, 115) has enabled one to measure detector efficiency in the region of 10 to 100 keV more accurately (approximately 4 percent). The lack of agreement among some of the early measurements of L_2 - and L_3 -subshell fluorescence yields (90, 91, 92) and the present work may be due to problems associated with detector efficiencies (see Table 5). Recent measurements of Campbell et al. (106) by means of Ce_L^- -L x-ray coincidence techniques are in agreement with the present work (see Table 5).

The discontinuity in the value of ω_2 (see Fig. 9) is due to the discontinuity in f_{23} (i.e., $\omega_2 + a_2 + f_{23} = 1$, see Sect. 6.3 for a discussion of the discontinuity in f_{23}). The points designated by "+" at $Z = 93$ and designated by "X" at $Z = 94$ are calculated using the hydrogenic model (20) and the independent-particle model (IPM) with a Green-Sellin-Zachor (GSZ) potential (22), respectively.

The measured values of ω_2 agree with the SCF Calculations of McGuire (17, 18). The hydrogenic calculations of Chen, Crasemann, and Kostroun (20) are low compared with with the present results, but fall within the experimental error limits at $Z = 86$ and 88 . The theoretical predictions of Chen and Crasemann (22) using the IPM with a GSZ potential

Table 5. Summary of Experimental Values and Theoretical Predictions of ω_2 and ω_3

Z	Element	ω_2		ω_3		Reference
		Experiment*	Theory	Experiment*	Theory	
83	Bi		0.417		0.389	17
85	At		0.422 0.410		0.380	20 22
86	Rn	0.459 ± 0.025		0.384 ± 0.020		Present Work, 73
88	Ra	0.493 ± 0.030 0.415 ± 0.027 0.498 ± 0.027		0.408 ± 0.027 0.438 ± 0.022		Present Work, 73 92 106
90	Th	0.44 ± 0.03	0.529		0.461	17 91
92	U	0.560 ± 0.033 0.529 ± 0.35*** 0.423 ± 0.023	0.488**	0.481 ± 0.029	0.460	18 Present Work, 133 38 92
93	Np		0.460		0.472	20
94	Pu	0.513 ± 0.022 0.523 ± 0.023*** 0.42 ± 0.02 0.485 ± 0.026	0.517** 0.427	0.509 ± 0.029 0.484 ± 0.017	0.502	18 22 Present Work, 73 38 90 106

Table 5. (Continued)

Z	Element	ω_2		ω_3		Reference
		Experiment*	Theory	Experiment*	Theory	
96	Cm		0.544		0.528	18
		0.552 \pm 0.032		0.515 \pm 0.034		38
		0.55 \pm 0.02		0.63 \pm 0.02		94
		0.59 \pm 0.04		0.68 \pm 0.05		93
98	Cf		0.503		0.515	18

* The quoted errors are taken from the original publication.

** This value was calculated assuming that $L_2-L_3M_{4,5}$ transitions are possible. A value of 0.544 and 0.579 is calculated at $Z = 92$, and 94, respectively, assuming that $L_2-L_3M_{4,5}$ transitions are not possible.

*** This value is a revision of a value given in Ref. 89.

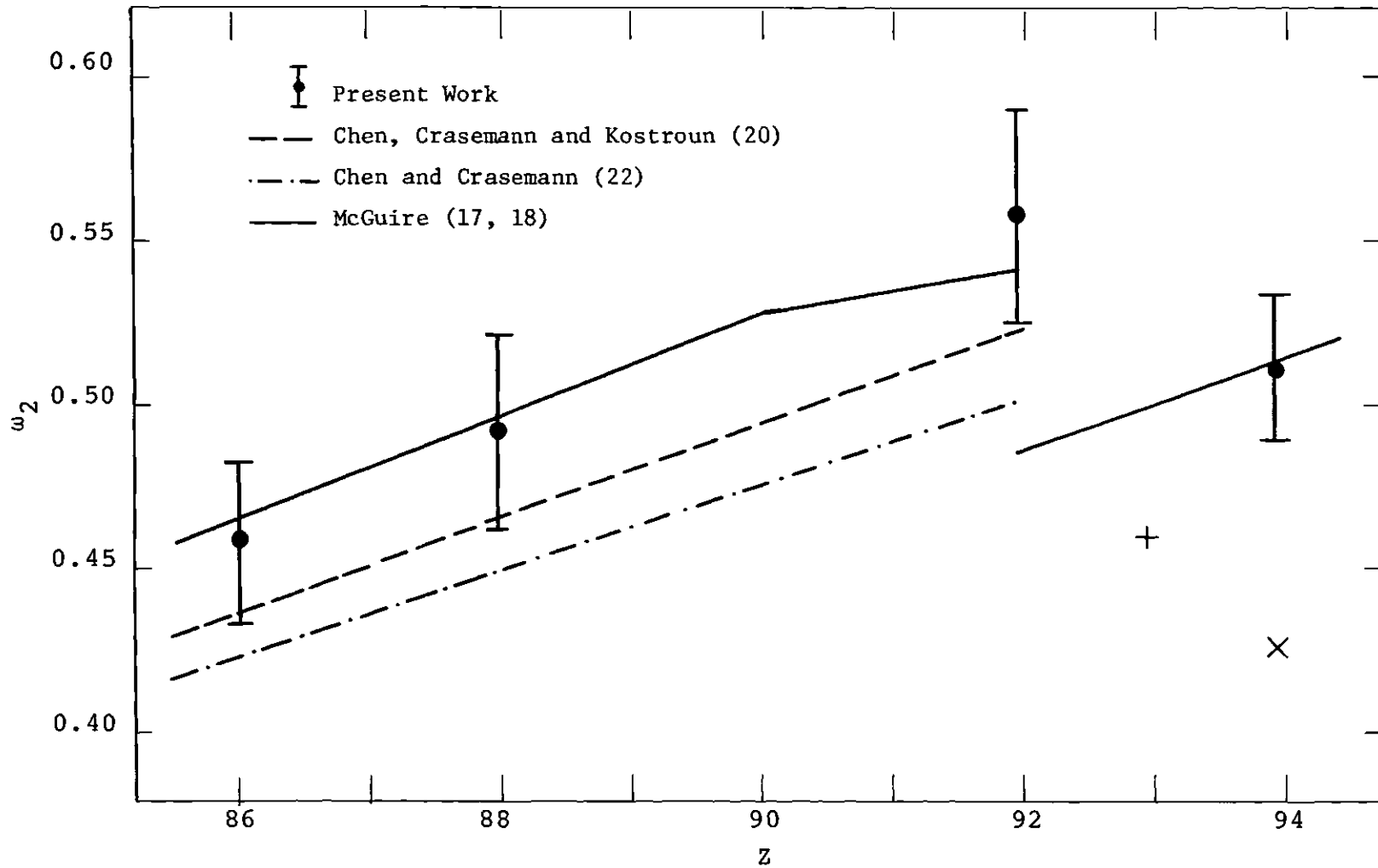


Figure 9. Plot of ω_2 vs Z . (Theoretical points at $Z = 93$ and 94 are calculated using the Hydrogenic model (20) and the IPM model (22), respectively, and are plotted as "+" and "X", respectively.)

are systematically lower than the present experimental values. The measured values of ω_3 (see Fig. 10) at $Z = 86$ and 88 tend to agree better with the hydrogenic calculations of Chen, Crasemann, and Kostroun (20) than with McGuire (17) while at $Z = 94$ the experiment agrees with the SCF calculations of McGuire (18).

In summary, although there is overall good agreement between experiment and McGuire's theory (17, 18) for ω_2 , the available experimental accuracy (limited mainly by uncertainties in detector efficiency) is not sufficient to distinguish between the theoretical predictions due to McGuire (17, 18) and those due to Chen, Crasemann, and Kostroun (20). The experimental results rule out the IPM calculation with the GSZ potential by Chen and Crasemann (22).

6.3 Comparison of f_{23} with Theory

Owing to the lack of agreement among all reported measurements of f_{23} (see Table 6), a critical evaluation of the past experimental work is necessary before a meaningful comparison with theory can be made. In the present work selected "most reliable" experimental values of f_{23} are derived from a consideration of all published results. Table 7 lists these selected "most reliable" f_{23} values. The selected results are derived only from those measurements which carefully measure and clearly describe all corrections. The magnitude of certain corrections is quite large, (see

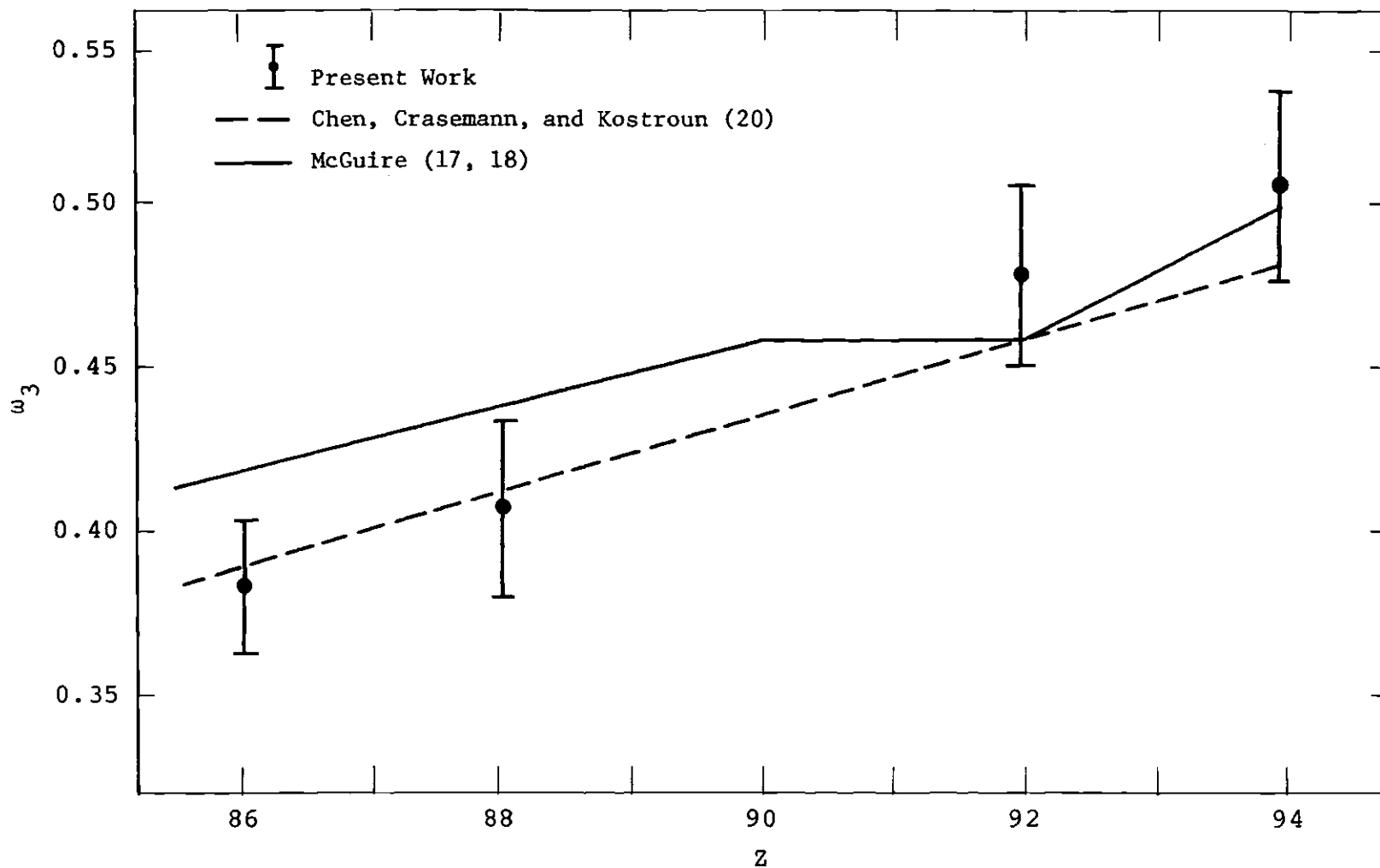


Figure 10. Plot of ω_3 vs Z. (The work of Chen, Crasemann, and Kostroun (20) is extrapolated from Z = 93 to Z = 94.)

Table 6. Measured $L_2 - L_3$ Coster-Kronig Yields

Z	Element	f_{23}^*	Reference
57	La	0.21 ± 0.02	143
63	Eu	0.172 ± 0.015 0.127 ± 0.013	144,145 41,146
64	Gd	0.223 ± 0.011	147
65	Tb	0.066 ± 0.014 0.124 ± 0.012	148,116 41,146
67	Ho	0.205 ± 0.034	149,15
68	Er	0.225 ± 0.025	149,15
70	Yb	0.142 ± 0.009 0.130 ± 0.010	148,150 151
73	Ta	0.20 ± 0.04 0.150 ± 0.007 0.128 ± 0.013	33 148,110 41,146
76	Os	0.106 ± 0.023	152
78	Pt	0.126 ± 0.021	152
80	Hg	0.123 ± 0.012 0.22 ± 0.04 0.08 ± 0.02 0.188 ± 0.010 0.131 ± 0.013 0.125 ± 0.012	Present Work 153 33 148,154 41,146 41,146
81	Tl	0.109 ± 0.011 0.25 ± 0.13 0.169 ± 0.010 0.113 ± 0.010 0.130 ± 0.006	Present Work 155 156 41,146 157
82	Pb	0.105 ± 0.011 0.164 ± 0.016 0.156 ± 0.010	Present Work 37 158

Table 6. (Continued)

Z	Element	f_{23}^*	Reference
83	Bi	0.06 + 0.14 - 0.06	109
86	Rn	0.105 ± 0.011	Present Work, 73
88	Ra	0.053 ± 0.052 0.01 ± 0.07 0.102 ± 0.006	Present Work, 73 92 106
90	Th	0.13 ± 0.10	91
92	U	0.147 ± 0.010 0.146 ± 0.018 0.43 ± 0.06 0.37 ± 0.07 0.07 ± 0.05 0.23 ± 0.12 0.14 + 0.11** - 0.06	Present Work, 133 Present Work 89 89 92 38 112, 159
93	Np	0.02 + 0.05 - 0.02	160
94	Pu	0.226 ± 0.016 0.22 ± 0.08 0.42 ± 0.08 0.21 ± 0.08 0.24 ± 0.08 0.229 ± 0.004 0.233 ± 0.015 0.24 + 0.19** - 0.09	Present Work, 73 26 89 90 38 106 144, 145 112, 159
96	Cm	0.188 ± 0.010 0.226 ± 0.017	73, 38 144, 145

* The quoted errors are taken from the original publication.

** These values are calculated assuming the $L_2 - L_3M_{4,5}$ transitions are possible. Values of $f_{23} = 0.41 + 0.59$
- 0.16 and > 0.44 are calculated for $Z = 92$ and 94 , respectively, if only the $L_2 - L_3M_5$ transition is possible (112, 159).

Table 7. Selected "Most Reliable" Experimental $L_2 - L_3$ Coster-Kronig Yields*

Z	Parent	Daughter	f_{23}	Method	Reference
63	Gd ¹⁵³	Eu ¹⁵³	0.127 ± 0.013	L_α gated K_α x-ray coinc.	41,146
65	Dy ¹⁵⁹	Tb ¹⁵⁹	0.124 ± 0.012	L_α gated K_α x-ray coinc.	41,146
70	Tm ^{171,170}	Tm ^{171,170}	0.142 ± 0.009	$K_{\alpha_1}, K_{\alpha_2}$ gated L_α x-ray coinc.	148,150
	Tm ¹⁷¹	Yb ¹⁷¹	0.130 ± 0.010	$L_2, L_3\text{Ce}^-$ gated L_α x-ray coinc.	151
73	W ¹⁸¹	Ta ¹⁸¹	0.128 ± 0.013	L_α gated K_α x-ray coinc.	41,146
76	Ir ¹⁹²	Os ¹⁹²	0.106 ± 0.023	$K_{\alpha_1}, K_{\alpha_2}$ gated L_α x-ray coinc.	152
78	Ir ¹⁹²	Pt ¹⁹²	0.126 ± 0.021	$K_{\alpha_1}, K_{\alpha_2}$ gated L_α x-ray coinc.	152
80	Au ¹⁹⁸	Hg ¹⁹⁸	0.123 ± 0.012	$K_{\alpha_1}, K_{\alpha_2}$ gated L_α x-ray coinc.	Present Work
	Au ¹⁹⁸	Hg ¹⁹⁸	0.131 ± 0.013	L_α gated K_α x-ray coinc.	41,146
	Tl ²⁰⁴	Hg ²⁰⁴	0.125 ± 0.012	L_α gated K_α x-ray coinc.	41,146
81	Hg ²⁰⁵	Tl ²⁰³	0.109 ± 0.011	$K_{\alpha_1}, K_{\alpha_2}$ gated L_α x-ray coinc.	Present Work

Table 7. (Continued)

Z	Parent	Daughter	f_{23}	Method	Reference
81	Hg ²⁰³	Tl ²⁰³	0.113 ± 0.010	L _α gated K _α x-ray coinc.	41,146
82	Bi ²⁰⁷	Pb ²⁰⁹	0.105 ± 0.011	K _{α₁} , K _{α₂} gated L _α x-ray coinc.	Present Work
86	Ra ²²³	Rn ²¹⁹	0.105 ± 0.011	K _{α₁} , K _{α₂} gated L _α x-ray coinc.	Present Work, 73
88	Th ²²⁸	Ra ²²⁴	0.102 ± 0.006	L ₂ , L ₃ Ce ⁻ gated L _α x-ray coinc.	106
92	Np ²³⁵	U ²³⁵	0.147 ± 0.010	K _{α₁} , K _{α₂} gated L _α x-ray coinc.	Present Work, 133
	Pa ²³³	U ²³³	0.146 ± 0.018	K _{α₁} , K _{α₂} gated L _α x-ray coinc.	Present Work
94	Np ²³⁹	Pu ²³⁹	0.226 ± 0.016	K _{α₁} , K _{α₂} gated L _α x-ray coinc.	Present Work, 73
	Cm ²⁴²	Pu ²³⁸	0.229 ± 0.004	L ₂ , L ₃ Ce ⁻ gated L _α x-ray coinc.	106
96	Cf ²⁴⁹	Cm ²⁴⁵	0.188 ± 0.010	K _{α₁} , K _{α₂} gated L _α x-ray coinc.	73,38

* Appendix II lists all values of f_{23} not contained in the selected "most reliable" values, along with reasons for their rejection. The quoted errors are taken from the original publication.

Appendix I for typical corrections) and thus these corrections have a large influence on the determination of the experimental values of f_{23} . Results which are derived using older, low-resolution instruments have been rejected as well as measurements which produced results by assuming other L-subshell quantities not measured in that work. Results which are measured by an α -particle-L x-ray coincidence technique have been described in Sect. 3.2.2.3. Measurements of f_{23} using the method of critical absorbers are rejected due to uncertainties in corrections for absorption and scattering that are present in this method. Appendix II lists all values of f_{23} not contained in the selected "most reliable" values, along with reasons for their rejection. Some results in Appendix II might be good measurements, but do not fit the stringent criteria.

Fig. 11 presents graphically the selected "most reliable" f_{23} values in the region $63 \leq Z \leq 88$ and compares them with theoretical predictions*. From Fig. 11 it is evident that the experimental values of f_{23} that were measured generally to plus or minus 10 percent or better, are in general agreement with the theoretical results in the region $63 \leq Z \leq 88$. This conclusion is in marked

*Values of f_{23} plotted at $Z = 70, 80, \text{ and } 81$ in Fig. 11 and $Z = 92$ and 94 in Fig. 12 correspond to an error weighted average of the selected "most reliable" experimental values. The error limits plotted at these Z values correspond to the error limits assigned to the most reliable measurement.

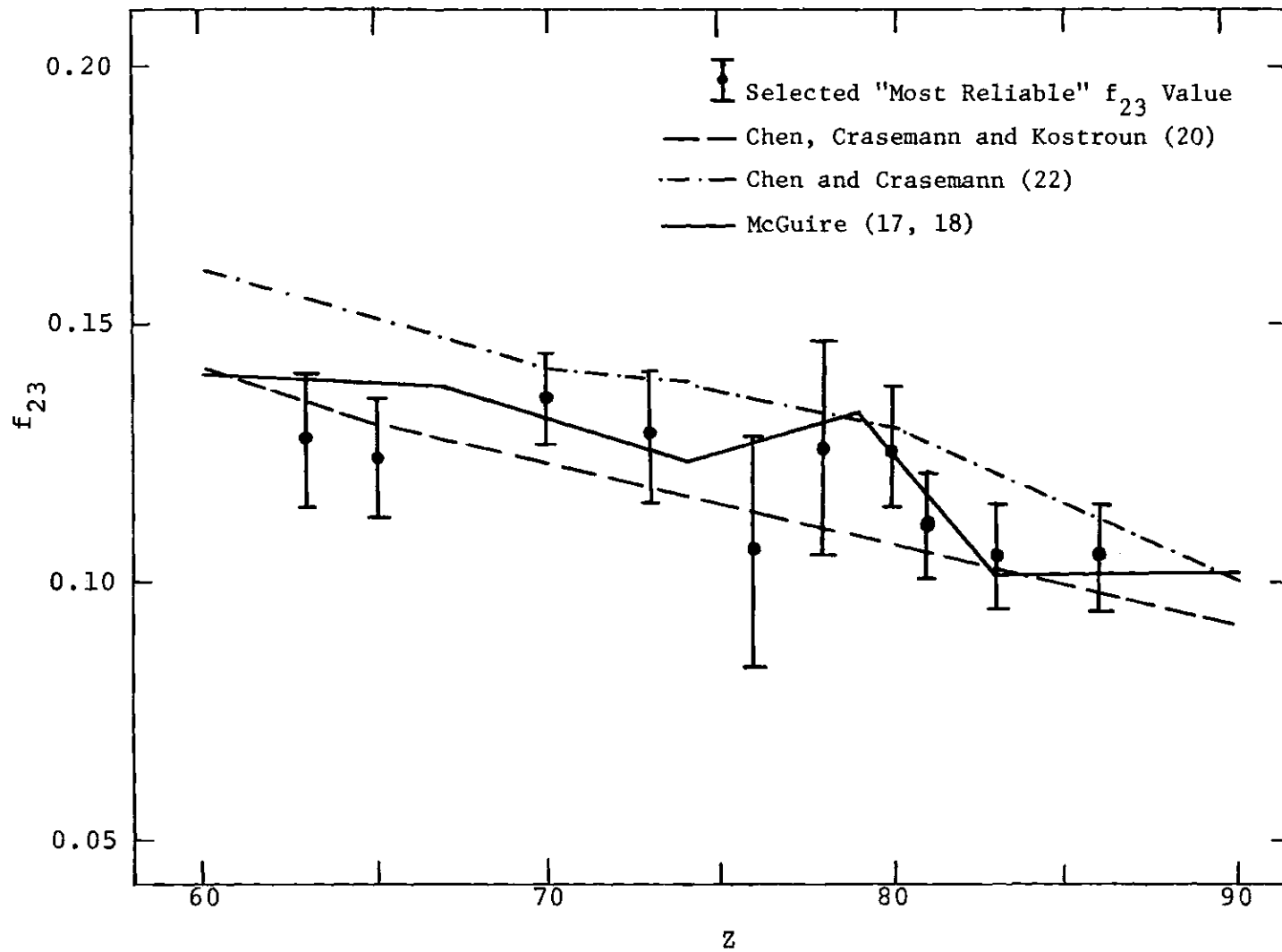


Figure 11. Plot of f_{23} vs Z in the Region $60 \leq Z \leq 90$.

disagreement with past interpretations (40, 147, 143, 158) which postulated disagreements of as much as 30 percent between theory and experiment. The different theoretical predictions in the region $60 \leq Z \leq 88$ lie within approximately plus or minus 5 percent of each other. Thus, the present experimental accuracy is insufficient to discriminate among the different theoretical methods in this region, although within the accuracy of the experimental and theoretical results, the agreement with the general trend of theory is good.

Fig. 12 plots f_{23} for the region $Z > 85$. It is evident that in the region $Z > 90$ the three theoretical predictions diverge (18, 20, 22), thus making experimental measurements of f_{23} in this region fruitful in terms of distinguishing among the different theoretical predictions. Each theory is discussed below and compared with the experimental results.

It can be seen from Fig. 12 that the theoretical prediction at $Z = 94$ by Chen and Crasemann (22) using the IPM with a GSZ potential is in violent disagreement with the experimental results. The uncertainties in this theoretical calculation of f_{23} employing the IPM at $Z = 94$ is dependent on the availability of a set of accurately determined parameters for $Z = 94$. It can be recalled from Sect. 2.3.2 that the GSZ potential is given by (eqs. 35 and 36, Sect. 3.2.2):

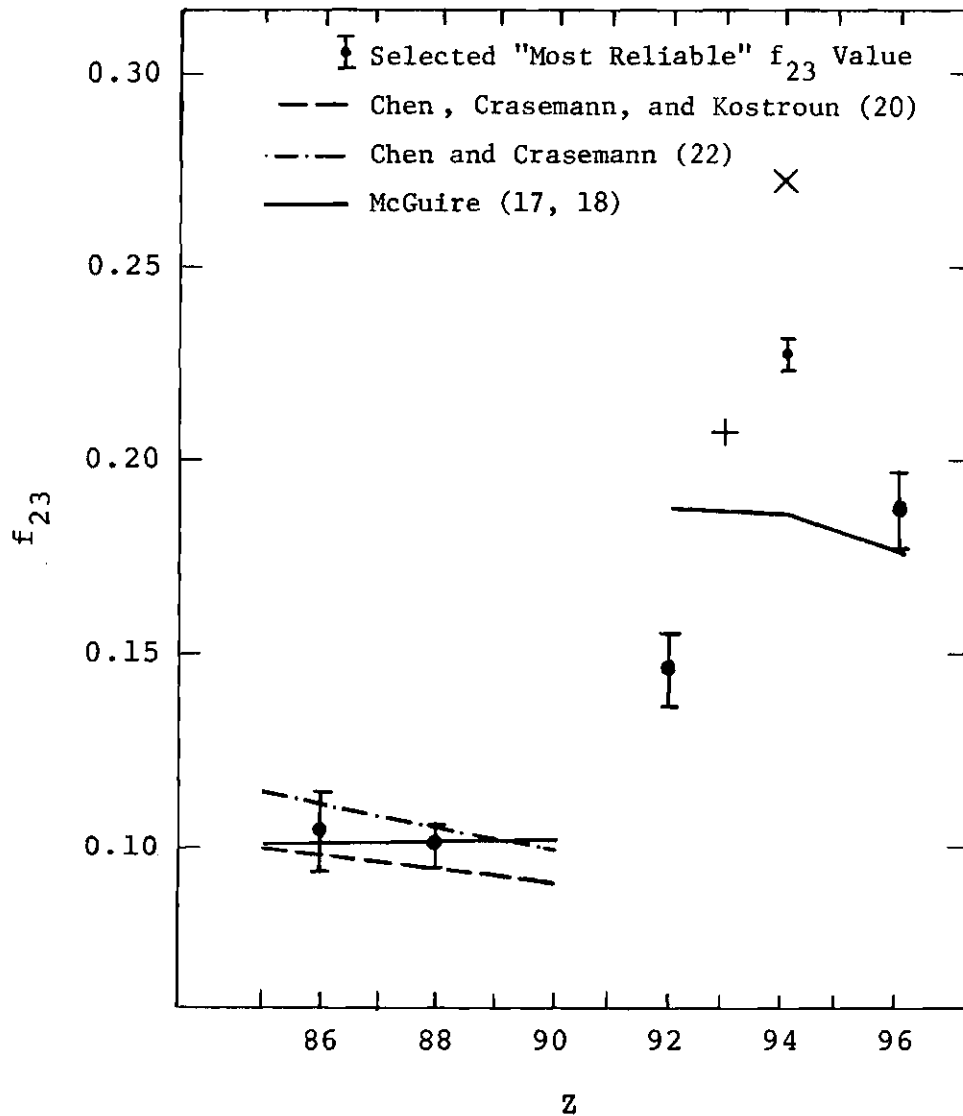


Figure 12. Plot of f_{23} vs Z Above $Z = 85$. (Theoretical points at $Z = 93$ and 94 are calculated using the Hydrogenic model (20) and the IPM (22), respectively, and are plotted as "+" and "x", respectively.)

$$V(r) = 2r^{-1}(NT-Z)$$

where

$$T = 1 - [(e^{r/d} - 1)H + 1]^{-1}$$

and $N = Z - 1$ is the number of core electrons, r is the magnitude of the radial vector, and d and H are adjustable parameters. Crasemann has pointed out (106) that the disagreement at $Z = 94$ with experiment may be due to the inaccuracy of the adjustable parameters, since these parameters are difficult to determine at very high Z .

The hydrogenic calculation of Chen, Crasemann, and Kostroun (20) at $Z = 93$ agrees with the experimentally determined value of f_{23} at $Z = 94$ within 10 percent, but disagrees with the experimental value of f_{23} at $Z = 92$. Disagreement between the theoretical prediction at $Z = 93$ and the experimental results at $Z = 92$ are probably due to the "jump in f_{23} " at or near $Z = 92$. A further discussion which should clarify this point is given in the following paragraphs. The theoretical predictions of Chen, Crasemann, and Kostroun (20) appear to be in qualitative agreement with the experimental results over the region $63 \leq Z \leq 94$. Additional experimental determinations and theoretical predictions are needed above $Z = 90$ before a quantitative comparison can be made.

In order to discuss the theoretical predictions of McGuire (17, 18) and compare them with the experimental

results, a discussion of the "jump in f_{23} " is necessary. The terms "jump in f_{23} " is used to refer to the large increase in f_{23} in the region around $Z = 92$. The "jump in f_{23} " results from an increase in the total Coster-Kronig transition rate, which is due to the onset of the $L_2-L_3M_4$ and the $L_2-L_3M_5$ Coster-Kronig transitions. These particular transitions are not allowed energetically in the region $29 < Z < 91$ (71, 112).

Estimates of the ejected M_4 or M_5 electron energy and thus of the value of Z at which the $L_2-L_3M_{4,5}$ transitions are energetically possible, are made by using energy formulae (eqs. 47 - 51) with tabulated binding energies (59, 62). Using a formula for electron-ejection energy in the theoretical calculation which predicts one or both of these transitions to be energetically impossible, when in fact one or both are possible, causes a large error in the calculated value of f_{23} . This is especially true in the region $Z > 90$ since the $L_2-M_{4,5}$ transitions are theoretically predicted to contribute approximately 70 percent of the total Coster-Kronig transition rate; i.e., approximately 70 percent of the value of f_{23} is predicted to be due to the $L_2-L_3M_{4,5}$ Coster-Kronig transitions. (This estimate is based on the theoretical transition rates predicted by McGuire at $Z = 96$.) In addition, the $L_2-L_3M_4$ transition rate is theoretically predicted to vary in an irregular manner from 260 to 540 percent of the theoretical $L_2-L_3M_5$ transition rate in the

region $96 \leq Z \leq 103$.

In the light of the above considerations, it is possible to discuss the theoretical predictions of McGuire (17, 18). The formula [eq.(51)] used by McGuire to predict the ejected-electron energy forbids the occurrence of the $L_2-L_3M_5$ transition at $Z = 92$, as well as the $L_2-L_3M_4$ transition at $Z = 92$ and 94 . In order to provide realistic values of f_{23} , McGuire calculated the $L_2-L_3M_5$ transition rate at $Z = 92$. The numerical wave functions were calculated using an approximate Herman-Skillman potential (61, 17, 18) and substituting these wave functions into the appropriate expressions (eqs. 25 and 26, see Sect. 2.2) to calculate direct and exchange matrix elements. These matrix elements were substituted into the appropriate expression (eq. 27) to get the transition rate. The transition energy was altered in the calculation to give a positive ejected-electron energy (17, 18).

McGuire used his calculated $L_2-L_3M_5$ transition rate to estimate the $L_2-L_3M_4$ transition rate. This was apparently accomplished by using the average of the ratio of the theoretically calculated $L_2-L_3M_4$ transition rate to the theoretically calculated $L_2-L_3M_5$ transition rate (found to be 4.0) in the region $96 \leq Z \leq 103$. This is a very crude approximation, since the magnitude of the $L_2-L_3M_4$ transition rate varies in an irregular fashion from 2.6 to 5.4 times

the magnitude of the $L_2-L_3M_5$ transition rate. This approximation affects f_{23} quite drastically, since more than 50 percent of the value of f_{23} is due to the $L_2-L_3M_4$ transition.* Therefore, an uncertainty of at least 30 percent exists in the calculated value (18) of f_{23} at $Z = 92$ and 94 due to this assumption alone.

The 17 percent discrepancy at $Z = 94$ between the theoretical predictions of McGuire and the experimental results is not of great significance when one considers the uncertainty in the theoretical results. At $Z = 96$, the $L_2-L_3M_4$ Coster-Kronig transition is predicted by McGuire's energy formula to be energetically possible and well above threshold, and significantly, at $Z = 96$, McGuire's theoretical prediction agrees with experiment.

At $Z = 92$, the experimental value of f_{23} appears to be considerably higher than those for $Z < 90$ but considerably lower than those for $Z > 92$. In addition, the $Z = 92$ experimental result is considerably higher than the calculated** results of McGuire (18) ($f_{23} = 0.095$) assuming M_5

* At $Z = 92$ a calculated value of $f_{23} = 0.155$ corresponds to a $(L_2-L_3M_4/L_2-L_3M_5)$ ratio of 2.6, while a calculated value of $f_{23} = 0.219$ corresponds to a ratio of 5.4. Similarly, at $Z = 94$, f_{23} can be as low as 0.14 or as high as 0.195, depending on this ratio.

** This theoretical calculation did not include the $L_2-L_3M_4$ transition rate.

electron ejection to be allowed, but M_4 electron ejection to be forbidden. However, the theoretical predictions of Chen, Crasemann, and Kostroun (20) at $Z = 93$, which assumed that $L_2-L_3M_{4,5}$ transitions are possible and are well above threshold, lie considerably higher than the experiment at $Z = 92$. The theory of McGuire, assuming that both $L_2-L_3M_{4,5}$ transitions are possible, predicts a value of f_{23} at $Z = 92$ also considerably larger than the experimental one. These facts suggest that at $Z = 92$ the M_4 ejected electron energy is very near threshold*, and thus the probability for the $L_2-L_3M_4$ transition is only a fraction of the value which would be expected if the energy available for the $L_2-L_3M_4$ transition were slightly larger. In other words, at $Z = 92$, it appears that the $L_2-L_3M_5$ transition is fully present, but that the $L_2-L_3M_4$ transition, being just above threshold, contributes only a fraction of its ultimate strength.

The general agreement between the theoretical results in the region $63 \leq Z \leq 88$ (see Fig. 11) is quite a contrast to the disagreement between the theoretical results in the very high- Z region (see Fig. 12). The problems associated with the theoretical results at very high Z are due to the adoption of incorrect energy formula (McGuire's results) and

* As mentioned earlier, the results of Yin et al. (71) at $Z = 29$ and 30 indicate that the $L_2-L_3M_4$ and the $L_2-L_3M_5$ Coster-Kronig transitions are insensitive to the ejected electron energy except very near threshold; i.e., within 2 eV of threshold.

also are due to the problem of obtaining accurate adjustable parameters (Chen and Crasemann's IPM results).

In summary, the comparisons of experiment and theory for f_{23} lead to the following conclusions:

1) The experimental values of f_{23} are in general agreement with the theoretical results in the region $63 \leq Z \leq 88$.

2) In the region $63 \leq Z \leq 88$, the experimental values of f_{23} which are measured generally to plus or minus 10 percent or better are insufficient to distinguish among the different theoretical results which lie within approximately plus or minus 5 percent of each other.

3) The theoretical predication at $Z = 94$ by Chen and Crasemann (22) using the IPM with a GSZ potential is in violent disagreement with the experimental results. This disagreement with experiment at $Z = 94$ may be due to the inaccuracy of the adjustable parameters used in the GSZ potential. It should be recalled (Sect. 6.2) that the IPM model with the GSZ potential disagreed with experiment for ω_2 as well.

4) The theoretical predictions of McGuire agree with the experimental results at $Z = 96$, where both the $L_2-L_3M_{4,5}$ transitions are well above threshold and contribute fully.

5) The experimental results at $Z = 92$ seem to indicate that the $L_2-L_3M_4$ transition is very near threshold and contributes only part of its full intensity to the value of f_{23} .

6) More experimental determinations of f_{23} are necessary, especially at $Z = 91$ and 93 , in order to completely understand the effect of M_5 and M_4 electron-ejection on f_{23} (see Chap. 7).

7) Further calculations above $Z = 92$ of f_{23} will be necessary in order to adequately compare theory with experiment (see Chap. 7).

CHAPTER VII

SUGGESTIONS FOR FURTHER WORK

From the discussion it is quite evident that more experimental and theoretical work is urgently needed for $Z > 90$. The lack of experimental work is due to problems of obtaining suitable radioactive sources. In the region $Z > 90$ some of the radioactive sources which would be suitable for these measurements are difficult to obtain, while the half-lives of otherwise suitable sources are too short to be practical.

A thorough literature search for possible radioactive sources suitable for f_{23} measurements for $Z \geq 90$ indicates that the following experiments would be feasible. At $Z = 90$, an f_{23} measurement could be performed using a Ce^- -L x-ray coincidence technique with the L_2^- and L_3^- -conversion electrons from the 57.5 keV E2 transition in the decay of U^{232} . Such a measurement is somewhat difficult due to the low energy of the L_2^- and L_3^- -conversion electrons (approximately 39 keV). At $Z = 91$, an f_{23} measurement could be performed using a Ce^- -L x-ray coincidence technique with L_2^- and L_3^- -conversion electrons from the 86.5 keV E1 transition in the decay of Np^{237} . If the radioactive sources Pu^{237} and Cm^{241} were available, one could measure f_{23} at $Z = 93$ and 95,

respectively, using the $K_{\alpha_{1,2}}-L$ x-ray coincidence technique. The determination of f_{23} at $Z = 91$ and 93 would be crucial for a complete understanding of the effect of M_5 - and M_4 -electron ejection and for a critical test of theory near threshold (see Fig. 12).

Further calculations should be performed for each Z in the region $90 \leq Z \leq 96$. Calculations employing screened hydrogenic wave functions as well as those based on the Herman-Skillman approach would be valuable. These calculations should use an energy formula which "forbids" and "allows" the proper transitions at a given Z . For such calculations the transition rates for all principal transitions should be tabulated. A theoretical investigation of the variation of transition rates with ejected-electron energy should be performed for the $L_2-L_3M_4$ and $L_2-L_3M_5$ transitions in the vicinity of $Z = 92$.

APPENDIX I

CORRECTION FOR GATE COMPOSITIONS IN THE DETERMINATION OF THE
NET TRUE COINCIDENCE COUNTING RATES USED IN MEASUREMENTS OF
 f_{23} AND EXAMPLE OF EXPERIMENTAL EVALUATION OF L-SUBSHELL
YIELDS

In order to obtain the quantities $C'_{K_{\alpha_2}}$ and $C'_{K_{\alpha_1}}$ which are used to calculate L-subshell yields (eqs. 59-61), corrections must be applied to the gate counting rates (see Sect. 3.3.1). Typically the K_{α_1} gate events are due to continuum events and true events. The continuum events are due to background, Compton scattering, and incomplete charge collection in the detector. The K_{α_2} gate events are due to continuum events, K_{α_1} x-ray events which tail into the K_{α_2} gate, and true events. In certain cases the experimental gate counting rates include contributions due to other sources such as γ rays, e.g. the 106 keV γ ray in the decay of Np^{239} . Complete analysis of the gate counting rates for typical coincidence runs are given in Table 8.

The coincidence spectra must also be corrected for spurious events (see Sect. 3.3.2). Typical corrections for the L_{α} peak along with the magnitude of these corrections are given in Table 9. Typically the L_{α} events in coincidence with the K_{α_1} events are due to chance and cascade, L_{β} and L_{γ}

Table 8. Typical Composition of the K_{α} X-Ray Gates

Atomic Number	Parent	Component	K_{α_1} Gate (%)	K_{α_2} Gate (%)
86	Ra ²²³	Continuum	2.0	2.4
		Overlap of K_{α_1}	-	4.3
		True	98.0	93.3
88	Th ²²⁷	Continuum	9.4	11.9
		Overlap of K_{α_1}	-	4.0
		True	90.6	84.1
92	Np ²³⁵	Continuum	0.7	1.1
		Overlap of K_{α_1}	-	3.3
		True	99.3	95.6
92	Pa ²³³	Continuum	2.7	3.8
		Overlap of K_{α_1}	-	2.6
		True	97.3	93.6
94	Np ²³⁹	Continuum	1.9	2.5
		Overlap of K_{α_1}	-	3.6
		106 keV γ Ray Overlap	6.1	4.1
		True	92.0	89.8
80	Au ¹⁹⁸	Continuum	12.9	17.5
		Overlap of K_{α_1}	-	3.8
		True	87.1	78.7
81	Hg ²⁰³	Continuum	3.8	5.8
		Overlap of K_{α_1}	-	4.7
		True	96.2	89.5
82	Bi ²⁰⁷	Continuum	1.6	2.3
		Overlap of K_{α_1}	-	4.9
		True	98.4	92.8

Table 9. Typical Composition of the L_{α} Peak in the Coincidence Spectra

Atomic Number	Parent	Component	L_{α} (K_{α_1}) (%)	L_{α} (K_{α_2}) (%)
86	Ra ²²³	Chance and Cascade	3.0	20.1
		L_{α} (K_{α_1}) Contribution*	-	23.4
		L_{β} and L_{γ} Tail + Continuum	0.3	6.5
		True Coincidences	96.7	50.0
88	Th ²²⁷	Chance and Cascade	33.7	87.3
		L_{α} (K_{α_1}) Contribution	-	4.1
		L_{β} and L_{γ} Tail + Continuum	1.4	0.7
		True Coincidences	64.9	7.9
92	Np ²³⁵	Chance	2.0	13.8
		L_{α} (K_{α_1}) Contribution	-	10.5
		L_{β} and L_{γ} Tail + Continuum	1.0	7.5
		True Coincidences	97.0	68.2
92	Pa ²³³	Chance and Cascade	29.1	68.4
		L_{α} (K_{α_1}) Contribution	-	4.5
		L_{β} and L_{γ} Tail + Continuum	1.8	3.7
		True Coincidences	69.1	23.4
94	Np ²³⁹	Chance and Cascade	30.3	62.1
		L_{α} (K_{α_1}) Contribution	-	5.2
		L_{β} and L_{γ} Tail + Continuum	1.0	1.7
		L_{α} (106 keV γ) Contribution	3.0	4.0
		True Coincidences	65.7	27.0
80	Au ¹⁹⁸	Chance and Cascade	1.4	8.0
		L_{α} (K_{α_1}) Contribution	-	23.3
		L_{β} and L_{γ} Tail + Continuum	0.4	7.3
		True Coincidences	98.2	61.4

Table 9. (Continued)

Atomic Number	Parent	Component	$L_{\alpha} (K_{\alpha_1})$ (%)	$L_{\alpha} (K_{\alpha_2})$ (%)
81	Hg ²⁰³	Chance and Cascade	3.0	15.4
		$L_{\alpha} (K_{\alpha_1})$ Contribtuion	-	23.5
		L_{β} and L_{γ} Tail + Continuum	0.4	8.4
		True Coincidences	96.6	52.7
82	Bi ²⁰⁷	Chance and Cascade	3.5	20.5
		$L_{\alpha} (K_{\alpha_1})$ Contribution	-	24.0
		L_{β} and L_{γ} Tail + Continuum	0.4	8.2
		True Coincidences	96.1	47.3

* The " $L_{\alpha} (K_{\alpha_1})$ Contribution" is the percentage of L_{α} events in the K_{α_2} gated spectra that are due to the tailing of K_{α_1} into K_{α_2} .

tailing, continuum events, and true events. The L_α events in coincidence with the K_{α_2} events are due to chance and cascade, L_β and L_γ tailing, continuum events, L_α events in the K_{α_2} gated spectra that are due to the tailing of K_{α_1} into K_{α_2} , and true events. In certain cases additional corrections must be applied to account for impurities in gates other than those previously mentioned, e.g. the L_α events which are in coincidence with the 106 keV γ -ray pulses in the K_{α_1} and K_{α_2} gates.

Since typical gate spectra (Fig. 2) and typical coincidence spectra (Fig. 3) were given for the $Z = 94$ experiment, one of these measurements will be used to give an outline of a typical calculation.

In order to calculate the quantities ν_2 , ω_2 , ω_3 , and f_{23} , the quantities $C'_{K_{\alpha_1}}$, $C'_{K_{\alpha_2}}$, $I_{L_3-X(K_{\alpha_1})}$, and $I_{L_2-X(K_{\alpha_2})}$ used in eqs. (59-61) must be derived from the experimentally measured gate counts and the experimentally measured coincidence spectra. For the $Z = 94$ measurements, an analysis of six gate counting rates and the spectra associated with these gates was performed. Only quantities associated with the K_{α_1} and K_{α_2} gate counting rates and their spectra was involved in the final calculation, but the other four gates and their coincidence spectra were used to correct for spurious events in the K_{α_1} and K_{α_2} x-ray gates and their coincidence spectra (see Sects. 3.3.1 and 3.3.2).

The gate counting rates $C'_{K_{\alpha_1}}$ and $C'_{K_{\alpha_2}}$ were corrected

for the continuum, tailing of K_{α_1} pulses into the K_{α_2} gate region (i.e., overlap of K_{α_1} , Table 8), and tailing (i.e., overlap) of the 106 keV γ ray into the K_{α_1} and K_{α_2} x-ray gates^{*}. The details of the measurement of the tailing corrections are given in Sect. 5.2.5. The continuum in the region of the K_{α_1} and K_{α_2} x-ray gates was assumed to vary slowly, therefore, a region above the 106 keV γ ray was used to estimate the continuum. After all corrections were made, 92.0 percent of the K_{α_1} gate events (1.899×10^7 counts) were found to be true events. Therefore, the gate counting rate $C'_{K_{\alpha_1}}$ multiplied by the counting time of the experiment (T) was found to be 1.748×10^7 counts ($C'_{K_{\alpha_1}} \cdot T$)^{**}. The true events ($C'_{K_{\alpha_2}} \cdot T = 1.189 \times 10^7$ counts) in the K_{α_2} gate were found to be 89.8 percent of the gate events (1.325×10^7 counts).

A continuum gated coincidence spectrum^{***} multiplied

^{*} Other corrections [e.g. for unresolved lines and escape peaks [Ge K x-ray escape is negligible in this energy region (115)]] were unnecessary.

^{**} Since ratios of counting rates and intensity per unit time appear in eqs. (59-61), the magnitude of the final L-subshell quantities do not depend on T.

^{***} The gate setting for this continuum gated coincidence spectra is shown in Fig. 2 (the gate between the γ ray and the $K-M_2$ line).

by appropriate normalizing factors* was subtracted from the K_{α_1} x-ray, K_{α_2} x-ray, and 106 keV γ -ray gated coincidence spectra in order to correct for the L x rays in coincidence with the continuum. A similar correction was applied to the K_{β_1} ' x-ray gated coincidence spectra**. After the above corrections were applied, the 106 keV γ -ray gated spectra and the K_{β_1} ' x-ray gated spectra were properly normalized and subtracted from the K_{α_1} and K_{α_2} x-ray gated spectra. These two final spectra contain only true coincidences.

The counts in the L_{ℓ} , L_{α} , $L_{\eta} + L_{\beta}$, and L_{γ} x-ray peaks were summed and corrected for continuum and tailing***. The total counts in the L_{ℓ} , L_{α} , $L_{\beta} + L_{\eta}$, and L_{γ} x-ray peaks in the K_{α_1} x-ray gated spectra and in the K_{α_2} x-ray gated

* The continuum gated coincidence spectrum was normalized to the gate width (number of channels in the gate) of the K_{α_1} x-ray, K_{α_2} x-ray, and γ -ray gates.

** The gate setting for the continuum gated coincidence spectrum that was subtracted from the K_{β_1} ' x-ray gated coincidence spectrum is shown in Fig. 2 (the shaded area to the right of the K - O line).

*** Counts in the regions to the immediate right and immediate left (i.e., continuum regions) of each peak were properly normalized and subtracted from their respective peak totals (i.e., a step-function background subtraction was performed).

spectra* divided by their respective total corrected gate counts along with 1σ statistical errors are given in Tables 10 and 11. In addition, other corrections are tabulated and values of $I_{L_{\beta}}(K_{\alpha_1})/C'_{K_{\alpha_1}}$, $I_{L_{\alpha}}(K_{\alpha_1})/C'_{K_{\alpha_1}}$, and $I_{L_{\eta+\beta}}(K_{\alpha_1})/C'_{K_{\alpha_1}}$; and $I_{L_{\eta+\beta}}(K_{\alpha_2})/C'_{K_{\alpha_2}} - f_{23} [I_{L_{\eta+\beta}}(K_{\alpha_1})/C'_{K_{\alpha_1}}]$ and $I_{L_{\gamma}}(K_{\alpha_2})/C'_{K_{\alpha_2}}$ are tabulated (right most column) in Tables 10 and 11, respectively.

The right hand column of Table 10 and of Table 11 are summed to obtain the quantities $I_{L_{2-X}}(K_{\alpha_1})/C'_{K_{\alpha_1}}$ and $I_{L_{3-X}}(K_{\alpha_2})/C'_{K_{\alpha_2}}$ (i.e., ω_3 and ω_2), respectively. Actually f_{23} was calculated before the quantities in Table 11 are summed since these quantities depend on f_{23} (see the next paragraph for the calculation of f_{23}). The 4 percent (0.0021) uncertainty in the value of ω_3 was added to the 2σ statistical uncertainty (0.014) to obtain a total uncertainty of 0.036 (or 7.2 percent, 95 percent confidence level). The uncertainty in ω_2 was similarly determined to be 0.036 (or 7.2 percent).

* For example, the total counts in the L_{α} peak in coincidence with K_{α_1} gate events and in coincidence with K_{α_2} gate events were 2.926×10^4 and 1.018×10^4 counts, respectively. The number of true L_{α} counts in coincidence with true K_{α_1} x-ray events were 1.921×10^4 counts (65.7 percent true, see Table 9) and 2.751×10^3 counts (27.0 percent true, see Table 9), respectively.

Table 10. Evaluation of ω_3 from Coincidence Data

Peak	Quantity				
	$\frac{[I_{L_3(K_{\alpha_1})}][1+A_{22}f(\theta)][\epsilon \times 10^3]}{C'_{K_{\alpha_1}}}$	$1+A_{22}f(\theta)$	$\frac{[I_{L_3(K_{\alpha_1})}][\epsilon \times 10^3]}{C'_{K_{\alpha_1}}}$	$\epsilon \times 10^3$	$\frac{I_{L_3(K_{\alpha_1})}}{C'_{K_{\alpha_1}}}$
L_ℓ	0.081±0.004	1.236	0.066±0.003	2.98 ^a	0.022±0.001
L_α	1.094±0.015	1.019	1.074±0.015	2.93	0.367±0.005
$L_\eta + L_\beta$	0.307±0.015	1.032	0.297±0.015	2.70	<u>0.110±0.006</u> 0.499±0.008

a) Values given for the efficiency in this table were measured in a different geometry than those given in Fig. 6.

Table 11. Evaluation of ω_2 from Coincidence Data

Peak	Quantity				
	$[I_{L_2+L_3}(K_{\alpha_2})][\epsilon \times 10^3]$	$[f_{23}][I_{L_3}(K_{\alpha_1})][\epsilon \times 10^3]$	$[I_{L_2}(K_{\alpha_2})][\epsilon \times 10^3]$	$\epsilon \times 10^3$	$I_{L_2}(K_{\alpha_2})$
	$C'_{K_{\alpha_2}}$	$C'_{K_{\alpha_1}}$	$C'_{K_{\alpha_2}}$		$C'_{K_{\alpha_2}}$
L_ℓ	0.015±0.004	0.014±0.002		2.98 ^a	
L_α	0.231±0.014	0.232±0.028		2.93	
$L_\eta+L_\beta$	1.141±0.017	0.064±0.009	1.077±0.018	2.70	0.399±0.007
L_γ	0.288±0.008		0.288±0.008	2.46	<u>0.117±0.003</u> 0.516±0.007

a) Values given for the efficiency in this table were measured in a different geometry than those given in Fig. 6.

An experimental value of f_{23} was calculated from the relation*:

$$f_{23} = \frac{[I_{L_{\ell}}(K_{\alpha_2})/C'_{K_{\alpha_2}} + I_{L_{\alpha}}(K_{\alpha_2})/C'_{K_{\alpha_2}}]}{[I_{L_{\ell}}(K_{\alpha_1})/C'_{K_{\alpha_1}} + I_{L_{\alpha}}(K_{\alpha_1})/C'_{K_{\alpha_1}}]} \quad (85)$$

After substituting the appropriate quantities from Table 9 and 10 into eq. (85) and evaluating the result, a value of $f_{23} = 0.216 \pm 0.013$ was obtained (the 0.013 uncertainty is only a 1σ statistical uncertainty). The total uncertainty in f_{23} [i.e., 2σ statistical (0.026) plus the uncertainty in f_{23} due to the tailing** of K_{α_1} pulses into the K_{α_2} gate (0.004)] was 0.030 (or 14 percent, 95 percent confidence level). Thus, $f_{23} = 0.216 \pm 0.030$ for this particular determination.

Judicious assignment of the four gate regions for each of the seven runs effectively produced a set of seven determinations of the L-subshell quantities. An error weighted average of these seven determinations were reported.

* Any fraction of $I_{L_{3-X}}(K_{\alpha_2})/C'_{K_{\alpha_2}}$ and the same fraction of $I_{L_{3-X}}(K_{\alpha_1})/C'_{K_{\alpha_1}}$ may be used to calculate f_{23} . Frequently $I_{L_{\alpha}}(K_{\alpha_2})/C'_{K_{\alpha_2}}$ and $I_{L_{\alpha}}(K_{\alpha_1})/C'_{K_{\alpha_1}}$ are used to calculate f_{23} .

** The uncertainty in the tailing correction was assumed to be 10 percent.

APPENDIX II

VALUES OF f_{23} OMITTED FROM "MOST RELIABLE" VALUES

Table 12. Values of f_{23} Omitted From Selected "Most Reliable" Values

Z	f_{23}	Reference	Comment
57	0.21 ± 0.02	143	No reference to L_{η} Correction, performed using critical absorbers, no reference to correction for tailing of L_{β} and L_{γ} into L_{α} peak.
63	0.172 ± 0.015	144,145	Unpublished result.
64	0.223 ± 0.011	147	No reference to L_{η} Correction, no reference to correction for tailing of L_{β} and L_{γ} into L_{α} peak.
65	0.066 ± 0.014	148,116	Possible improper tailing correction, and possible improper cascade correction*.
67	0.205 ± 0.034	149,15	Unpublished result.
68	0.225 ± 0.025	149,15	Unpublished result.
73	0.20 ± 0.04	33	Low resolution, performed using critical absorbers.
	0.150 ± 0.007	148,110	Low resolution.
80	0.22 ± 0.04	153	Assumed previously measured values in order to derive result.
	0.08 ± 0.02	33	Low resolution, performed using critical absorbers.
	0.188 ± 0.010	148,154	Low resolution.

Table 12. (Continued)

Z	f_{23}	Reference	Comment
81	0.25 ± 0.13	155	Assumed previously measured values in order to derive result.
	0.169 ± 0.010	156	Low resolution.
	0.130 ± 0.006	157	Unpublished result.
82	0.164 ± 0.016	37	Low resolution.
	0.156 ± 0.010	158	No reference to correction for tailing of L_{β} and L_{γ} into L_{α} gates.
83	0.06 + 0.14 - 0.06	109	Assumed previously measured values in order to derive result.
88	0.01 ± 0.07	92	α -particle-L x-ray coincidence technique used.
	0.053 ± 0.052	Present Work, 73	Assigned error limits negate the value of this result.
90	0.13 ± 0.10	91	α -particle-L x-ray coincidence technique used.
92	0.43 ± 0.06	89	α -particle-L x-ray coincidence technique used.
	0.37 ± 0.07	89	α -particle-L x-ray coincidence technique used.
	0.07 ± 0.05	92	α -particle-L x-ray coincidence technique used.
	0.23 ± 0.12	38	Assumed previously measured values in order to derive result.

Table 12. (Continued)

Z	f_{23}	Reference	Comment
92	0.14 + 0.11 - 0.06	112,159	Assumed theoretical values in order to derive result.
93	0.02 + 0.05 - 0.02	160	Assumed previously measured values in order to derive result.
94	0.22 ± 0.08	26	α-particle-L x-ray coincidence technique used.
	0.42 ± 0.08	89	α-particle-L x-ray coincidence technique used.
	0.21 ± 0.08	90	Assumed previously measured values in order to determine result.
	0.24 ± 0.08	38	Assumed previously measured values in order to determine result.
	0.233 ± 0.015	144,145	Unpublished result.
	0.24 + 0.19 - 0.09	112,159	Assumed theoretical values in order to derive result.
96	0.226 ± 0.017	144,145	Unpublished result.

* J. C. McGeorge, private communication (1972).

APPENDIX III

EVALUATION OF HIGHLY ORIENTED GRAPHITE CURVED CRYSTALS FOR
X-RAY SPECTROSCOPY WITH RADIOACTIVE SOURCES

The possible use of highly oriented graphite (HOG) mosaic curved crystals (161) for determination of x-ray fluorescence and Coster-Kronig yields was evaluated. Budick and Derman (162) had measured L-subshell fluorescence yields at $Z = 47$ and 52 using such a crystal. From their singles spectra and previously measured value of the mean L-shell fluorescence yield ($\bar{\omega}_L$), they were able to extend our knowledge of L-subshell yields to lower Z with 10 percent accuracy (previous measurements existed only for $Z > 53$).

Differentiating the Bragg equation, $n\lambda = 2D\sin\theta$, the energy resolution of the crystal is given by:

$$\left(\frac{dE}{d\theta}\right) = - \frac{2E^2 D \cos\theta}{12.4} (\text{keV } \text{\AA})^{-1} \quad (86)$$

where D is the crystal spacing ($2D = 6.7 \text{\AA}$), $d\theta$ is the slit width including the working angle of the crystal.

Assuming $d\theta = 0.5^\circ$ (by assuming a slit width of 0.1° and a rocking angle of 0.4°), one finds from the table below that the resolution becomes better than that of a semiconductor detector only below 6 keV.

Budick and Derman worked with curved mosaic graphite

crystals having a mosaic spread of 0.8° and collimators to 0.25° to obtain resolutions for the L_α x rays of Ag and Te (2.88 and 3.76 keV, respectively) in first-order reflection of 65 and 110 eV FWHM, respectively. Table 13 suggests that the resolution obtainable is close to the best that might be achieved on a practical basis, and that the Si(Li) detector begins to compete favorably above 6 keV. Although the HOG curved crystals have much higher diffracting power (161) (6.7 for Cu K_α x-rays) than LiF crystals, their very low efficiency (approximately 10^{-4} to 10^{-5}) makes K_α x-ray-L x-ray coincidence studies impossible within a reasonable time. The problems arising from low efficiency, source attenuation, and assumptions of quantities from other measurements in the singles use of HOG crystals makes it difficult to use them for precise measurements of fluorescence and Coster-Kronig yields at low Z; however, at present, they represent perhaps the only available method.

Table 13. Resolution vs Energy of Highly Oriented Graphite Curved Crystal (Typical)

E (keV)	dE (FWHM) in eV
2	7.2
3	33.5
4	67.0
5	105.0
6	162.0
7	223.0

BIBLIOGRAPHY

1. W. C. Röntgen, Sitzber. Würzburger Phys.-Med. Ges. (1895); Ann. Physik 64, 1 (1898); translation by A. Stanton in Science 3, 227 and 726 (1896).
2. P. Auger, J. Phys. Radium 6, 205 (1925).
3. D. Coster and R. de L. Kronig, Physica 2, 13 (1935).
4. H. G. J. Moseley, Phil. Mag. 26, 1024 (1913).
5. N. Bohr, Phil. Mag. 26, 1, 476 (1913).
6. W. Heisenberg, Z. Phys. 33, 879 (1925).
7. E. Schrödinger, Ann. Physik 79, 734 (1926).
8. P. A. M. Dirac, Proc. Roy. Soc. (London) A109, 642 (1925).
9. H. S. W. Massey and E. H. S. Burhop, Proc. Roy. Soc. (London), A153, 661 (1936).
10. J. H. Scofield, Phys. Rev. 179, 9 (1969).
11. L. Pincherle, Nuovo Cimento 12, 81 (1935).
12. E. H. S. Burhop, Proc. Roy. Soc. (London) A148, 272 (1935).
13. E. H. S. Burhop, The Auger Effect and Other Radiationless Transitions, (Cambridge U. P., Cambridge 1952).
14. E. H. S. Burhop and W. N. Asaad "The Auger Effect" in Advance in Atomic and Molecular Physics, (Academic Press, New York, 1972) Vol. 8, p. 163.
15. W. Bambynek, B. Crasemann, R. W. Fink, H. U. Freund, H. Mark, C. D. Swift, R. E. Price, and P. V. Rao, Rev. Mod. Phys. 44, 716 (1972).
16. M. A. Listengarten, Izv. Akad. Nauk SSSR, Ser. Fiz. 24, 1041 (1960) [Bull. Acad. Sci. USSR, Phys. Ser. 24, 1050 (1960)].
17. E. J. McGuire, Phys. Rev. A3, 587 (1971).

18. E. J. McGuire, in Fink et al., Ref. (19), p. 662 (1973).
19. R. W. Fink, S. T. Manson, J. M. Palms and P. V. Rao eds., Inner Shell Ionization Phenomena and Future Applications, (North Holland Publishing Co., Amsterdam, 1973).
20. M. H. Chen, B. Crasemann and V. O. Kostroun, Phys. Rev., A4, 1 (1971).
21. B. Crasemann, M. H. Chen, and V. O. Kostroun, Phys. Rev. A4, 2161 (1971).
22. M. H. Chen and B. Crasemann, in Fink et al., Ref. (19), p. 43 (1973).
23. H. Lay, Z. Phys., 91, 533 (1934).
24. H. Küstner and E. Arends, Ann. Phys. 22, 443 (1935).
25. R. J. Stephenson, Phys. Rev. 51, 637 (1937).
26. L. Salgueiro, J. G. Ferreira, J. J. H. Park and M. A. S. Ross, Proc. Phys. Soc. (London) 77, 657 (1961).
27. N. H. Lazar and W. S. Lyon, Bull. Amer. Phys. Soc. 3, 29 (1958).
28. R. C. Jopson, H. Mark, C. D. Swift and M. A. Williamson, Phys. Rev. 131, 1165 (1963).
29. R. C. Jopson, H. Mark, C. D. Swift and M. A. Williamson, Phys. Rev. 136, A69 (1964).
30. R. C. Jopson, J. M. Khan, H. Mark, C. D. Swift, and M. A. Williamson Phys. Rev., 133, A381 (1964).
31. K. Homuth, G. Müller, and J. Schintlmeister, Nucl. Phys. 48, 209 (1963).
32. K. Homuth and G. Winter, Phys. Letters 10, 58 (1964).
33. P. V. Rao and B. Crasemann, Phys. Rev. 139, A1926 (1965).
34. R. E. Price, H. Mark, and C. D. Swift, Phys. Rev. 176, 3 (1968).
35. P. V. Rao, R. E. Wood, and J. M. Palms in Berényi, Ref. (36), p. 264 (1968).

36. D. Berényi, ed., Proceedings of the Conference on Electron Capture and Higher-Order Processes in Nuclear Decay (Eötvös Lóránd Physical Society, Budapest, 1968).
37. P. V. Rao, R. E. Wood, J. M. Palms, and R. W. Fink, Phys. Rev. 178, 1997 (1969).
38. J. C. McGeorge and R. W. Fink, Z. Phys. 248, 208 (1971).
39. J. L. Campbell, J. Phys. (London) B5, L40 (1972).
40. J. C. McGeorge, in Fink et al., Ref. (19), p. 157 (1973).
41. V. R. Veluri, Thesis, Emory University (unpublished) (1973).
42. M. H. Chen, B. Crasemann, P. V. Rao, J. M. Palms, and R. E. Wood, Phys. Rev. A4, 846 (1971).
43. R. M. Eisberg, Fundamentals of Modern Physics, (Wiley, New York, 1961) pp. 285 - 291.
44. E. U. Condon and C. H. Shortley, Theory of Atomic Spectra (Cambridge U. P., Cambridge, 1953).
45. W. Heitler, The Quantum Theory of Radiation (Clarendon Press, Oxford, 1954) 3rd ed.
46. S. A. Moszkowski, in K. Siegbahn, Ref. (47), Vol. II, p. 863 (1965).
47. K. Siegbahn, ed., Alpha, Beta, Gamma-Ray Spectroscopy (North-Holland Publ. Co., Amsterdam, 1965) 2nd ed.
48. M. E. Rose, Relativistic Electron Theory (Wiley, New York, 1961).
49. G. Wentzel, Z. Phys. 43, 524 (1927).
50. C. Møller, Z. Phys. 70, 786 (1931).
51. J. R. Oppenheimer, Z. Phys. 55, 725 (1929).
52. J. A. Gaunt, Phil. Trans. A229, 163 (1930).
53. H. A. Bethe and E. E. Salpeter, Quantum Mechanics of One- and Two-Electron Atoms (Springer-Verlag, Berlin, 1957).
54. W. N. Asaad and E. H. S. Burhop, Proc. Phys. Soc. (London) 71, 369 (1958).

55. W. Gordon, *Z. Phys.* 48, 180 (1928).
56. E. J. Callan, *Phys. Rev.* 124, 793 (1961).
57. V. O. Kostroun, M. H. Chen, and B. Crasemann, *Phys. Rev.* A3, 533 (1971).
58. J. H. Scofield, Univ. Calif. Lawrence Radiation Laboratory Report UCRL-51231 (unpublished) (1972).
59. J. A. Bearden and A. F. Burr, *Rev. Mod. Phys.* 39, 125 (1967).
60. A. E. S. Green, D. L. Sellin, and A. S. Zachor, *Phys. Rev.* 184, 1 (1969).
61. F. Herman and S. Skillman, Atomic Structure Calculations (Prentice-Hall, Englewood Cliffs, New Jersey, 1963).
62. K. Siegbahn, ed., ESCA: Atomic Molecular and Solid State Structure Studied by Means of Electron Spectroscopy (Novo Acta Regiae Societatis Upsaliensis, Uppsala, 1967).
63. R. Latter, *Phys. Rev.* 99, 510 (1955).
64. E. J. McGuire, *Phys. Rev.* 175, 20 (1968).
65. L. L. Foldy and S. A. Wouthuysen, *Phys. Rev.* 78, 29 (1950).
66. H. R. Rosner and C. P. Bhalla, *Z. Phys.* 231, 347 (1970).
67. S. K. Haynes, in Fink et al., Ref. (19), p. 559 (1973).
68. E. J. McGuire, Sandia Laboratories Report SC-RR-71-0075 (unpublished) (1971).
69. R. A. Rubenstein and J. N. Snyder, *Phys. Rev.* 97, 1653 (1955).
70. E. J. Callan, *Phys. Rev.* 124, 793 (1961).
71. L. I. Yin, I. Adler, M. H. Chen, and B. Crasemann, *Phys. Rev.* A7, 897 (1973).
72. E. J. Callan, *Rev. Mod. Phys.* 35, 524 (1963).
73. J. C. McGeorge, D. W. Nix, and R. W. Fink, *J. Phys.* (London) B6, 573 (1973).
74. W. Mehlhorn, The Auger Effect, (Univ. of Nebraska Press, Lincoln, Nebraska, 1969).

75. I. Bergström and R. D. Hill, Ark. Fys. 8, 21 (1954).
76. E. J. McGuire, Phys. Rev. A5, 2313 (1972).
77. R. G. Albridge and J. M. Hollander, Nucl. Phys. 27 554 (1961).
78. J. A. Bearden, J. Appl. Phys. 37, 1681 (1966).
79. R. D. Deslattes, Thesis, Johns Hopkins University (unpublished) (1959).
80. C. McGilvary and K. Lansdale, International Tables for X-Ray Crystallography (Kynoch Press, Birmingham) 2nd ed. (1965).
81. A. J. Guttman and W. Wagenfeld, Acta Crystallogr. 22, (3), 334 (1967).
82. M. E. Rudd, in Fink et al. Ref. (19), p. 1485 (1973).
83. H. Behrens and W. Bühring, in Berényi, Ref. (36). p. 61 (1968).
84. L. N. Zyryanova and Y. P. Suslov, in Berényi, Ref. (36), p. 45 (1968).
85. M. J. Martin and P. H. Blichert-Toft, Nucl. Data Tables, A8, 1 (1970).
86. J. H. Hamilton, A. V. Ramayya, B. van Nooijen, R. G. Albridge, E. F. Zganjar, S. C. Pancholi, J. M. Hollander, V. S. Shirley, and C. M. Lederer, Nucl. Data A1, 521 (1966).
87. O. Dragoun, H. C. Pauli, and F. Schmutzler, Nucl. Data A6, 235 (1969).
88. R. S. Hager and E. C. Seltzer, Nucl. Data A4, 1 (1968).
89. J. Byrne, W. Gelletly, M. A. S. Ross, and F. Shaikh, Phys. Rev. 170, 80 (1968).
90. J. Byrne, R. J. D. Beattie, S. Benda, and I. Collingwood, J. Phys. (London) B3, 1166 (1970).
91. J. G. Ferreira, J. C. Soares, A. Barroso, and F. B. Gil, J. Phys. (London) A4, 679 (1971).
92. F. B. Gil, A. Barroso, J. C. Soares, and J. G. Ferreira, Phys. Rev. A5, 536 (1972).

93. R. L. Watson and T. K. Li, Nucl. Phys. A178, 201 (1971).
94. Y. Y. Chu, M. L. Perlman, P. F. Dittner, and C. E. Bemis, Phys. Rev. A5, 67 (1972).
95. P. V. Rao, M. H. Chen, and B. Crasemann, Phys. Rev. A5, 997 (1972).
96. H. Schmied and R. W. Fink, Phys. Rev. 107, 1062 (1957).
97. R. W. Fink and B. L. Robinson, Phys. Rev. 98, 1293 (1955).
98. G. Bertolini, A. Bisi, E. Lazarrini, and L. Zappa, Nuovo Cim. 11, 539 (1954).
99. D. W. Nix, J. C. McGeorge, and R. W. Fink, in Fink et al., Ref. (19), p. 206 (1973).
100. D. W. Nix, J. C. McGeorge, and R. W. Fink, Z. Phys. 256, 131 (1972).
101. T. Zimmerli and A. Flammersfeld, Z. Phys. 176, 323 (1963).
102. K. Risch, Z. Phys. 150, 87 (1958).
103. H. Winkenbach, Z. Phys. 152, 387 (1958).
104. H. U. Freund and R. W. Fink, Phys. Rev. 178, 1952 (1969).
105. L. I. Yin, T. Tsang, and I. Adler, in Fink et al. Ref. (19), p. 694 (1973).
106. J. L. Campbell, L. A. McNelles, J. S. Geiger, R. L. Graham, and J. S. Merritt, Can. J. Phys. 52, 488 (1974).
107. P. Boyer and J. L. Barat, Nucl. Phys. A115, 521 (1968).
108. R. E. Wood, V. R. Veluri, J. M. Palms, and P. V. Rao, in Fink et al., Ref. (19), p. 226 (1973).
109. M. A. S. Ross, A. J. Cochran, J. Hughes, and N. Feather, Proc. Phys. Soc. (London) A68, 612 (1955).
110. S. Mohan, R. W. Fink, R. E. Wood, J. M. Palms, and P. V. Rao, Z. Phys. 239, 423 (1970).

111. S. Mohan, Thesis, Georgia Institute of Technology (unpublished) (1972).
112. K. R. Baker, F. Tolea, and R. W. Fink, submitted to Z. Phys. (1974).
113. V. R. Veluri, R. E. Wood, J. M. Palms, and P. V. Rao in Fink et al., Ref. (21), p. 251 (1973).
114. J. P. Briand, P. Chevallier, and M. Tavernier, Jour. de Physique C4, 165 (1971).
115. J. S. Hansen, Thesis, Georgia Institute of Technology, (unpublished) (1971).
116. J. C. McGeorge, H. U. Freund, and R. W. Fink, Nucl. Phys. A154, 526 (1970).
117. W. Moellering and J. H. D. Jensen, Z. Phys. 144, 252 (1956).
118. F. A. Babushkin, Opt. Spectrosk. 19, 3 (1965), [Opt. Spectrosc. 19, 1 (1965)].
119. H. W. Beste, Z. Phys. 213, 333 (1968).
120. A. A. Konstantinov and T. E. Sazonova, Izv. Akad, Nauk SSSR, Ser. Fiz. 32, 631 (1968) [Bull. Acad. Sci. USSR, Phys. Ser., 32, 581 (1968)].
121. J. H. Landrum, M. Lindner, and N. Jones, Anal. Chem. 41, 840 (1969).
122. M. Lindner, Lawrence Radiation Laboratory Report UCRL-14258 (1965).
123. W. W. Meinke, University of California Radiation Laboratory AECD-2750, (1949).
124. H. W. Kirby, The Radiochemistry of Protoactinium, NAS-NS-3016 (1959).
125. C. Sebillle and C. F. Leang, Compt. Rend. B266, 1049 (1968).
126. Y. A. Ellis, Nucl. Data Sheets B6, 257 (1971).
127. W. D. Schmidt-Ott, J. C. McGeorge, and R. W. Fink, Z. Phys. 255, 161 (1972).

128. J. S. Hansen, H. U. Freund, E. Karttunen and R. W. Fink: Proc. Int. Conf. on Radioactivity in Nuclear Spectroscopy, Nashville, Tennessee (1969) (Gordon and Breach Publishers, New York, 1972).
129. J. S. Hansen, J. C. McGeorge, D. W. Nix, W. D. Schmidt-Ott, I. Unus, and R. W. Fink, Nucl. Inst. and Methods 106, 365 (1973).
130. R. E. Wood, P. V. Rao, H. O. Puckett, and J. M. Palms, Nucl. Inst. Methods 94, 245 (1971).
131. E. Storm and H. I. Israel, Nucl. Data A7, 565 (1970).
132. W. E. Davidson and R. D. Conner, Nucl. Phys. A116, 342 (1968).
133. J. C. McGeorge, D. W. Nix, R. W. Fink, and J. H. Landrum, Z. Phys. 255, 335 (1972).
134. J. E. Gindler, J. R. Huizenga, and D. W. Engelkemeir, Phys. Rev. 109, 1263 (1958).
135. J. E. Gindler and D. W. Engelkemeir, Phys. Rev. 119, 1645 (1960).
136. C. M. Lederer, J. M. Hollander, and I. Perlman, Table of Isotopes, 6th ed. (Wiley, New York, 1967).
137. D. Engelkemeir, Phys. Rev. 181, 1675 (1969).
138. J. R. Van Hise and D. Engelkemeir, Phys. Rev. 171, 1325 (1968).
139. G. Bertolini, A. Bisi, E. Lazzarini, and L. Zappa, Nuovo Cim. 11, 539 (1954).
140. A. Bisi, E. Germagnoli, and L. Zappa, Nucl. Phys. 1, 593 (1956).
141. L. E. Bailey and J. B. Swedland, Phys. Rev. 158, 6 (1967).
142. F. Bertrand, G. Charpak, and F. Suzor, J. Phys. Radium 20, 462; 20, 956 (1959).
143. D. G. Douglas, Can. J. Phys. 51, 1519 (1973).
144. M. R. Zalutsky and E. S. Macias, Bull. Am. Phys. Soc. 18, 635 (1973).

145. M. R. Zalutsky and E. S. Macias, submitted to Phys. Rev. A (1974).
146. V. R. Veluri, R. E. Wood, J. M. Palms, and P. V. Rao submitted to J. Phys. B (London) (1974).
147. D. G. Douglas, Can. J. Phys. 50, 1697 (1972).
148. J. C. McGeorge, S. Mohan, and R. W. Fink, Phys. Rev. A4, 1317 (1971).
149. C. P. Holmes and V. O. Kostroun, Bull. Amer. Phys. Soc. 15, 561 (1970).
150. S. Mohan, H. U. Freund, R. W. Fink, and P. V. Rao, Phys. Rev. C1, 254 (1970).
151. J. L. Campbell, L. A. McNelles, J. S. Geiger, R. L. Graham, and J. S. Merritt, Bull. Amer. Phys. Soc. 19, 520 (1974).
152. S. Mohan, W. D. Schmidt-Ott, J. C. McGeorge, and R. W. Fink, in Fink et al., Ref. (19), p. 244 (1973).
153. J. C. Nall, Q. L. Baird, and S. K. Haynes, Phys. Rev. 118, 1278 (1960).
154. J. M. Palms, R. E. Wood, P. V. Rao and V. O. Kostroun, Phys. Rev. C2, 592 (1970).
155. Z. Sujkowski and O. Melvin, Ark. Fys. 20, 193 (1961).
156. R. E. Wood, J. M. Palms, and P. V. Rao, Phys. Rev. 187, 1479 (1969).
157. F. Tolea, J. C. McGeorge, and R. W. Fink (unpublished data) (1973).
158. R. E. Wood, J. M. Palms and P. V. Rao, Phys. Rev., A5, 11 (1972).
159. F. Tolea, Thesis, Georgia Institute of Technology, (unpublished) (1974).
160. G. G. Akalaev, N. A. Vatanov, and P. S. Samoilov, Izv. Akad. Nauk SSSR, Ser. Fiz. 28, 1259 (1964) [Bull. Acad. Sci. USSR, Phys. Ser. 28, 1158 (1964)].
161. R. W. Gould, S. R. Bates, and C. J. Sparks, Appl. Spectr. 22, 549 (1968).

162. B. Budick and S. Derman, Phys. Rev. Lett. 29, 1055 (1972).

VITA

Dale Wendel Nix was born June 17, 1947, in Villa Rica, Georgia. He attended Buchanan High School and upon graduation completed one year of study at Asbury College, Wilmore, Kentucky. In 1966 he transferred to West Georgia College, Carrollton, Georgia, and in 1968 received his B.A. Degree in Chemistry.

In the fall of 1968 he entered Georgia Institute of Technology, School of Chemistry, and in March, 1972, received his M.S. Degree. His program at Georgia Tech has been supported in part by a Georgia Tech Teaching Assistantship and a U.S. Atomic Energy Commission Research Assistantship. His publications include:

D. W. Nix, J. C. McGeorge, and R. W. Fink, "Mean L-Shell X-Ray Fluorescence Yields from $Z = 55 - 65$ ", In: Inner Shell Ionization Phenomena and Future Applications, R. W. Fink, S. T. Manson, J. M. Palms, and R. V. Rao, eds. p. 206 (1973).

J. C. McGeorge, D. W. Nix, R. W. Fink, and J. H. Landrum, "L-Subshell Fluorescence and Coster-Kronig Yields at $Z = 92$ and the Decay of Np^{235} ", Z. Phys. 255, 335 (1972).

D. W. Nix, J. C. McGeorge, and R. W. Fink, "Mean L-Shell X-Ray Fluorescence Yields at $Z = 47, 60, \text{ and } 63$ ", Z. Phys. 256, 131 (1972).

J. S. Hansen, J. C. McGeorge, D. W. Nix, W. D. Schmidt-Ott, I. Unus, and R. W. Fink, "Accurate Efficiency Calibration and Properties of Semiconductor Detectors For Low-Energy Photons", Nucl. Instr. and Meth. 106, 365 (1973).

J. C. McGeorge, D. W. Nix, and R. W. Fink, "Coster-Kronig and Fluorescence Yields for the L_2 and L_3 Subshells in the High-Z Region", J. Phys. (London) B6, 573 (1973).

D. W. Nix, J. C. McGeorge, and R. W. Fink, "X-Ray Intensity Ratio for $I_{L_\alpha} / I_{L_\beta}$ in the Region $55 \leq Z \leq 94$ ", Phys. Lett. A46, 205 (1973).

Dale Nix is married to the former Susan Lynda Caldwell of Atlanta, Georgia.